



Radar Systems and
Remote Sensing Laboratory

(2)

AD-A219 217

DTIC FILE COPY

A LABORATORY INVESTIGATION INTO
MICROWAVE BACKSCATTERING
FROM SEA ICE

DTIC
ELECTE
MAR 12 1990
S D

Approved for public release;
Distribution Unlimited

2

**A LABORATORY INVESTIGATION INTO
MICROWAVE BACKSCATTERING
FROM SEA ICE**

Jonathan W. Bredow
(Ph.D. Dissertation)

DTIC
ELECTE
MAR 12 1990
S D D

Radar Systems and Remote Sensing Laboratory
University of Kansas Center for Research, Inc.
2291 Irving Hill Road
Lawrence KS 66045-2969, USA
913/864-4835
FAX: 913/864-7789, TELEX: 706352, OMNET: KANSAS.U.RSL

RSL Technical Report 8240-1

August 1989

DECLASSIFICATION STATEMENT A
Approved for public release;
Distribution Unlimited

Supported by:

Office of Naval Research
Arlington VA 22217-5000

and

National Aeronautics Space Administration
NASA Headquarters
Washington DC 20546

Grant # N00014-89-J-1456

90 03 07 015

ABSTRACT

The purpose of the research reported here was to determine the sources of scattering of artificial sea ice, to compare backscatter measurements semi-quantitatively with theoretical predictions, and to develop inexpensive polarimetric radars for sea ice backscatter studies.

In Chapter 2, a brief review of the dielectric properties of sea ice and of commonly used surface and volume scattering theories is presented,

In Chapter 3, we provide a description of the backscatter measurements performed and experimental techniques used,

Discussion of the development of inexpensive short-range polarimetric radars is the topic of Chapter 4. The steps taken to add polarimetric capability to a simple FM-CW radar are considered as are sample polarimetric phase measurements of the radar. We also consider limitations of this system and discuss the development of a radar that avoids the oscillator instability problems of continuously tuneable oscillators by doing measurements at discrete frequencies, using a synthesized frequency source. We present results of simple test of copolar phase capability and a simple method of doing phase calibrations in the laboratory.

VG

3/9/90

STATEMENT "A" per Charles Luther
ONR/Code 1121RS
TELECON

per call



In Chapter 5, we discuss ice surface characterization data and techniques, including computation of surface rms height and correlation length and air bubble distribution statistics. We also present a method of estimating the standard deviation of rms height and correlation length for cases of few data points.

Chapter 6 consists of comparisons of backscatter measurements and theory. We determined that backscatter from an extremely smooth saline ice surface at C band, i.e., rms height < 0.05 cm, cannot be attributed only to surface scatter. We found that snow cover had a significant influence on backscatter from extremely smooth saline ice at C band. We determined that backscatter at C band from moderately smooth desalinated ice, at incidence angles of less than 30° (rms height ≈ 0.1 cm), and rough saline ice (rms height $= 0.5$ cm) was dominated by surface scatter. We found that volume scatter from desalinated ice is important at X band and that it is dominant at Ku band at angles of 10° or more from nadir.

Conclusions and suggestions for future research are presented in Chapter 7.

Keywords: Microwave Publications, Remote Sensing, Etc.

TABLE OF CONTENTS

1.0 Introduction	1
1.1.0 Background	2
1.1.1 History of remote sensing of sea ice	2
1.1.1.1 Determination of scene parameters	6
1.1.1.2 Automatically extracting scene parameter	13
1.2 Organization	15
2.0 Background	18
2.1 The dielectric properties of sea ice at microwave frequencies	18
2.1.1 Formation and morphology of sea ice	18
2.1.2 Electrical properties of sea ice	25
2.2 Theories used in remote sensing of sea ice .	31
2.2.1 Review of surface scattering theories	31
2.2.1.1 Kirchhoff surface scattering theory	31
2.2.1.2 Small Perturbation Method	34
2.2.1.3 Validity conditions	36
2.2.2 Volume scattering theories	36
3.0 Measurements conducted: microwave backscatter and ice characterization	41
3.1 CRREL 1987	46
3.1.1 Measurement regime	46
3.1.2 Experimental procedure	46
3.1.3 Measured surface physical characteristics	46
3.2 CRREL 1988	50
3.2.1 Measurement regime	50
3.2.2 Experimental procedure	50
3.2.3 Measured surface physical characteristics	51
3.3 CRREL 1989	57
3.3.1 Measurement regime	57
3.3.2 Experimental procedure	61
3.3.3 Measured surface physical characteristics	61
4.0 The radar systems	69
4.1 Design considerations and operation	69
4.1.1 The SOURCECAT radar	69
4.1.2 PAIR	71
4.1.2.1 Discussion of circuitry unique to PAIR .	74
4.1.3 STEFRAD	78
4.2 Comparison of modes of operation	81
4.2.1 SOURCECAT	81
4.2.2 PAIR	83
4.2.3 STEFRAD	85
4.3 Calibration and performance	93
4.3.1 SOURCECAT	93
4.3.2 PAIR	93
4.3.3 STEFRAD	94

5.0 Analysis of ice sheet physical parameters ..	101
5.1 Surface roughness	101
5.2 Internal structure	109
5.3 Snow cover	116
6.0 Data analysis and comparison with theory ...	118
6.1 Computation of σ^2	118
6.1.1 Consideration of errors	122
6.2 Results	127
6.2.1 Smooth saline ice	128
6.2.2 Snow cover effects	138
6.2.3 Rough saline ice	145
6.2.4 Desalinated ice	147
7.0 Conclusions and recommendations	159
7.1 Conclusions	159
7.2 Recommendations	161

LIST OF FIGURES

- Figure 2.1: Phase relations for "standard" sea ice. Circles on the brine-salt line indicates temperatures at which solid salts precipitate (Assur, 1958).
- Figure 2.2: Simplified geometry of first-year sea ice (Vant et al., 1978).
- Figure 2.3: Variation of salinity with time for 2.5 cm sections of ice at a depth between 40 and 42.5 cm. Broken line indicates "stable" salinity or average of all the salinities except the initial high value at this level (Nakawo and Sinha, 1981).
- Figure 2.4: Salinity and temperature profiles of a typical frazil ice core (Martin, 1979).
- Figure 2.5: Conceptual view of a brine drainage channel (Vant, 1976).
- Figure 2.6: Temperature and salinity profiles for typical multiyear sea ice (McNeill and Hoekstra, 1973).
- Figure 2.7: Real and imaginary parts of the relative dielectric constant of brine (Vant et al., 1978).
- Figure 3.1: Setup for CRREL'87 experiment.
- Figure 3.2: Setup for CRREL'88 experiment. Tent (T) has been rolled off to expose pond (P) for measurements from gantry (G).
- Figure 3.3: Setup for CRREL'89 experiment. University of Kansas and Environmental Research Institute of Michigan radars mounted on the gantry (G), University of Washington (UW) radiometers, and University of Massachusetts (UM) radar and radiometer during measurements on pond (P). Weather station (W) is in foreground.
- Figure 3.4: Vertical growth history of saline ice sheet grown during CRREL'87 as seen in thin section photographed between crossed polarizers (courtesy of CRREL).

- Figure 3.5: Salinity profiles of saline ice sheet grown during CRREL'87 experiment.
- Figure 3.6: Growth history of saline ice sheet of CRREL'88 experiment as revealed in thin sections of ice structure photographed between crossed polarizers (courtesy of CRREL).
- Figure 3.7: (a) saline ice sheet of Fig. 3.6 after 2 days of intense desalination (b) same sheet after 3 weeks of growth and desalination (courtesy of CRREL).
- Figure 3.8: Porous nature of ice revealed in slice of saline ice sheet of Fig. 3.6 photographed in transmitted light after 5 and a half weeks of desalination and growth.
- Figure 3.9: (a) platelet structure of crystals at depth of 6 cm in 6.5-cm thick ice sheet of Fig. 3.6 after 3 days of growth (b) platelet structure of crystals at depth of 5 cm in 14.5-cm thick ice sheet of Fig. 3.6 after 6 days of growth (courtesy of CRREL).
- Figure 3.10: (a) thermally modified platelet structure in ice from depth of 8 cm in 19-cm thick ice sheet of Fig. 3.6 after 11 days of growth and desalination (b) thermally modified platelet structure in ice from depth of 8 cm in 23-cm thick ice sheet of Fig. 3.6 after 3 weeks of growth and desalination (courtesy of CRREL).
- Figure 3.11: Salinity profile history of saline ice sheet of CRREL'88 experiment.
- Figure 3.12: Temperature profiles of CRREL'88 ice sheet on dates measurements were taken.
- Figure 3.13: Estimated dielectric constant profiles at C band on dates measurements were taken during the CRREL'88 experiment: (a) real component of epsilon (b) imaginary component of epsilon.
- Figure 3.14: Two-way absorption loss at C band as a function of depth into the ice, computed from data of Fig. 3.13.

- Figure 3.15: Desalinated ice blocks as studied during the CRREL'89 experiment.
- Figure 3.16: Porous structure of ice as seen in horizontal thick section from top surface of a desalinated block shown in Fig. 3.15.
- Figure 3.17: Air bubble size distribution in a block of desalinated ice shown in Fig. 3.15.
- Figure 3.18: Temperature profile of saline ice sheet grown during the CRREL'89 experiment, on date measurements were taken.
- Figure 3.19: Salinity profiles of saline ice sheet and desalinated ice blocks on date measurements were taken during the CRREL'89 experiment.
- Figure 3.20: Estimated dielectric constant profiles on dates measurements were taken during the CRREL'89 experiment: (a) real component of epsilon (b) imaginary component of epsilon.
- Figure 3.21: Two-way absorption loss as a function of depth into the ice, computed from data of Fig. 3.20.
- Figure 4.1: Block diagram of X-band SOURCECAT radar (Zoughi, 1984).
- Figure 4.2: Block diagram of the C-band section of PAIR (the X-band section is nearly identical).
- Figure 4.3: Frequency-versus-driving-current response of a typical YIG oscillator (Clark and Swartz, 1971).
- Figure 4.4: Effect of bias level on the impedance of a typical X-band oscillator diode (Clark and Swartz, 1971).
- Figure 4.5: Effect of a spurious YIG-sphere resonance on linearity of a YIG-tuned oscillator (Clark and Swartz, 1971).

- Figure 4.6: Effect of temperature on linearity of a typical heated YIG-tuned oscillator (Clark and Swartz, 1971).
- Figure 4.7: Block diagram of the Ku-band section of STEFRAD (the C-band section is similar).
- Figure 4.8: Vector addition of returns from four targets (Iizuka, 1984).
- Figure 4.9: Relative phase shift encountered by r.f. signal in propagating to target and back, at all 8 frequency steps and various target ranges for an 8-frequency step frequency radar.
- Figure 4.10: Real components of vectors sampled by an 8-frequency step frequency radar for various target ranges.
- Figure 4.11: Imaginary components of vectors sampled by an 8-frequency step frequency radar for various target ranges.
- Figure 4.12: Uncalibrated copolar phase measured by PAIR for several spots on a smooth saline ice surface.
- Figure 4.13: Return from an 8" sphere as output from C-band STEFRAD (a) before and (b) after removal of the system response.
- Figure 4.14: Return from an 8" sphere as output from Ku-band STEFRAD (a) before and (b) after removal of the system response.
- Figure 4.15: Results of C-band copolar phase experiment using inserts of known phase shift.
- Figure 4.16: Results of Ku-band copolar phase experiment using inserts of known phase shift.
- Figure 5.1: Surface profiles for (a) smooth and (b) rough saline ice studied during the CRREL'88 experiment.
- Figure 5.2: Surface profiles for (a) smooth saline ice sheet and (b) desalinated ice blocks studied during the CRREL'89 experiment.

- Figure 5.3: Computed autocorrelations and minimum-mean-square exponential fits for surfaces of (a) smooth saline, (b) rough saline, and (c) desalinated ice sheets studied during the CRREL'88 experiment.
- Figure 5.4: Computed autocorrelations and minimum-mean-square-exponential fits for surfaces of (a) smooth saline ice sheet, and (b) desalinated ice blocks studied during the CRREL'89 experiment.
- Figure 5.5: Computed autocorrelations and ± 1 standard deviation limits obtained from Monte Carlo simulations for surfaces of (a) smooth saline, (b) rough saline, and (c) desalinated ice sheets studied during the CRREL'88 experiment.
- Figure 5.6: Computed autocorrelations and ± 1 standard deviation limits obtained from Monte Carlo simulations for surfaces of (a) smooth saline ice sheet, and (b) desalinated ice blocks studied during the CRREL'89 experiment.
- Figure 5.7: Bubbles in a 3-mm thick section taken from the top of a sample of a desalinated ice block studied during the CRREL'89 experiment, as visually identified in a thick-section photograph.
- Figure 5.8: Autocorrelation of air bubbles in (a) a 3-mm thick horizontal section of the top and (b) 3-mm thick vertical section near the middle of a sample taken from the desalinated ice blocks studied during the CRREL'89 experiment, computed from thick-section photographs that were processed as shown in Fig. 5.7. (Courtesy of CRREL)
- Figure 5.9: (a) roughness and (b) computed autocorrelation of the surface of the snow covering the saline ice sheet on Feb. 3, 1989.
- Figure 6.1: Returns from target and system as seen in range-discriminated outputs of (a) X-band SOURCESCAT (b) Ku-band STEFRAD.

- Figure 6.2: Relative power return at X band from an 8" Luneberg lens as the bistatic angle, θ , is varied (courtesy of P. Racette and R. Forster [1989]).
- Figure 6.3: Backscatter cross-section of smooth (i.e., rms height < 0.1 cm) saline ice sheet at X band, as determined from data obtained during the CRREL'87 experiment.
- Figure 6.4: (a) measured backscatter from artificially grown sea ice at X band and 30 degrees incidence, contrasted with point target return (b) simulation of relative contributions of surface and volume scatter to backscatter from artificially grown sea ice at X band and 30 degrees incidence.
- Figure 6.5: Backscatter cross-section of textured saline ice sheet at X band, as determined from data obtained during the CRREL'87 experiment.
- Figure 6.6: Effect of variation in (a) correlation length and (b) rms height on predictions of the Small Perturbation Method at X band.
- Figure 6.7: Backscatter cross-section of smooth saline ice sheet at C band, as determined from data obtained during the CRREL'89 experiment, compared with Small Perturbation Method predictions.
- Figure 6.8: Backscatter cross-section of smooth saline ice sheet at C band, as determined from data obtained during the CRREL'89 experiment, compared with predictions of a simple layer model.

- Figure 6.9: Effect of snow cover as seen in range-discriminated output of X-band SOURCESCAT during the CRREL'87 experiment. (a) return from bare smooth saline ice surface - peak at slant range of about 3.6m corresponds to surface, (b) broadening effect caused by volume scatter within 15-cm snow cover, and (c) return after 15 cm of loose snow packed to thickness of 7.5cm - peak at 3.4m corresponds to snow surface and peak at 3.8m corresponds to ice surface.
- Figure 6.10: Effect of 6.5cm cover on backscatter cross-section of smooth saline ice at X band, as determined from data obtained during the CRREL'87 experiment, for (a) VV polarization and (b) HH polarization.
- Figure 6.11: Effect of 7cm snow cover on backscatter cross-section of smooth saline ice at C band, as determined from data obtained during the CRREL'89 experiment (see data points on Figs. 6.7 and 6.13).
- Figure 6.12: Backscatter cross-section of snow covered smooth saline ice surface at C band, as determined from data obtained during the CRREL'89 experiment, compared with predictions of the layer model of Ulaby et al. [1982].
- Figure 6.13: Backscatter cross-section of snow covered smooth saline ice surface at C band, as determined from data obtained during the CRREL'89 experiment, and predicted relative contributions of snow surface, snow volume, and ice.
- Figure 6.14: Comparison of backscatter cross-sections of smooth, rough, and desalinated ice at C band, as determined from data obtained during the CRREL'88 experiment (see data points on Figs. 6.15 and 6.16).
- Figure 6.15: Backscatter cross-section of rough saline ice sheet at C band, as determined from data obtained during the CRREL'88 experiment, compared with predictions of the Small Perturbation Method.

- Figure 6.16: Backscatter cross-section of desalinated ice sheet at C band, as determined from data obtained during the CRREL'88 experiment, compared with predictions of the Small Perturbation Method.
- Figure 6.17: Effect of temperature on backscatter from desalinated ice at (a) C band and (b) X band, as determined from data obtained during the CRREL'88 experiment.
- Figure 6.18: Backscatter cross-section of desalinated ice at (a) C band and (b) Ku band, as determined from data obtained during the CRREL'89 experiment, compared with combined predictions of Small Perturbation Method surface and Effective Medium volume scattering theories.
- Figure 6.19: Backscatter cross-section of desalinated ice at (a) C band and (b) Ku band, as determined from data obtained during the CRREL'89 experiment, compared with predictions of the Effective Medium theory at three different values of volume fraction of air.
- Figure 6.20: Backscatter cross-section of desalinated ice at (a) C band and (b) Ku band, as determined from data obtained during the CRREL'89 experiment, compared with predictions of the Effective Medium theory for three different values of the imaginary component of the dielectric constant.
- Figure 6.21: Backscatter cross-section of desalinated ice at (a) C band and (b) Ku band, as determined from data obtained during the CRREL'89 experiment, compared with predictions of the Effective Medium theory for three different values of correlation length of spacing between air bubbles.

LIST OF TABLES

- Table 2.1: Summary of sea ice dielectric constant measurements prior to 1978 (Vant et al., 1978).
- Table 3.1: Scenes observed during the three years of experiments at CRREL.
- Table 3.2: Characteristics of ice sheets observed during the CRREL'88 experiment.
- Table 3.3: Characteristics of ice sheets observed during the CRREL'89 experiment.
- Table 4.1: SOURCESCAT radar specifications.
- Table 4.2: PAIR specifications.
- Table 4.3: STEFRAD specifications.
- Table 5.1: Correlation lengths of air bubbles in a sample taken from a desalinated ice block studied during the CRREL'89 experiment, computed from thick-section photographs that were processed as shown in Fig. 5.7.
- Table 5.2: Volume fraction profile of air in the desalinated ice blocks observed during the CRREL'89 experiment, computed from estimated air bubble density and size distributions, and a bulk density measurement.
- Table 6.1: Estimated measurement and fading uncertainties (in dB) for the three years of experiments.

1.0 Introduction

The Arctic region has attracted considerable attention in recent years for several reasons. The study of sea ice as an indicator of global climate is among the most important scientific reasons. Commercially, the Arctic offers a wealth of mineral resources which will undoubtedly be exploited as those in the temperate regions become scarce.

This region has remained largely unexploited, however, because of its uninviting environment. Weather can be severe, sunlight is absent for several months, and in some areas sea ice is always present, making navigation hazardous and often impossible.

A knowledge of the morphology, extent, and dynamics of sea ice is essential to successful exploration and development of the Arctic and Antarctic regions and to better understanding of long-term global climatic changes. Since the long polar winters and frequent cloud cover limit the utility of visible and infrared sensors, microwave remote sensing has long been used as an ice-surveillance tool. Microwave systems can see through clouds and darkness and are thus suited for this task.

Microwave sensors fall into two major categories: passive sensors that monitor inherent black-body radiation; active sensors that monitor reflected

radiation [Thomas, 1986]. Because of the easy access to passive microwave data from satellites, radiometers have been well tested for monitoring areal ice concentration and surface wetness. Radar, especially synthetic aperture radar (SAR), is generally more suited for determining ice types, surface features, and movement, because of its finer resolution. The principal disadvantage of SAR is the high rate of data acquisition. Radar altimeters may also provide estimates of the ice edge and areal ice concentration. Much research currently underway is aimed at determining what information can be obtained from microwave sensors, optimum parameters for the sensors, and methods of automatically interpreting the data gathered by the sensors. This research is of great importance in light of the present operation of the Soviet Kosmos 1870 SAR and the approaching deployment of the European Space Agency (ESA) Earth Remote Sensing (ERS-1) satellite, slated for launch in the early 1990's, Canadian RADARSAT, Japanese JERS-1, and the Earth Observation System (EOS), scheduled for the mid-1990's.

1.1.0 Background

1.1.1 History of remote sensing of sea ice

Radar was used for experimental mapping of Arctic ice as early as 1962, when the U.S. Army Cold Regions Research and Engineering Laboratory (CRREL) flew a Side-

Looking Airborne Radar (SLAR) over Arctic pack ice [Anderson, 1966]. In his analysis of the data, Anderson showed that ice types can be identified from SLAR imagery. To verify the potential of radar to discriminate between ice types, the National Aeronautics and Space Administration (NASA), Naval Oceanographic Office, and CRREL conducted a joint experiment over the Arctic with a 13.3 GHz scatterometer in 1967 [Rouse, 1969]. In 1968, the Naval Oceanographic Office flew an X-,C-,L-,P-band multifrequency SLAR over the ice fields north of Alaska [Ketchum and Tooma, 1973]. In their report, Ketchum and Tooma concluded that X-band holds the greatest potential for sea ice mapping, determining the stage of ice development and for fracture- pattern analysis. They also concluded that L-band sees only more prominent features such as ridges and hummocks. In 1969, the U.S. Coast Guard conducted ice mapping experiments in the Northwest passage using a Ku-band, unfocussed synthetic- aperture radar (SAR) [Johnson and Farmer, 1971]. In their report, Johnson and Farmer concluded that the ice concentration, ice-floe size and number, and water openings are readily determined from SLAR/SAR images. They further concluded that, through careful analysis, the age of ice, drift, surface topography, fractures, and pressure ridge characteristics can be discerned to varying degrees.

Others involved in the early years in investigating the potential for microwave radar as a sea ice mapping tool include the Soviets, who in the early 1970's, reported on sea ice measurements conducted with the TOROS SLAR [Glushkov and Kamarov, 1971; and Loshchilov and Voyevodin, 1972].

Operational use of such radars started in the early 1970's. For example, airborne and spaceborne radars have been used to monitor ice on the Great Lakes [Hagman, 1976; and Gedney et al., 1975], and along the Alaskan coast [Gedney et al., 1977] to assist navigators; and the Soviets reportedly used data from the TOROS SLAR to provide sea ice maps to navigators and fishermen [Loshchilov et al., 1978]. To improve their operational capability many field experiments were and are being conducted, during the 1970's and 1980's, in the Arctic and, more recently, in the Antarctic. Most experiments were conducted along ice edges or in marginal ice zones because the processes in these regions impact importantly on global climate and also greatly influence oil and mineral exploration, naval operations and commercial fishing [Luther, 1988]. Major field experiments of the 1970's included the Arctic Ice Dynamics Joint Experiment (AIDJEX) in the Beaufort Sea [Gray et al., 1977; and Campbell et al., 1978], the joint U.S.- U.S.S.R. Bering Sea Experiment (BESEX)

[Gloersen et al., 1975; and Ramseier, 1975], and the Norwegian Remote Sensing Experiment in the Norwegian Sea [Matzler et al., 1984; and Svendsen et al., 1983]. Similar experiments conducted in the 1980's include the Marginal Ice Zone Experiment (MIZEX) in the Bering and Greenland Seas ([Luther, 1988; and Shuchman et al., 1988]), the Labrador Ice Margin Experiment (LIMEX) in the Labrador Sea [McNutt and Raney, 1988], and the Bothnian Experiment in Preparation for ERS-1 (BEPERS) in the Baltic Sea [Hallikainen et al., 1988]. The role of remote sensing in these experiments is two-fold: 1) to provide synoptic data; and 2) to improve understanding of interaction between electromagnetic radiation and the ice/ocean surface.

Because field conditions have been found to be highly variable, a laboratory program was established at the U.S. Army Cold Regions Research and Engineering Laboratory (CRREL) in Hanover, New Hampshire in the early 1980's to examine the interaction between electromagnetic radiation and sea ice.

Research on microwave remote sensing of sea ice has proceeded, during the 1970's and 1980's, along a number of fronts: (1) determination of the scene parameters that can be extracted from backscatter measurements; (2) development of procedures for automatically extracting scene parameters; and (3) improvement of our

understanding of microwave interactions with sea ice. The latter is considered in some detail in Chapters 2 and 6.

1.1.1.1 Determination of scene parameters

Sea-ice parameters that are desirable to measure include:

- 1) Thickness
- 2) Areal concentration
- 3) Ice type
- 4) Surface conditions
- 5) Floe size and movement
- 6) Location of leads and polynyas
- 7) Location of the ice edge

Radio-frequency techniques have been used to determine ice thickness (and, thus, ice type). Knowing of the application of r.f. techniques to study glaciers, V. Bogorodsky and V. Rudakov suggested in 1956 that similar methods be used for measurements of the thickness of sea ice and fresh water ice [Bogorodsky, 1978]. Finkelstein and Kutev [1972] used video pulses of nanosecond duration and repetition rates of a few tens of MHz and found that ice with salinity of 10 - 130/00 could be penetrated to depths of .75 to 1.5m. Wadhams et al. [1987] reported on the use of a 100 MHz impulse radar to determine ice thickness in the Atlantic sector of the Antarctic Ocean. VHF techniques are of

limited usefulness from spacecraft, however, because adequate gains are not achievable using reasonable-size antennas, and because of ionospheric propagation effects. Since GHz-frequency signals penetrate only a few cm into first-year ice and undergo considerable volume scatter in multiyear ice, they are not useful for direct thickness measurements except for very thin ice.

The topic of areal ice concentration has been thoroughly addressed. Many papers have been written on concentration estimation from passive microwave data; e.g., [Alfultis and Martin, 1987]; [Carsey, 1982]; [Cavalieri et al., 1986]; [Gloersen and Campbell, 1988]; [Comiso and Sullivan, 1986a]; and [Comiso, 1986b]. Others were directed toward concentration estimation from radar data; e.g., [Loschilov et al., 1978]; [Comiso, 1986b]; and [Wackerman et al., 1988]. A few papers directly compare the two methods; e.g., [Burns et al., 1987]; [Martin et al., 1987]; and [Steffen and Maslanik, 1988]. The accuracy of the estimates of ice and open water have been reported to be between 5% and 13% depending on whether the measurements were near the ice edge or in the ice pack. The schemes used to obtain the estimates consisted of a ratio of polarization ratios for the passive devices, and modal analysis of histograms of local statistics for the active devices.

The problem of classifying ice types in winter

conditions using microwave emission and backscatter measurements occupied the attention of many experimenters. Rouse [1969] indicated the potential use of 13.3 GHz scatterometer data to discriminate between old and new ice. In 1971, as a part of the Arctic Ice Dynamics Joint Experiment (AIDJEX), airborne measurements of microwave emission between 0.3 and 3.0cm were combined with extensive surface-comparison measurements to further investigate similar potential for passive devices [Gloersen et al., 1973]. Using rather crude images from a 16.5 GHz SLAR, Parashar [1974] classified ice types according to image intensity as: (a) open water, (b) thin first-year ice, (c) thick first-year ice, and (d) multiyear and very thick first-year ice. Similarly, using SLAR data, Loschilov et al. [1978] were able to classify ice types according to (a) new ice and nilas, (b) pancake, (c) grey, (d) grey-white, and (e) multiyear ice. From both 13.3 GHz scatterometer and SLAR data Gray et al. [1977] determined that the typical contrast between first-year and multiyear ice is 8 - 10 dB for like polarization and 15 - 18 dB for cross polarization. More recently it has been reported that emission data at 33.6 GHz can be used to distinguish between open water, frazil, old ice, and young first-year ice [Eppler et al., 1986].

Using data collected by a surface-based

scatterometer in the Beaufort Sea, Onstott et al. confirmed that $\sigma^0(\theta)$ can be used to discriminate thick first-year (FY) ice from multiyear (MY) ice [Onstott et al., 1979a; Onstott and Delker, 1979b; and Onstott, 1980]. They also confirmed that the contrast between MY and FY ice is greater for cross-polarization than it is for like-polarization. Kim, Onstott and others concluded that the most effective discrimination of FY from MY occurs for: (a) microwave frequencies between 8 and 18GHz, and (b) incidence angles greater than 30° . The least-effective frequencies studied were between 1 and 2GHz [Kim, 1984a; Kim et al., 1985; Onstott et al., 1979a; Onstott and Delker, 1979b; and Onstott, 1980].

A combination of frequencies can reduce ambiguity. Using 400MHz and 13.3GHz data collected over Alaska during a NASA Earth Resources Aircraft Program mission, Parashar [1974] determined that the 400MHz data helped to eliminate the MY/thin-FY ice ambiguity observed in the 13.3GHz data. Cluster analysis of brightness temperatures at two and three different frequencies has also proven to be useful in discrimination; e.g., [Comiso and Sullivan, 1986a]; and [Comiso, 1986b]. Using 18 and 37 GHz radiometer data obtained by the NASA CV-990 over the Bering Sea, Cavelieri et al. [1986] were able to distinguish among new, young, and first-year ice. Rothrock et al. [1988] did a principal-

component analysis on 10 channels of sea ice data collected by the Nimbus 7 SMMR and determined that 2 or 3 of the channels explained most of the data.

Some experimenters have combined simultaneous active and passive microwave measurements in attempts to improve discrimination between ice types. Gray, Hawkins, and Livingstone combined emissivity data at 19.4GHz, H-polarization and 45° incidence, with 13.3GHz like- and cross-polarized backscatter data [Gray et al., 1982; Hawkins et al., 1980; and Livingstone et al., 1980]. They concluded that a combined scheme improved classification of sea-ice types and conditions. Kurskaya and Kutuza [1984] stated that radiometric measurements aided in interpreting SLAR images.

Experimenters have determined that ice classification is possible during winter months; the problem is much more difficult during the summer season due to surface melting. Using data from the Mould Bay 1982 experiment, Nimbus 5, and Seasat (July-October 1978), Carsey concluded that the summer values of backscatter and brightness temperature are controlled by surface morphology and wetness [Carsey, 1985]. L-, C-, X-, and Ku-band scatterometer data collected at Mould Bay 1982 by Onstott and Gogineni showed reductions and even reversals in contrast between FY and MY ice because of the melting [Onstott and Gogineni, 1985; and Gogineni,

1984]. They concluded that lower frequencies, such as L-band, are slightly better for discriminating between ice types during the melt season. In a nutshell, a fully reliable method of classifying ice by remote sensing techniques during summer has not been found.

Ambiguity in interpretation can also occur in the winter months, but not to the same extent. For example, thin ice can be misinterpreted as multiyear ice [U.Kansas], and snow cover can greatly alter the backscatter from sea ice [Kim, 1984b; and Lohanick and Grenfell, 1986].

The ability to track moving ice is important because of the hazards it presents and to map Arctic ocean currents. Curlander et al. [1985] used an ice-feature tracking scheme to study ice movement between successive Seasat SAR images. They determined mean displacements of 15.3km/day in the marginal ice zone and 5km/day in the central ice pack with an overall error of 150-200m. Fily and Rothrock [1987] used a scheme of nested correlations to track sea ice movement. Their technique consisted of correlations at several levels of resolution from coarse to fine. The fine-resolution correlations are driven by the results of coarse-resolution correlations. Ninnis et al. [1986], and Collins and Emery [1988] sought to optimize the correlation technique by using a matched-filtering

approach. Vesecky et al. [1986] discussed the use of both the ice-feature tracking technique and the nested-correlation technique. Shuchman et al. [1986] used sequential SAR images to study the interactions of sea ice, ocean, and atmosphere. Fily and Rothrock [1986] studied lead-area changes in successive SAR images.

The ability to delineate geometric shapes can also be advantageous. For example, ridges and icebergs can be hazardous to navigation. Askne and Johansson [1988] tried to determine the ridge characteristics that can be discerned from radar by using a stochastic triangular model for ridges. Larson et al. [1978] considered the use of SAR systems for iceberg detection and characterization. Using data collected by an X-/L-band SAR at depression angles of 10° and 30° they concluded that it is possible (1) to detect icebergs in a variety of sea clutter, (2) to identify icebergs by shape, and (3) to estimate size from shadow information. Gray [1980] similarly concluded that large incidence angles enhance the detectability of ridges and other objects, such as icebergs, in an open sea or when surrounded by sea ice. Shaw et al. [1988] used data obtained off the coast of Newfoundland to study for example, the relationship of iceberg responses to incidence angle and the look direction relative to predominant wave direction. Wadhams [1988] used shipboard radar to

monitor icebergs in the south Atlantic, and Walsh et al. [1986] determined that ground-wave radars are effective ice-hazard sensors. Marthaler and Heighway [1978] discussed radar image processing of SLAR data for detection and identification of icebergs.

In recent years, considerable emphasis has been placed on polarimetric measurements: (1) to determine if useful sea-ice target information is contained in the copolar phase; and (2) so that targets can be further studied via the technique of polarization synthesis. During the last few years such measurements have been made at CRREL; e.g., [Onstott et al., 1988]. In addition, the Jet Propulsion Laboratory (JPL) has recently imaged sea ice regions north of Alaska with a P-, L-, and C-band polarimetric SAR. Analysis of these images is still in progress.

1.1.1.2 Automatically extracting scene parameters

The routines discussed in the previous section for tracking ice movement were, out of necessity, at least partly automated. Considerable work has also been done on developing automated routines for ice-type classification. Holmes et al. [1982] developed a digital procedure for ice-type discrimination. Their method reduces the speckle effect frequently found in SAR images, without visibly degrading the edges of the different ice types. It uses a nonlinear isotropic

filtering technique called neighborhood processing. Lyden et al. [1982] considered the importance of textural differences between ice types. Having found evidence that the image statistics of FY ice differ from those of MY ice, they considered hypothesis-testing techniques for the different probability distributions of different ice-types. Fily et al. [1986] discovered that they could reliably discriminate open water from thin ice via a bivariate distribution of brightness and variance. Wackerman et al. [1988] presented routines to determine ice concentration and to classify sea-ice types. The ice- concentration algorithm is an iterative scheme that fits the observed histogram to the weighted sum of the probability density functions (pdfs) of open water and ice. The ice- classification routine consists of a modal analysis of histograms of local statistics. Bogorodsky and Darovskih [1984] and Murthy and Haykin [1987] developed Bayesian classification schemes. Murthy also discussed nonparametric classification and multilevel thresholding techniques. Parashar [1974] tested a similar technique, developing a decision rule on the basis of information in a training-data set. Using 7 categories, he found that this routine interpreted 66% of the remaining data set correctly. Raizer et al. [1986] used numerical models of emission characteristics to retrieve thickness, temperature,

salinity, and density. The program "iceman" has been developed at the Jet Propulsion Laboratory to classify ice types, and to study ice surface texture and ice motion [Lee, 1988].

1.2 Organization

This thesis is organized into 7 chapters. A brief outline of each is presented here.

An overview of sea ice structural and dielectric properties and a review of scattering theories being used to interpret microwave backscatter from sea ice are the subjects of Chapter 2.

Chapter 3 consists of a description of backscatter measurements and surface characteristics obtained during three years of experiments at CRREL. Backscatter measurement techniques are described, including spatial sampling and calibration procedures. Emphasis is placed on surface characterization, including a description of temperature and salinity profiles, surface roughness parameters, inhomogeneities, and snow cover parameters.

Radar system development and performance is the subject of Chapter 4. FM-CW radars are commonly used as short-range scatterometers. Even with high quality YIG oscillators, the performance of these radars is limited due to amplitude and residual frequency modulation effects of the oscillator. Several reasons for the residual FM and the steps we took to reduce its effect

are presented. Other aspects of our FM-CW polarimetric radar are also presented. A comparison of the performance of this radar and a step frequency radar is given, as is a technique for determining copolar phase.

Chapter 5 includes a discussion of analysis of ice surface truth data. Included are computation of autocorrelations for surface and volume parameters. Simulations are done to illustrate uncertainty in the autocorrelation data. Consideration is also given to statistics of the inhomogeneities in the desalinated ice.

A comparison of results with theory is the subject of Chapter 6. Measured surface parameters are used in the small perturbation and Kirchoff (scalar approximation) surface scatter models to generate confidence intervals with which to compare saline ice backscatter data. The results and a simple model are used to show that the volume scatter contribution is important for very smooth saline ice surfaces. The return from desalinated ice is modelled as a sum of surface and volume scatter contributions. Surface scatter is modelled with the above-mentioned models; the volume scatter contribution is modelled with a dense medium theory. Snow cover for saline ice is modelled as in Ulaby et al. [1982].

General conclusions and recommendations for future

research are given in Chapter 7.

2.0 Background

2.1 The dielectric properties of sea ice at microwave frequencies

An extensive literature search was conducted to survey the current knowledge of the electrical properties of sea ice. Because so much work, both theoretical and experimental, has been done, only an overview is presented here. For a thorough discussion of the subject see Vant [1976] and Arcone et al [1986b].

Because the electrical properties of sea ice depend strongly on morphology, we first give a description of the formation and morphology of sea ice.

2.1.1 Formation and morphology of sea ice

Sea water consists primarily of H_2O , Na^+ and Cl^- with smaller percentages of SO_4^{2-} , Mg^{2+} , Ca^{2+} and K^+ . The maximum salinity (in grams of dissolved solids/kg of solution) of ocean water is about 350/00 but may be lower, depending upon dilution with fresh water. Figure 2.1 indicates the change in the sea water make-up as ice forms to equilibrium at given temperatures. The solution consists of pure ice and brine down to approximately $-24^\circ C$; at colder temperatures $NaCl$ (the principal salt) precipitates.

If sea water is cooled slowly enough, complete separation of ice and brine can occur. This rarely happens in nature, especially in the polar regions,

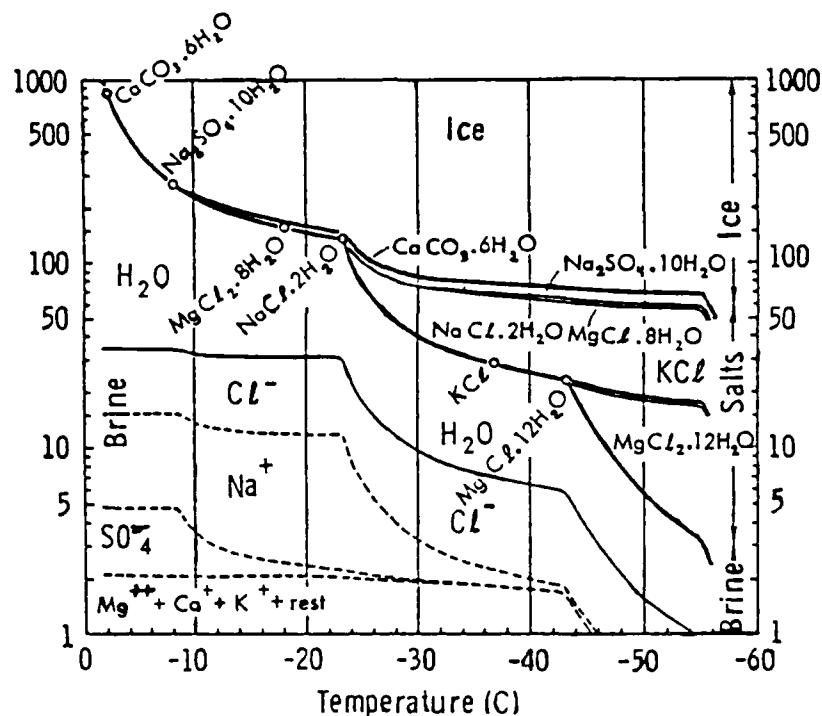


Figure 2.1: Phase relations for "standard" sea ice. Circles on the brine-salt line indicates temperatures at which solid salts precipitate (Assur, 1958).

where ice formation occurs rapidly enough to allow considerable amounts of brine to be trapped within the ice structure. The amount trapped depends largely on the rate of ice growth [Nakawo and Sinha, 1981]; the primary entrapment occurs at interplatelet boundaries within individual crystals composing the ice structure.

The simplest ice structures consist of two layers as shown in Fig. 2.2. The consistency and depth of the upper layer is dictated primarily by the cooling rate and turbulence in the water. The lower layer

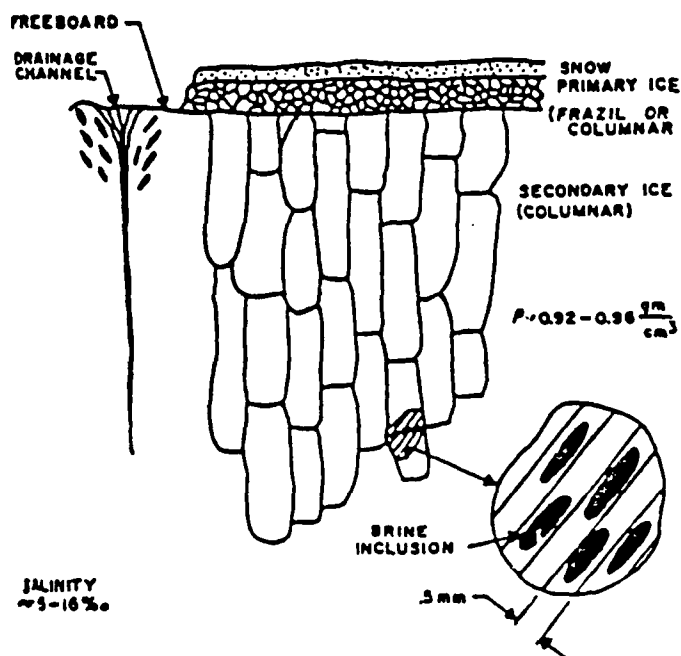


Figure 2.2: Simplified geometry of first-year sea ice (Vant et al., 1978).

preferentially grows as long columnar crystals, each crystal consisting of similarly oriented platelets [Martin, 1979].

When the sea surface is calm and rapidly cooled, the water crystallizes in small, needle-like shapes. These rapidly change to circular disks which reach a diameter of no more than 2 to 3 mm [Weeks and Assur, 1969]. Under these conditions the upper layer continues to a depth of 1 to 2 cm.

When a cold wind blows over sea water that has a

temperature near freezing, the water is stirred and ice crystals of 1 to 10 μm in thickness and 1 to 2 mm in diameter form in the water column. These crystals float to the surface and form a porous mass with a random crystal structure [Martin, 1979]. This type of ice, referred to as frazil, can form to thicknesses of up to 1 m.

Ice similar in structure to frazil forms when snow falls into sea water that is supercooled. Further cooling causes the ice crystals formed from the snow to congeal into slush ice. This type of ice can also form layers up to about 1 m thick.

The locations of the brine inclusions within the ice structure are illustrated in Fig. 2.2. Typical brine- pocket dimensions in the columnar ice are on the order of 0.05 mm [Anderson, 1960; Pounder, 1965] in diameter and 2 to 3 cm in length [Pounder, 1965; Addison, 1969]. Deep within the ice the brine pockets are elongated vertically.

The brine content of sea ice is not static, however. During the first few days after the ice forms, the brine content of the ice can decrease dramatically; this decrease is a first-generation desalination process. Ice that has only undergone this type of desalination is referred to as first-year ice. Increased temperatures and melting, leading to

formations of melt ponds during the spring and summer months, cause additional reduction in the ice brine content of the ice; this decrease is second-generation desalination. Ice that has undergone at least one season of this type of desalination is generally referred to as multiyear ice.

First-generation desalination in winter ice is illustrated in Fig. 2.3 - notice the magnitude of the salinity decrease that occurred during the week after the ice formed. Four mechanisms to explain salinity decrease in sea ice have been presented by Untersteiner [1968]: (1) brine pocket diffusion, in which a salinity gradient causes continuous preferred melting of the brine pocket boundary; (2) gravity drainage; (3) flushing; and (4) expulsion, caused by pressure build-up within a brine pocket as cooling occurs. The brine pocket diffusion hypothesis is not considered significant due to the rapid rate at which desalination occurs. The gravity drainage explanation is believed to be a significant mechanism over the long term. The flushing mechanism, due primarily to snow melt at the ice-snow interface, is important during the spring and summer but is not effective at the temperatures encountered during the growth of winter sea ice sheets. Expulsion has been proposed as the dominant first-generation desalination mechanism [Untersteiner, 1968].

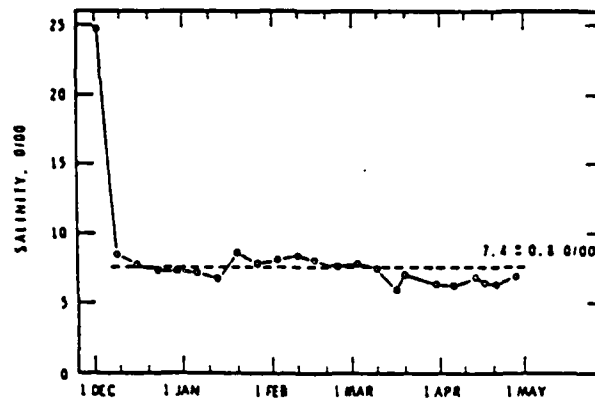


Figure 2.3: Variation of salinity with time for 2.5 cm sections of ice at a depth between 40 and 42.5 cm. Broken line indicates "stable" salinity or average of all the salinities except the initial high value at this level (Nakawo and Sinha, 1981).

Expulsion can be explained as follows: further cooling after initial brine pocket formation causes water to freeze out of the trapped brine leaving a more concentrated brine and a smaller pocket; the increased pressure due to volume reduction forces brine out of the pocket.

A typical salinity profile for first-year ice is shown in Fig. 2.4 - notice that the curve is C-shaped. Brine expulsion from very thin ice causes a thin (few tenths of a mm) high salinity (reported to be as high as

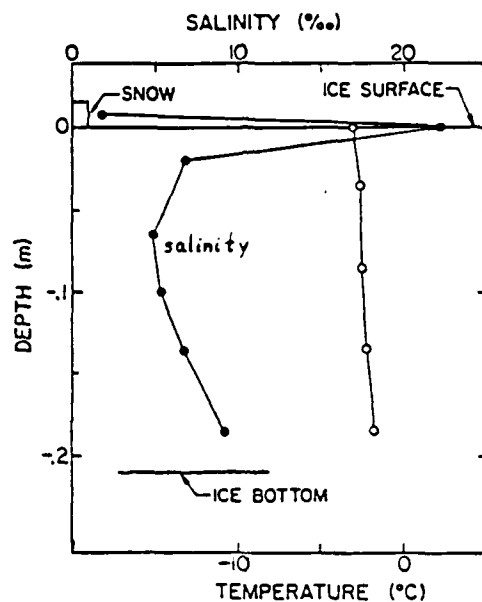


Figure 2.4: Salinity and temperature profiles of a typical frazil ice core (Martin, 1979).

950/00 (Martin, 1979)) layer to form on the ice surface. The salinity of the ice within a few cm of the ice-water interface is influenced largely by the brine content of the underlying water. The salinity of the intermediate structure is primarily dependent on the growth history and, apparently, also on the ice structure. Nakawo and Sinha [1981] indicate that fine-grained ice retains more brine than columnar-grained ice for a given growth history.

First-year ice can reach a thickness of up to about

2 m [Parashar, 1974]; before it attains a greater thickness, the ensuing spring and summer bring about bulk structural and salinity changes. Spring temperatures cause melting at the ice surface, both of the snow cover and of the ice itself, resulting in an altered terrain. The warmer temperatures and free surface water cause the brine drainage channels to grow and expand (See Fig. 2.5). These are present, but poorly developed, in cold first-year ice. The result is that the meltwater flushes brine from the ice. This second-generation desalination results in a salinity profile typical of that shown in Fig. 2.6. Also this flushing of brine pockets, and entrapped air in the snow layer, cause air bubbles to replace brine down to the freeboard level. The resultant ice, ice which may persist for many years, is referred to as multiyear ice, and can reach thicknesses of several meters.

2.1.2 Electrical properties of sea ice

Dielectric measurements have been made at a variety of frequencies, salinities, and temperatures. Vant et al., [1978] tabulated the conditions under which many of these measurements were made and commented on the techniques used (See Table 1.1). Since 1978, other experimenters have contributed: Troy [1981] conducted dielectric measurements at 90 GHz and below; Timco [1979] studied the in-situ resistivity of sea ice; and

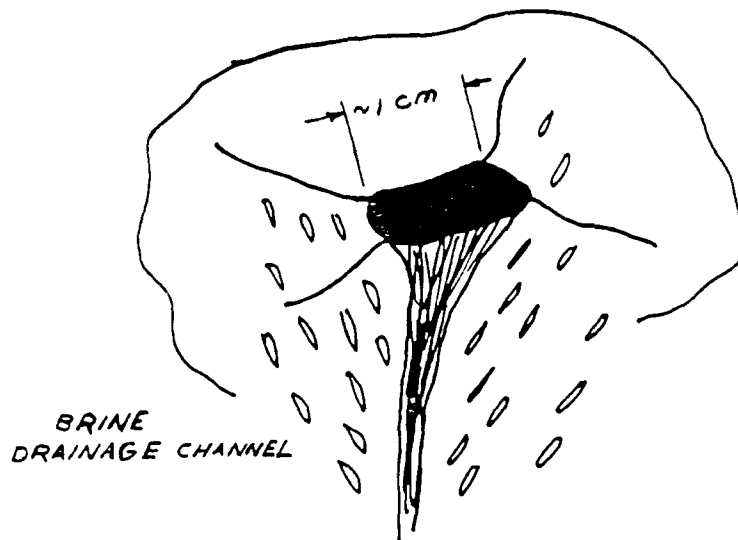


Figure 2.5: Conceptual view of a brine drainage channel (Vant, 1976).

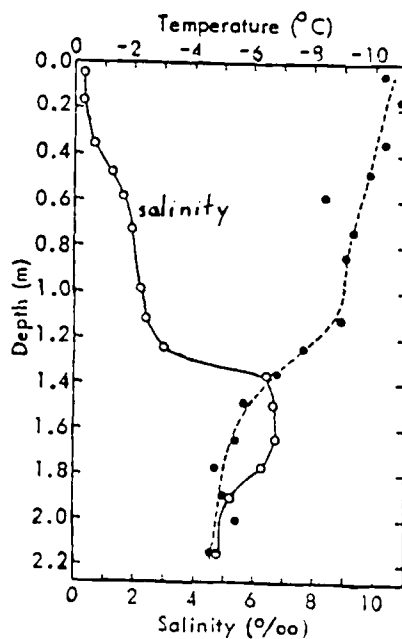


Figure 2.6: Temperature and salinity profiles for typical multiyear sea ice (McNeill and Hoekstra, 1973).

Frequency	Salinity (‰)	Temperature (-°C)	Comments	Author
20 Hz to 100 MHz	7-20	22	Artificial sea ice Special cell used	Addison and Pounder
20 Hz to 100 MHz	4-20	12.5-35	Special cell used, Sillars—dielectric model evaluated	Addison
1 kHz	From saline water 35‰	25-150	Special cell used	Addison <i>et al.</i>
30, 60, 100, 200, and 400 MHz	0.56, 4.4, 8.6, and 17.0	10-40	Sea water frozen in coastal air line, poor facsimile	Bogorodsky and Tripol'nikov
100 MHz	3.5, 0.7, and 0.35	10-70	...	Cook
100 MHz to 24 GHz	6, 8, and 10	0-80	Flash frozen sea water, poor facsimile, conducting spheres, dielectric model	Hoekstra and Cappillino
10 GHz	10-60	0-25	NaCl ice	Hoekstra
31.4 and 34 GHz	7.8	7	Free-space measurement	Vant <i>et al.</i>
100 Hz to 50 kHz	11, 13, and 15	5-70	Natural sea ice	Fujino
0.1-30 MHz	0.067-23	5-40	Possibly severe brine drainage	Wentworth and Cohn
150, 300, 500, and 1000 MHz	...	1-60	Very low salinity	Ragle <i>et al.</i>
400, 200, 400, 800, 1000, 2000, and 4000 MHz	1.32-10.5	5, 10, 15, 20, 25, 30, and 40	Large number of samples	This work and Vant
75 GHz	4.1-7.5	(as above)	Multiyear and first-year ice, several dielectric models discussed	
10 GHz	0.60-4.4	70-80	Differentiation of ice types, simple dielectric models discussed	Vant <i>et al.</i>
10 GHz	2.5-7.5	1-13	Good survey of ice types	Bogorodsky and Khokhlov
26-40 GHz	2.85, 3.40, and 7.20	7, 16.5, 21.5, 25, and 32		Sackinger and Byrd

Table 2.1: Summary of sea ice dielectric constant measurements prior to 1978 (Vant *et al.*, 1978).

Arcone [1986a] examined the dielectric properties of saline ice at microwave frequencies.

In the frequency range of 1 - 18 GHz, the real and imaginary components of the dielectric constant generally decrease with frequency. This is primarily because the large dielectric constant of brine decreases with frequency over this range (See Fig. 2.7).

Hallikainen [1982] derived a set of multipliers to describe the change of the real and imaginary components of the dielectric constant as a function of frequency:

$$\begin{aligned}\epsilon'(18 \text{ GHz}) &= 0.98\epsilon'(5 \text{ GHz}) = \\ 0.93\epsilon'(1 \text{ GHz}) &= 0.86\epsilon'(0.5 \text{ GHz})\end{aligned}\quad (2.1)$$

$$\begin{aligned}\epsilon''(18 \text{ GHz}) &= 0.92\epsilon''(5 \text{ GHz}) = \\ 0.61\epsilon''(1 \text{ GHz}) &= 0.46\epsilon''(0.5 \text{ GHz})\end{aligned}\quad (2.2)$$

Vant [1976] determined the dielectric constants for many cores taken during the Arctic Ice Dynamics Experiment (AIDJEX) and found a decrease in both real and imaginary components as a function of temperature; his measurements were at 1 - 4 GHz and salinities of 4 to 90/00. The real component decreased from about 3.7 to 3.2, and the imaginary component decreased from about 0.4 to 0.03 over the range of -5° to -40°C. These results are not surprising considering that the amount of liquid in the brine in the ice varies directly with temperature.

The dielectric constant of sea ice is not isotropic. Vant et al. provide many curves to

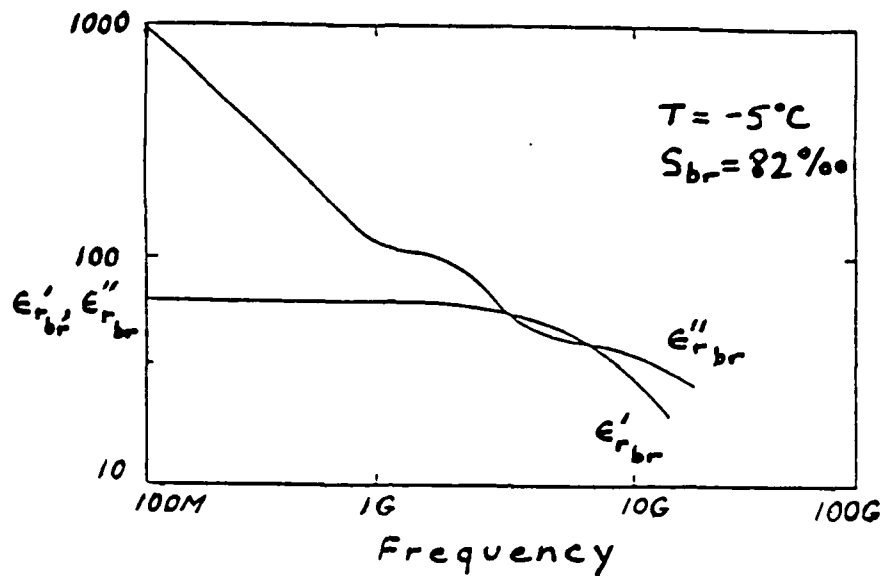


Figure 2.7: Real and imaginary parts of the relative dielectric constant of brine (Vant et al., 1978).

illustrate the effect of brine pocket orientation on the dielectric constant, as predicted by theory [Vant, 1976; and Vant et al., 1978].

The dielectric constant of sea ice has been modeled, both empirically and theoretically. Vant et al. attempted to include the available knowledge on the subject into a comprehensive semi-empirical model [Vant, 1976; and Vant et al., 1978]. The empirical components of the model relate the relaxation time, static dielectric constant, and conductivity of the

brine to temperature and frequency. They also relate brine volume to salinity, temperature, and density. The theoretical components consist of the Debye equations for brine and ice, to determine the corresponding dielectric constants, and a mixture equation. The latter comes from a solution to Laplace's equation for an arbitrary spheroid (quasi-static approximation).

This comprehensive model performs well for FY ice but has not performed well to date on MY ice due to the variable density of MY ice and also because the shapes of brine inclusions in MY ice are not well understood [Vant, 1976; and Vant et al., 1978].

This model works well in the range 400 MHz - 7.5 GHz but is lengthy and requires a detailed knowledge of the ice structure. For many purposes a simple empirical model is adequate. The form of the model Vant proposed is

$$\begin{aligned}\epsilon' &= a + bV_{br} \\ \epsilon'' &= c + dV_{br}\end{aligned}\tag{2.3}$$

where a, b, c , and d are constants, and V_{br} is the brine volume. V_{br} can be determined using empirical equations developed by Frankenstein and Garner [1967]:

$$V_{br} = S((-49.185/T) + 0.532) \text{ parts per thousand}, \tag{2.4}$$

where S and T are measured salinity and temperature.

The constants a, b, c , and d as determined by Vant are:
 $a = 3.05$, $b = .0072$, $c = .024$, $d = .0033$ at 4 GHz

$a = 2.46$, $b = .0224$, $c = .006$, $d = .01$ at 10 GHz. The dielectric constants at other frequencies can be estimated from equations (2.1) and (2.2) above.

The empirical equations are used throughout this paper.

2.2 Theories used in remote sensing of sea ice

Many surface- and volume-scattering theories have been applied to the problem of understanding and interpreting microwave backscatter from sea ice. The most commonly used surface scattering theories are the Kirchhoff (scalar approximation) and small perturbation methods. Both analytical wave and radiative-transfer methods have been used to model the volume-scattering component.

2.2.1 Review of surface scattering theories

2.2.1.1 Kirchhoff surface scattering theory

The Kirchhoff scattering theory is a physical optics approach; i.e., it is based on vector second Green's theorem which states that the scattered field at any point within a source-free region bounded by a closed surface can be expressed in terms of the tangential fields on the surface [Ulaby et al., 1982]. The development begins with (Pg. 926 of [Ulaby et al., 1982]):

$$\vec{E}^s = K\vec{n}_s \times \int ([\vec{n}_s \times \vec{E} - \eta_s \vec{n}_s \times (\vec{n}_s \times \vec{H})]) \exp(jk_s \vec{r} \cdot \vec{n}_s) dS \quad (2.5)$$

where $K = -jk_s \exp(-jk_s R_0) / 4\pi R_0$

\hat{n}_s = unit vector in scattered direction

\hat{n} = unit vector normal to the interface inside the medium in which scattering is being considered

η_s = intrinsic impedance of the medium in which E_s is evaluated

k_s = wave number of the medium in which \vec{E}^s is evaluated (e.g., k_1 in medium 1)

R_0 = range from the center of the illuminated area to the point of observation

\vec{E}, \vec{H} = total electric and magnetic fields on the interface

Assume a plane wave of the form $\vec{E}^i = \hat{a} E_0 \exp(-jk_1 \hat{n}_i \cdot \vec{r})$ incident on the surface and a coordinate system which includes local surface slopes; e.g., $\vec{t} = \hat{n}_i \times \hat{n} / |(\hat{n}_i \times \hat{n})|$, $\vec{d} = \hat{n}_i \times \vec{t}$, and $\hat{n}_i = \vec{t} \times \vec{d}$.

The theory is developed assuming that the fields at a point on the surface can be expressed as the sum of incident and reflected fields, where reflected fields are related to the incident fields via the Fresnel reflection coefficient. This implies that the surface radius of curvature is sufficiently large (locally) that the Fresnel reflection coefficient is applicable.

More approximations are then made assuming other physical characteristics of the surface. For surfaces that have small slopes a scalar approximation is used.

In the scalar approximation the slope terms in \vec{t} and \vec{d} are ignored; and the reflection coefficient, which is dependent on surface slope, is expanded in a Taylor series with respect to the slope terms. \vec{E}^s can then be expressed in the form

$$\vec{E}^s = \int U_{pq} \exp(jk_z (\vec{n}_s - \vec{n}_i) \cdot (\vec{r} - \vec{r}')) dS' \quad (2.6)$$

where U_{pq} is of the form

$$U_{pq} = a_0 + a_1 Z_x + a_2 Z_y \quad (\text{Pg. 937 of [Ulaby et al., 1982]}).$$

An ensemble average of

$\vec{E}^s \cdot \vec{E}^{s*}$ results in a series of terms, the first of which is

$$\begin{aligned} I &= |a_0|^2 \int_{-L}^L \int_{-L}^L \int_{-L}^L \int_{-L}^L \exp(jq_x(x' - x'') + jq_y(y' - y'')) \\ &\quad \times \langle \exp(jq_z(z(x', y') - z(x'', y''))) \rangle dx' dy' dx'' dy'' \\ &= |a_0|^2 \int_{-2L}^{2L} \int_{-2L}^{2L} [(2L - |u|)(2L - |v|) \exp(jq_x u + jq_y v) \\ &\quad \times \exp(-q_z^2 \sigma^2 (1 - \rho))] du dv \end{aligned} \quad (2.7)$$

where q_x, q_y, q_z are propagation constants, $2L \times 2L$ is the illuminated area, and ρ is the correlation function.

Note that the $\exp(-q_z^2 \sigma^2 (1 - \rho))$ term was obtained from $\langle \exp(jq_z(z(x', y') - z(x'', y''))) \rangle$ assuming that $z(x', y')$ and $z(x'', y'')$ are jointly gaussian with variance σ^2 and correlation coefficient ρ . The remaining terms of U_{pq} are developed similarly; these are functions of $\exp(-q_z^2 \sigma^2 (1 - \rho))$ and derivatives of ρ .

So that an analytical form can be obtained, the term $\exp(-q_z^2 \sigma^2(1-\rho))$ is expressed as series in ρ such that the first intensity term is

$$I \approx |a_0|^2 A_0 \exp(-q_z^2 \sigma^2) \sum_{n=0}^{\infty} (q_z^2 \sigma^2)^n / n! \times \iint_{-2L-2L}^{2L-2L} \rho^n \exp(jq_x u + jq_y v) du dv \quad (2.8)$$

where $A_0 = (2L)^2$ is the illuminated area (See Ulaby et al., [1982] for development of other terms). After a functional form is assumed for ρ , σ_{pq}^0 is determined as $\sigma_{pq}^0 = 4\pi R^2 \langle |\vec{E}_{pq}^s|^2 \rangle / A_0 |E_0|^2$. (2.9)

2.2.1.2 Small Perturbation method

This theory begins with the wave equation (Page 949 of [Ulaby et al., 1982]), i.e.,

$$\nabla^2 \vec{E} + k^2 \vec{E} = 0. \quad (2.10)$$

Using rectangular coordinates, each component is expressed as a function of wavenumbers. For example,

$$E_{fx} = (1/2\pi) \iint E_x \exp(-jk_x x - jk_y y) dx dy \quad (2.11)$$

(E_x can be retrieved from E_{fx} via an inverse Fourier Transform) Using the wave equation E_{fx} can be expressed as

$$(-k_x^2 - k_y^2 + d^2/dz^2) E_{fx} + k^2 E_{fx} = 0, \quad (2.12)$$

which has a solution of the form

$$A \exp(-jk_z z) + A' \exp(-jk_z z).$$

The total fields are assumed to be of the form:

$$\begin{aligned}
E_x &= (1/2\pi) \iint U_x \exp(jk_x x + jk_y y - jk_z z) dk_x dk_y \\
E_y &= (1/2\pi) \iint U_y \exp(jk_x x + jk_y y - jk_z z) dk_x dk_y \\
&\quad + \exp(-jk_x \sin \theta) (\exp(jk_z \cos \theta) + R \exp(-jk_z \cos \theta)) \\
E_z &= (1/2\pi) \iint U_z \exp(jk_x x + jk_y y - jk_z z) dk_x dk_y \quad (2.13)
\end{aligned}$$

where U_x, U_y, U_z represent unknown amplitude with respect to k_x and k_y and the additional term in E_y accounts for the source. The fields in medium 2 are similarly expressed, but with unknown amplitudes D_x, D_y , and D_z (Notice that propagation is in the x, z plane such that the incident wave is horizontally polarized).

From the boundary conditions, $\vec{n} \times \Delta \vec{E} = 0$ and $\vec{n} \times \Delta \vec{H} = 0$, and the divergence relations, $\nabla \cdot \vec{E} = 0$, six equations are obtained. $\Delta E_x, \Delta E_y$, and ΔE_z can be determined by expressing U_x, U_y, U_z, D_x, D_y , and D_z in terms of a perturbation series and expanding $\exp(-jk_z z)$, since $k_z z$ is small; for example,

$$\begin{aligned}
E_x &= (1/2\pi) \iint (U_{x1} + U_{x2} + \dots) [1 - jk_z z - \dots] \exp(jk_x x + jk_y y) dk_x dk_y \\
E_z &= (1/2\pi) \iint (D_{z1} + D_{z2} + \dots) [1 - jk_z z - \dots] \exp(jk_x x + jk_y y) dk_x dk_y
\end{aligned}$$

so that

$$\Delta E_x = (1/2\pi) \iint (U_{x1} - D_{x1}) \exp(jk_x x + jk_y y) dk_x dk_y = 0 \quad (2.14)$$

(to first-order).

First-order terms for ΔE_y and ΔE_z are obtained

similarly. $\Delta H_x, \Delta H_y$, and ΔH_z are obtained from derivatives of $\Delta E_x, \Delta E_y$, and ΔE_z . After solving the system of six equations and six unknowns the first-order scattered field can be expressed in terms of D_x, D_y, D_z, U_x, U_y , and U_z . An ensemble average is then taken. The result is of the form

$$\langle E_{pq} E_{pq}^* \rangle = |2k \sigma_1 \cos \theta \cos \theta_s \alpha_{pq}|^2 \iint W(k_x + k \sin \theta, k_y) dk_x dk_y \quad (2.15)$$

where $W(k_x, k_y) = (1/2\pi) \iint \rho(u, v) \exp(-jk_x u - jk_y v) du dv$

and where $\rho(u, v)$ is the correlation function of the

The resulting

$$\sigma_{pq} = 8 |k^2 \sigma_1 \cos \theta \cos \theta_s \alpha_{pq}|^2 W(k_x + k \sin \theta, k_y). \quad (2.16)$$

(See page 961 of [Ulaby et al., 1982])

2.2.1.3 Validity conditions

The Kirchhoff model (scalar approximation) is valid for $kl > 6$, $l^2 > 2.76 \sigma \lambda$, and $[-\sigma^2 \rho''(0)] 0.5 < 0.25$ [Ulaby et al., 1982],

where σ = rms height

l = correlation length

ρ = correlation function

λ = electromagnetic wavelength

k = wave number

The small perturbation model is valid for $k\sigma < 0.3$, and $(\sqrt{2})\sigma/l < 0.3$ [Ulaby et al., 1982].

2.2.2 Volume scattering theories

One of the most commonly used volume scattering theories is the radiative-transfer theory. It consists of a differential equation that is based on propagation of intensity and is not suited for conditions where fields are correlated.

More recent emphasis has been placed on analytical wave theories. These can generally be divided into two categories: (1) scattering from fluctuating media, and (2) scattering from layers containing discrete scatterers.

Fluctuating-medium theories include the Born Approximation and the Renormalization method. The former is applicable to volumes containing small permittivity fluctuations; i.e., $|\epsilon_f(\vec{r})/\epsilon_a| \ll 1$ where $\epsilon(\vec{r}) = \epsilon_a + \epsilon_f(\vec{r})$ (Page 1067 of [Ulaby et al., 1986]). If the electric field outside the medium is \vec{E} and that inside the medium is \vec{E}_1 , then $\nabla \times \nabla \times \vec{E} - k^2 \vec{E} = 0$ outside the medium and $\nabla \times \nabla \times \vec{E}_1 - k_a^2 \vec{E}_1 = k_a^2 \epsilon_f \vec{E}_1$ inside the medium.

The scattered field can be determined by iterative solution of

$$\vec{E} = \vec{E}^{(0)} + \int \vec{G}_{01}(\vec{r}, \vec{r}_1) \epsilon_f(\vec{r}_1) \cdot \vec{E}_1(\vec{r}_1) d\vec{r}_1$$

and

$$\vec{E}_1 = \vec{E}_1^{(0)} + \int \vec{G}_{11}(\vec{r}, \vec{r}_1) \epsilon_f(\vec{r}_1) \cdot \vec{E}_1(\vec{r}_1) d\vec{r}_1 \quad (2.17)$$

(See page 320 of [Tsang et al., 1985])

where $\vec{G}_{01}(\vec{r}, \vec{r}_1)$ and $\vec{G}_{11}(\vec{r}, \vec{r}_1)$ are layered-media dyadic Green's functions in the absence of permittivity fluctuations [Tsang et al., 1985]. The first-order Born solution (Born Approximation) is

$$\vec{E}_s^{(1)}(\vec{r}) = \int \vec{G}_{01}(\vec{r}, \vec{r}_1) \epsilon_f(\vec{r}_1) \cdot \vec{E}_1^{(0)}(\vec{r}_1) d\vec{r}_1 \quad (2.18)$$

From this the ensemble average of $\vec{E}_s^{(1)}(\vec{r}) \cdot \vec{E}_s^{(1)*}(\vec{r})$ is obtained as a function of the correlation of ϵ_f . After a functional form is assumed for the correlation function, the scattered intensity is determined and σ^o is obtained.

The Born Approximation does not include loss due to scattering but only that due to absorption. When scattering loss must be considered the Renormalization method is used. This is similar to the Born Approximation with the exception that the attenuation due to scattering loss is included in the wave equation; i.e., an effective propagation constant is determined. The equation is of the form:

$$\nabla \times \nabla \times \vec{E}_1 = k^2 \vec{E}_1 = - \int C(\vec{r}, \vec{r}_1) \vec{G}_{11}(\vec{r}, \vec{r}_1) \cdot \vec{E}_1(\vec{r}_1) d\vec{r}_1 \quad (2.19)$$

(See page 1073 of [Ulaby et al., 1986])

where $C(\vec{r}, \vec{r}_1)$ is the correlation of the dielectric constant (the integral term is Dyson's equation).

Effective medium approximations are also commonly used for layers of discrete scatterers. A mixing formula is used to obtain the effective dielectric

constant. To account for scattering loss the radiation power of the particles is considered. Scattering loss is dependent on the pair-distribution function, just as it was dependent on correlation length for the Renormalization method. With these considerations an effective propagation constant for spherical particles can be found to be [Tsang et al., 1985]:

$$K^2 = k^2(1+2fy)/(1-fy) + j2fk^5 a^3 |y/(1-fy)|^2 \times (1-8f+24fH_0) \quad (2.20)$$

where $f = n_0 v_0$ is the fractional volume occupied by the scatterers

$y = (\epsilon_s - \epsilon) / (\epsilon_s + 2\epsilon)$, where ϵ_s = permittivity of the scatterers
 ϵ = permittivity of the background

a = particle radius

H_0 includes pair distribution effects

After the development is complete σ^o of the form

$$\sigma_{VV}^o = \sigma_{HH}^o = |(K - k_{iz})k_{iz} / n_0|^2 (n_0 / 2\pi \text{Im}(K_z)) \times \{1 + n_0 \int_{-\infty}^{\infty} [g(r) - 1] dr\} \quad (2.21)$$

(See page 438 of [Tsang et al., 1985])

is obtained where

$$k_{iz} = k \cos \theta_i$$

$$K_z = \text{sqrt}(K^2 - k^2 \sin^2 \theta_i)$$

$g(r)$ =two-particle distribution function

More recently theories have been developed to account for multiple scattering. These are not considered in this paper.

3.0 Measurements conducted: microwave backscatter and ice characterization

We performed backscatter measurements of controlled and well-characterized ice surfaces at the Cold Regions Research and Engineering Laboratory (CRREL), in Hanover, New Hampshire. CRREL is well suited for such experiments both because of its excellent facilities (esp. for characterizing ice) and because of the glaciological expertise available on-site. In addition the local climate usually favors ice growth.

Simulated sea ice was grown at CRREL in a 12.2 x 5.2m, 1.5-m deep, outdoor pond that can be covered by a large moveable tent during periods of inclement weather. Straddling the pond is a gantry on which the radar antennas were mounted, permitting collection of data over the entire surface at various incidence angles. Adjacent to the pond is a tent for operating the radars. The setup for the 1987 experiment is shown in Fig. 3.1. Figures 3.2 and 3.3 are photographs of setups used during the 1988 and 1989 experiments, respectively.

Table 3.1 provides a list of backscatter measurements conducted during the winters of 1986-1987, 1987-1988, and 1988-1989. During all three campaigns

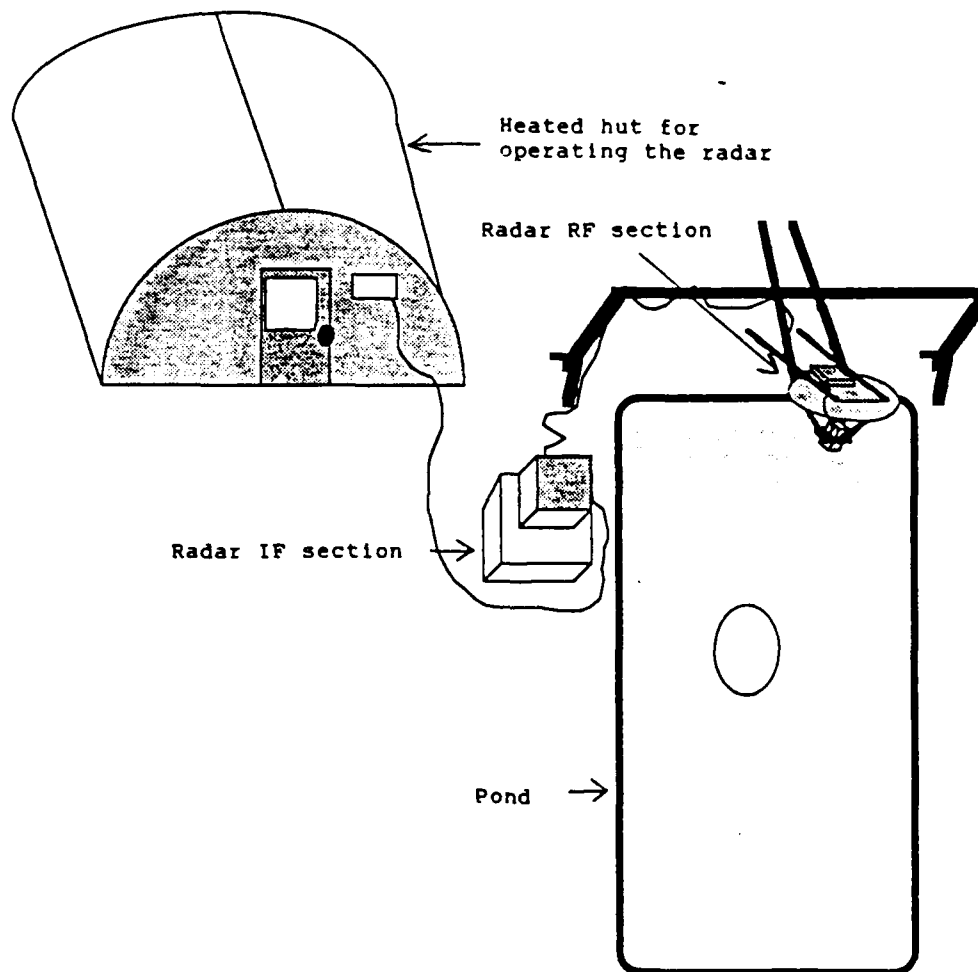


Figure 3.1: Setup for CRREL '87 experiment.



Figure 3.2: Setup for CRREL '88 experiment. Tent (T) has been rolled off to expose pond (P) for measurements from gantry (G).

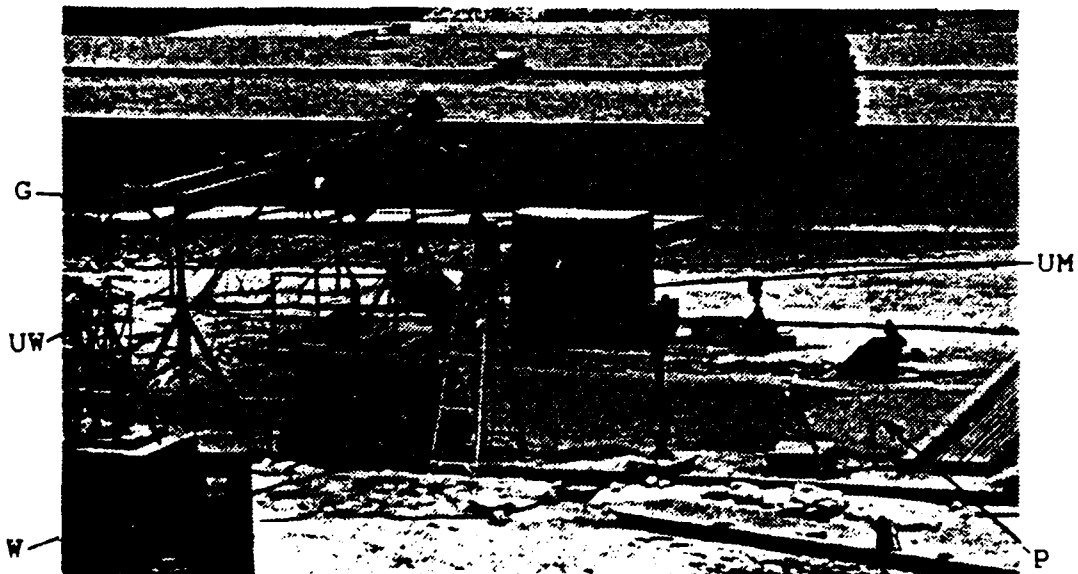


Figure 3.3: Setup for CRREL '89 experiment. University of Kansas and Environmental Research Institute of Michigan radars mounted on the gantry (G), University of Washington (UW) radiometers, and University of Massachusetts (UM) radar and radiometer during measurements on pond (P). Weather station (W) is in foreground.

<u>Year</u>	<u>Date</u>	<u>Scene Observed</u>	<u>Comments</u>
1987	Jan. 17	Smooth saline ice	X-band angle scan
	Jan. 18	Snow covered smooth saline ice	"
	Jan. 21	Roughened saline ice	"
1988	Jan. 14, 15	Smooth saline ice	C-band angle scan
	Jan. 15	Rough saline ice	"
	Feb. 26	Desalinated ice	C-band vs temperature
	Feb. 27, 28	Desalinated ice	C-band angle scan
1989	Feb. 4,5	Desalinated ice blocks	C-,Ku-band angle scan
	Feb. 3	Bare and snow covered saline ice	C-band angle scan

Table 3.1 Scenes observed during three years of experiments at CRREL

smooth saline ice surfaces (i.e., surfaces with rms height < 0.05 cm) were observed; thickness effects were stressed during 1988 and 1989. The effect of a several-cm snow cover was studied during the 1987 and 1989 campaigns. The effects of roughness on backscatter from saline ice were examined in 1987 and 1988. Backscatter from desalinated ice was the

emphasis of the 1988 and 1989 experiments.

The backscatter measurements of 1987 were conducted at X-band. In 1988 we concentrated on C-band although we made some X-band measurements. In 1989 very thin saline ice was studied with C- and Ku- band, thin saline ice and snow cover effects were examined with C-band, and C- and Ku- band were used to study backscatter from desalinated ice.

The ice characterization measurements done varied from 1987 to 1989 because we tried to provide a more detailed and more accurate quantitative description of the ice for each succeeding experiment. Discussions of techniques and measurements done for each experiment are given in the following sections. For all of the experiments salinity profiles and ice-structure photographs were supplied by CRREL. Salinity profiles were determined with a Beckmann Salubridge by measuring the conductance of the meltwater of 1-2 cm thick sections cut from an ice core. Using water temperature as an input, conversion of conductance to salinity was performed automatically by the bridge. Ice-structure photographs were obtained of 0.5-1 mm thick ice sections, which were prepared using a Leitz Wetzlar sledge microtome. The ice sections were photographed through crossed polarized filters so as to enhance the ice crystalline structure.

3.1 CRREL 1987

3.1.1 Measurement regime

Experiments began on January 17, 1987, with backscatter measurements on saline ice consisting of 6 cm of granular slush ice overlaying 6 cm of congelation ice. One day later, after 6.5 cm of snow had fallen, further measurements were made. Three days later, the third set of measurements involved slightly roughened ice. Its surface differed from the one observed earlier because of small-scale roughness introduced by the process of removing all snow and slush with a rubber bladed shovel.

3.1.2 Experimental procedure

For each of the scenes, backscatter was measured at incidence angles of 0, 10, 20, 30, 40, and 50° for vertical and horizontal polarizations. The height of the gantry was adjusted to maintain a slant range close to 3.5 m for all incidence angles. Ten statistically uncorrelated observations were made for each angle by moving the gantry over the ice surface. The system response was determined at the beginning and end of each of the three measurement sequences. Echoes from a 12-inch Luneberg-lens reflector provided an absolute calibration.

3.1.3 Measured surface physical characteristics

The salinity of the pond water was maintained at

240/00 throughout the experiment. Air temperature was continuously monitored at an adjacent weather station. We estimated surface height and measured ice thickness and salinity daily. Ice thickness, salinity profiles and structural information were also obtained on blocks of ice periodically removed from the pond.

The ice sheet was grown by allowing naturally precipitating snow to accumulate on the surface of the pond. This created a layer of slush which ultimately froze to form saline slush ice. Continued freezing of the salty water directly beneath the slush ice led to the formation of columnar-textured, congelation saline ice. The actual progress of this growth is illustrated in the series of thin-section photographs shown in Fig. 3.4. On January 20, 1987, the ice sheet reached a thickness of 12 cm. It had about equal parts of slush ice and congelation ice. The slush ice was composed of two layers; coarse-grained ice with platy grains up to several millimeters in diameter overlaid a fine-grained component with grains less than 1 mm in diameter. The photographs show that some modification of the texture of the slush ice occurred as it aged. The salinity characteristics (Fig. 3.5) and crystalline structure of this ice sheet closely resemble those obtained at the earliest stages of growth of Arctic sea ice in a slushed-over lead undergoing quiet freezing [Gow, 1988].

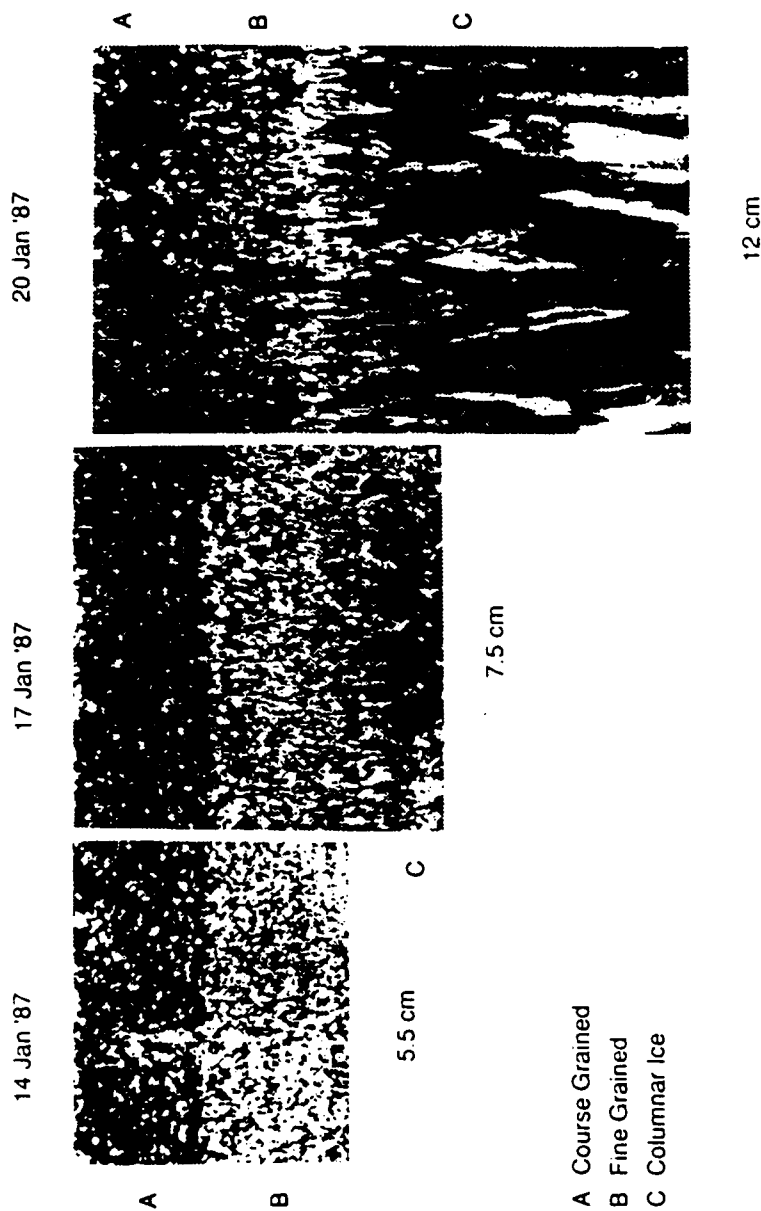


Figure 3.4: Vertical growth history of saline ice sheet grown during CRREL'87 as seen in thin section photographed between crossed polarizers (courtesy of CRREL).

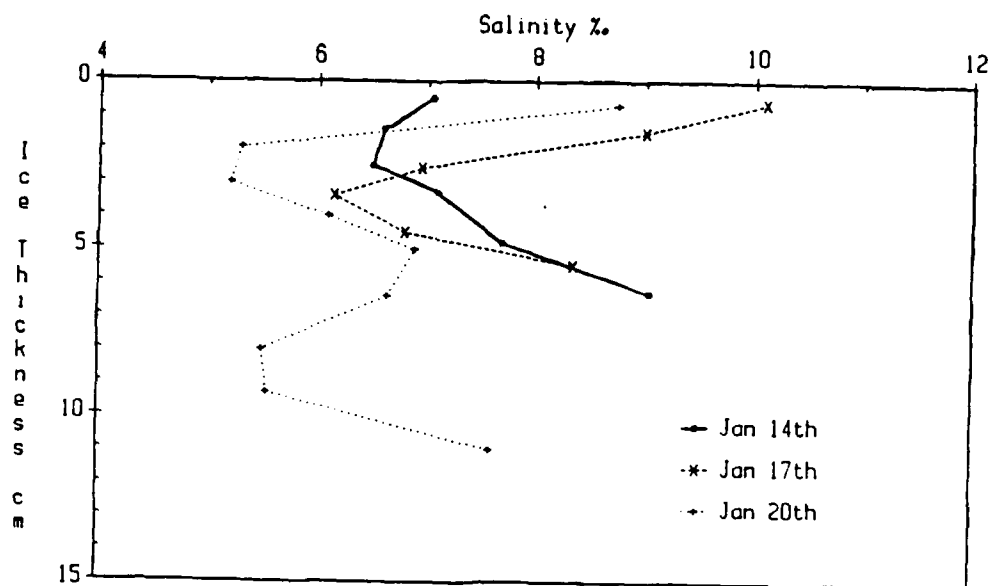


Figure 3.5: Salinity profiles of saline ice sheet grown during CRREL '87 experiment.

Temperature profiles were not determined. Using the air temperature and salinity profiles, we estimated the dielectric constants to be $3.4-j0.19$, $3.55-j0.25$, and $3.35-j0.17$ for January 17, 18, and 21 respectively. Surface roughness was estimated by observation; we estimated the rms height to be 0.1 cm for the two bare ice sheets. A texture was noticeable on the January 21 surface.

3.2 CRREL 1988

3.2.1 Measurement regime

Experiments began on January 11, 1988, with C- and X-band backscatter measurements on open water. They continued as the ice formed to a thickness of about 1 cm. Measurements were repeated for ice thicknesses of 3, 7, and 10 cm. Then 1 x 2 cm ice prisms were dumped on the sheet to simulate rubble field roughness in preparation for further measurements.

From January 16 to February 25 the ice was allowed to desalinate; during this period rain and meltwater contributed to the flushing of salt from the ice sheets. Several measurements were then conducted to study the effects of temperature. These were followed by incidence-angle measurements.

3.2.2 Experimental procedure

For each of the scenes, backscatter was measured at 10, 20, 30, 40, 50, and 60° for VV, HH, VH, and HV polarizations. The gantry height was maintained at approximately 3.3 m, for convenience. For each incidence angle, several statistically uncorrelated observations were made by moving the gantry over the ice surface - the number of uncorrelated samples varied depending on the scene we were observing. We measured the system response after every 2 or 3 samples. Backscatter from a 8" Luneberg lens or an active radar

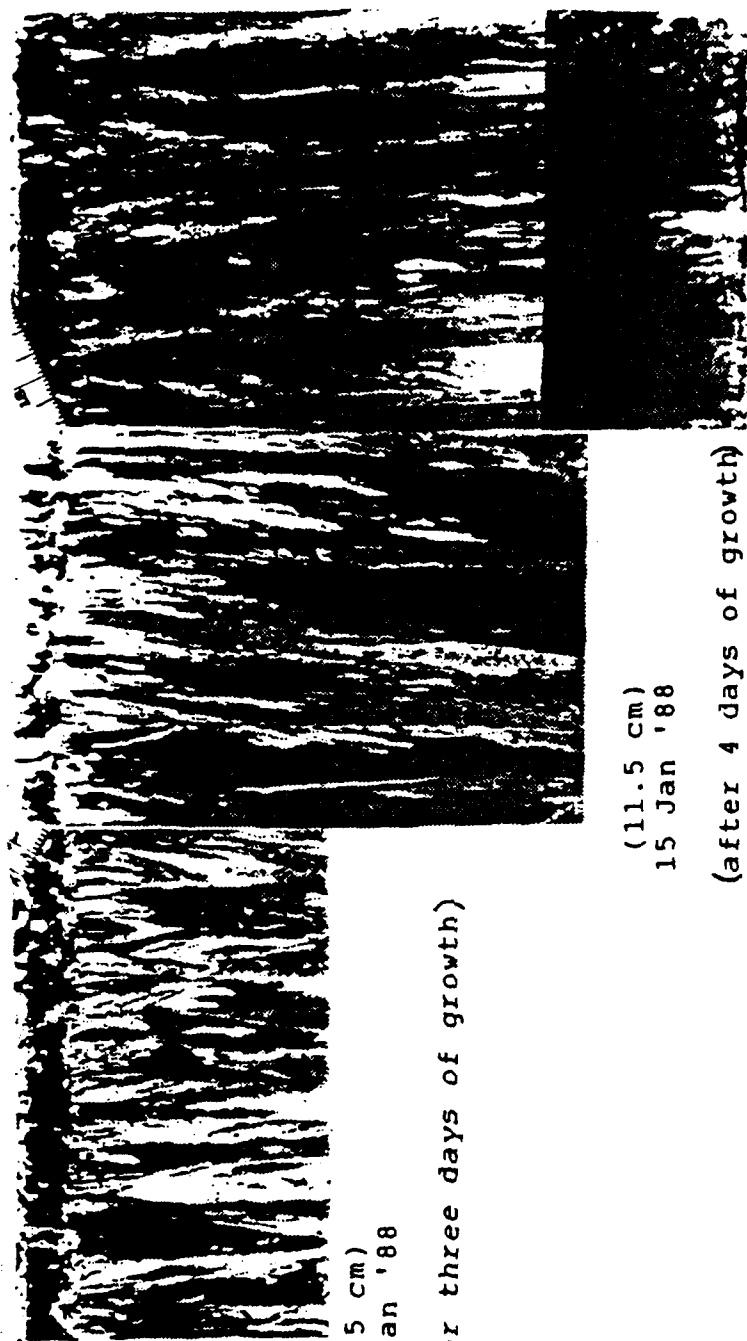
calibrator was measured every 2 or 3 days.

3.2.3 Measured surface physical characteristics

The salinity of the pond water was maintained at 240/00 throughout the experiment, as during 1987. Air temperature was continuously monitored at a nearby weather station and readings from a thermistor string provided ice temperature profiles. We measured surface-roughness parameters of the desalinated ice and obtained saline-ice roughness parameters from other groups participating in the experiments. We also measured ice thickness and obtained ice salinity and structural information from CRREL.

Ice formation began as a result of spray seeding of the surface water. The internal structure of the ice sheet after about 6 days growth is shown in Fig. 3.6; it is typical of that of first-year ice growing under calm conditions and composed principally of columnar crystals. After two days of rather intense desalination, i.e., flushing by meltwater and rain, the crystal structure changed dramatically and more bubbles appeared (Fig. 3.7a). Further growth and desalination over a period of three weeks led to further changes (Fig. 3.7b). Two and a half weeks later the ice became very porous (Fig. 3.8).

Platelet structures of ice crystals as observed in horizontal thin-sections are shown in Figs. 3.9 and 3.10.



(6.5 cm)
14 Jan '88

(after three days of growth)

(11.5 cm)
15 Jan '88

(after 4 days of growth)

(14.5 cm)
17 Jan '88

(after 6 days of growth)

Figure 3.6: Growth history of saline ice sheet of CRREL'88 experiment as revealed in thin sections of ice structure photographed between crossed polarizers (courtesy of CRREL).

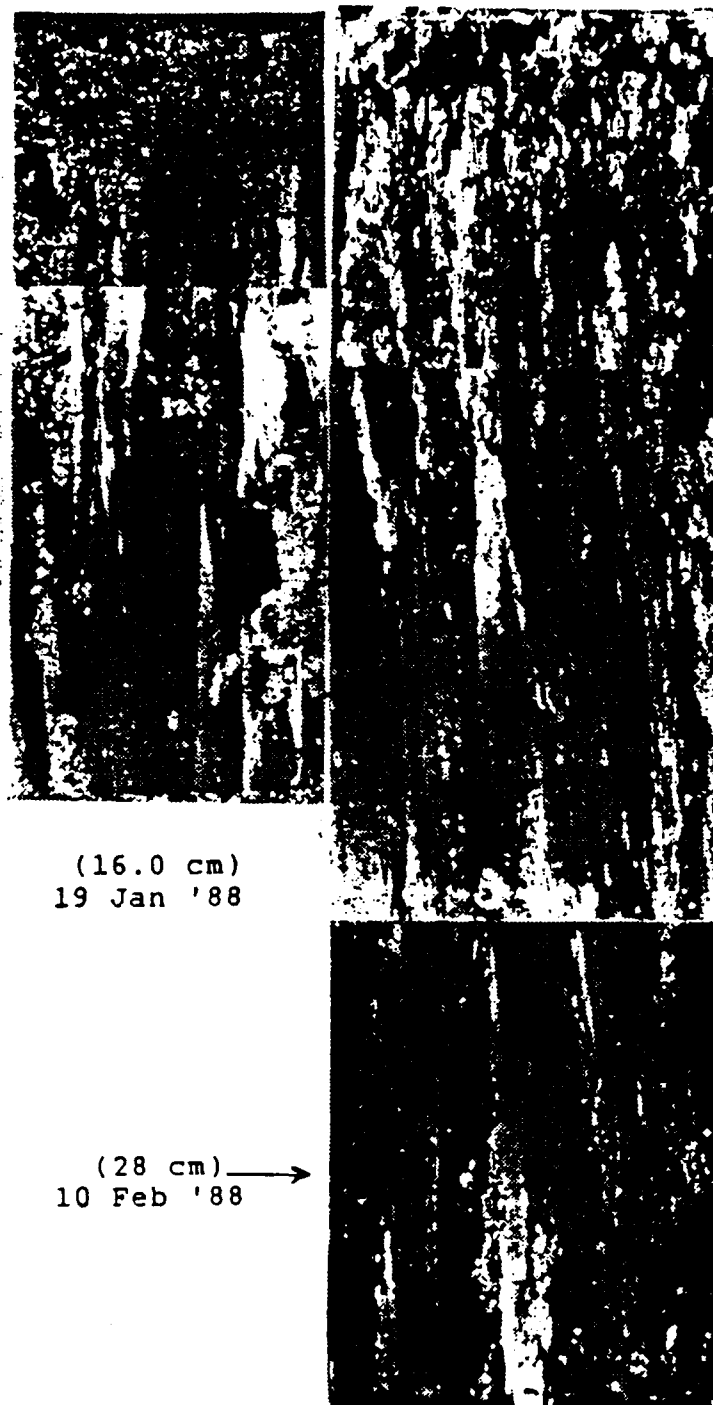


Figure 3.7: (a) saline ice sheet of Fig. 3.6 after 2 days of intense desalination (b) same sheet after 3 weeks of growth and desalination (courtesy of CRREL).



Figure 3.8: Porous nature of ice revealed in slice of saline ice sheet of Fig. 3.6 photographed in transmitted light after 5 and a half weeks of desalination and growth.

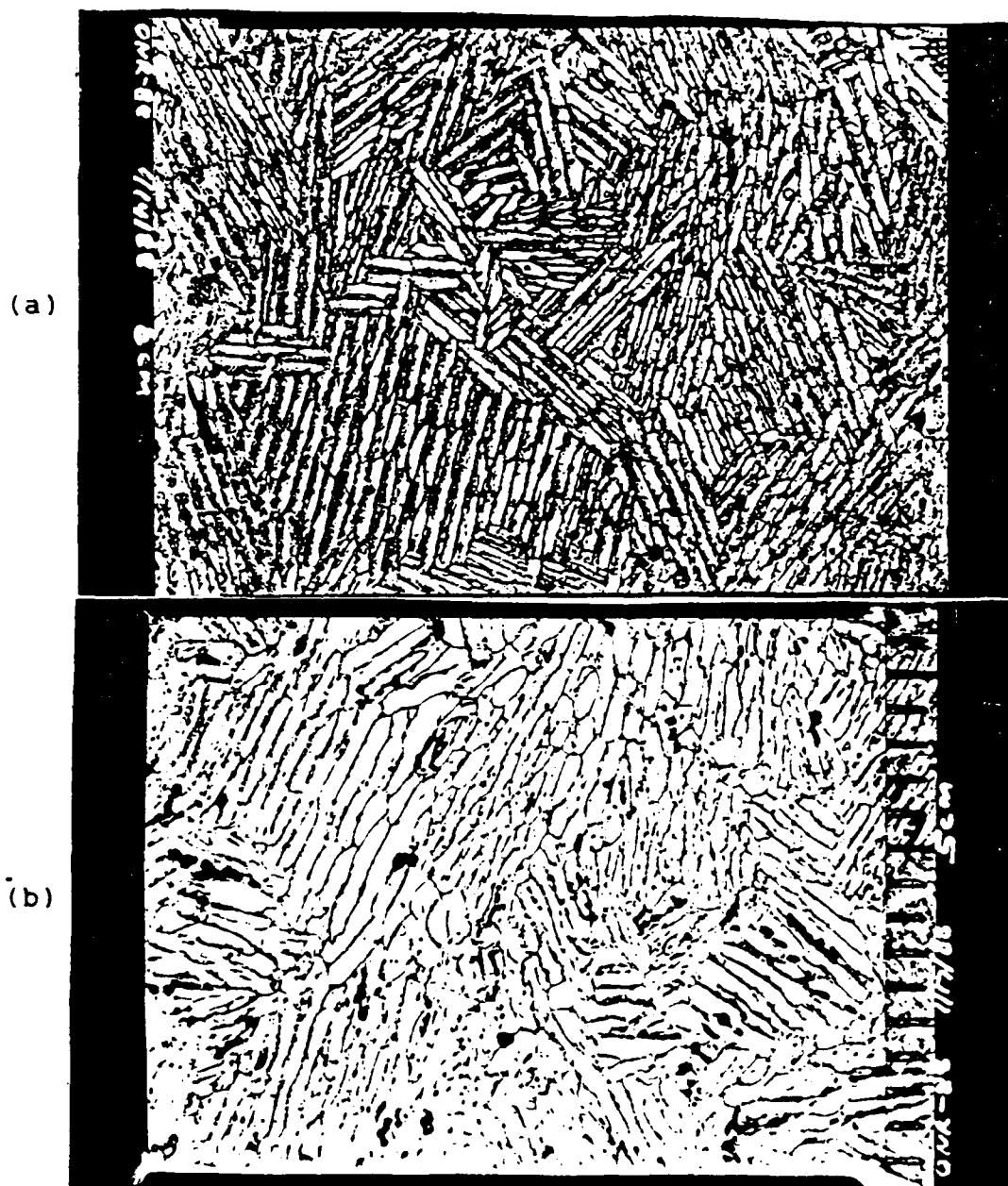
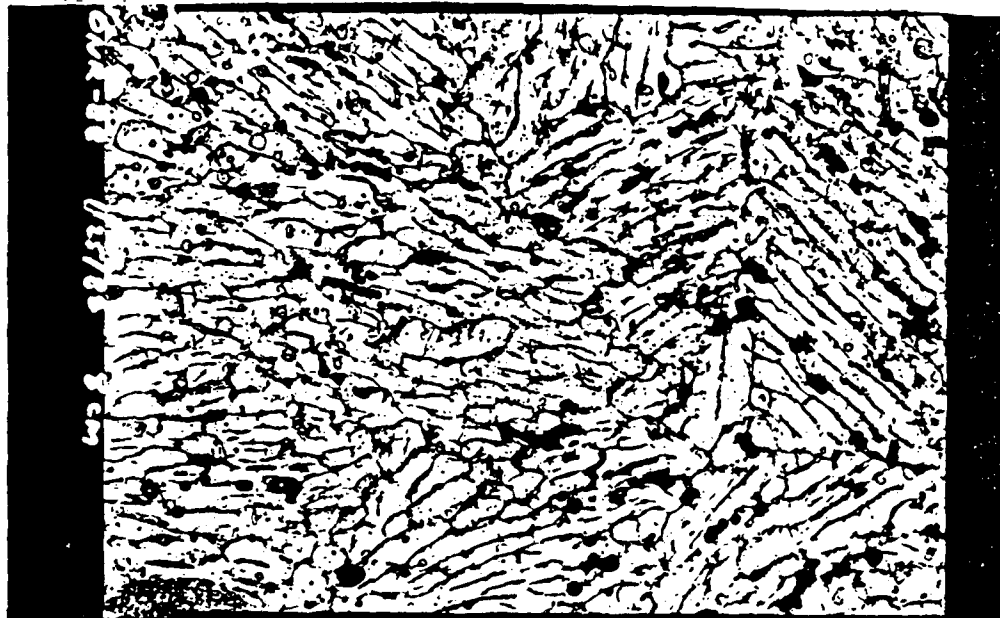


Figure 3.9: (a) platelet structure of crystals at depth of 6 cm in 6.5-cm thick ice sheet of Fig. 3.6 after 3 days of growth (b) platelet structure of crystals at depth of 5 cm in 14.5-cm thick ice sheet of Fig. 3.6 after 6 days of growth (courtesy of CRREL).

(a)



(b)



Figure 3.10: (a) thermally modified platelet structure in ice from depth of 8 cm in 19-cm thick ice sheet of Fig. 3.6 after 11 days of growth and desalination (b) thermally modified platelet structure in ice from depth of 8 cm in 23-cm thick ice sheet of Fig. 3.6 after 3 weeks of growth and desalination (courtesy of CRREL).

The platelet boundaries were progressively modified as desalination occurred. Second-generation desalination resulted in an increase in air bubbles. The desalination process is further illustrated in the salinity profiles of Fig. 3.11.

Figure 3.12 shows temperature profiles obtained during the experiments. Using the salinity and temperature profile data and the equations of Frankenstein and Garner [1967], dielectric profiles were calculated as shown in Figs. 3.13. Two-way absorption loss as-a-function-of-depth-into-the-ice for each ice sheet, obtained from the estimated dielectric constants, is shown in Fig. 3.14. Table 3.2 presents surface roughness and air bubble distribution data.

3.3 CRREL 1989

3.3.1 Measurement regime

Experiments began on January 9, 1989, with C- and X-band backscatter measurements on open water. Continuous measurements were conducted as the ice formed to a thickness of 2.5 cm. Measurements of this smooth ice sheet were repeated periodically throughout the remainder of the experiment.

The major focus of the CRREL '89 experiment was on microwave measurements of desalinated ice. On 29 December 1988 a 16-18 cm thick saline ice sheet was cut into 1 x 1 m blocks and harvested. These blocks were

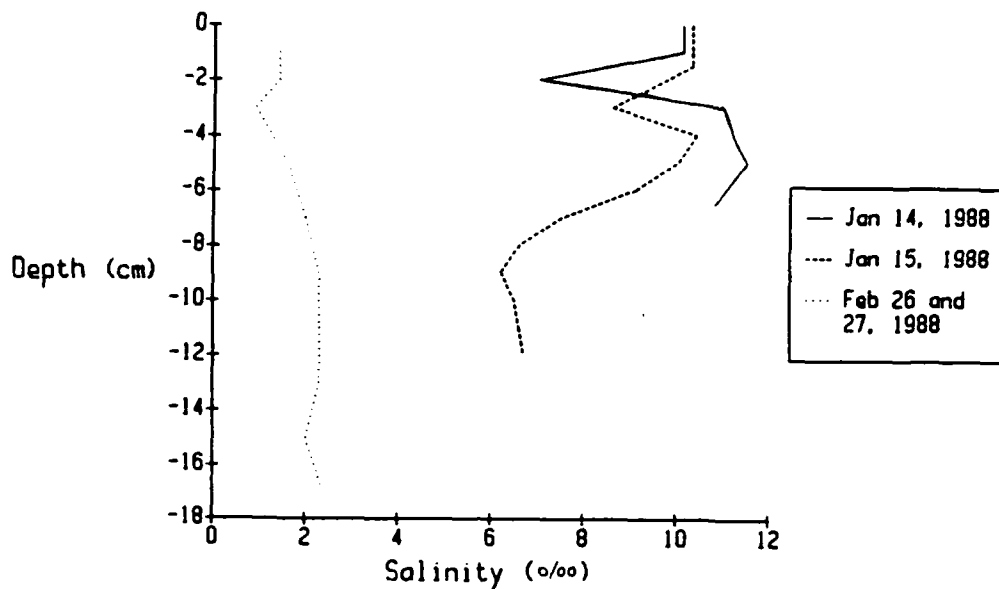


Figure 3.11: Salinity profile history of saline ice sheet of CRREL'88 experiment.

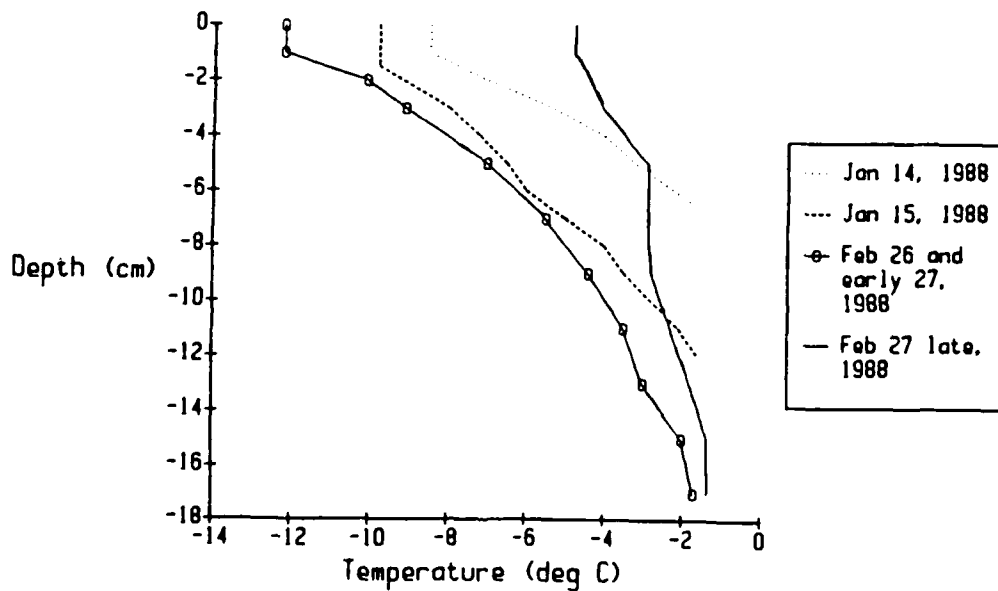
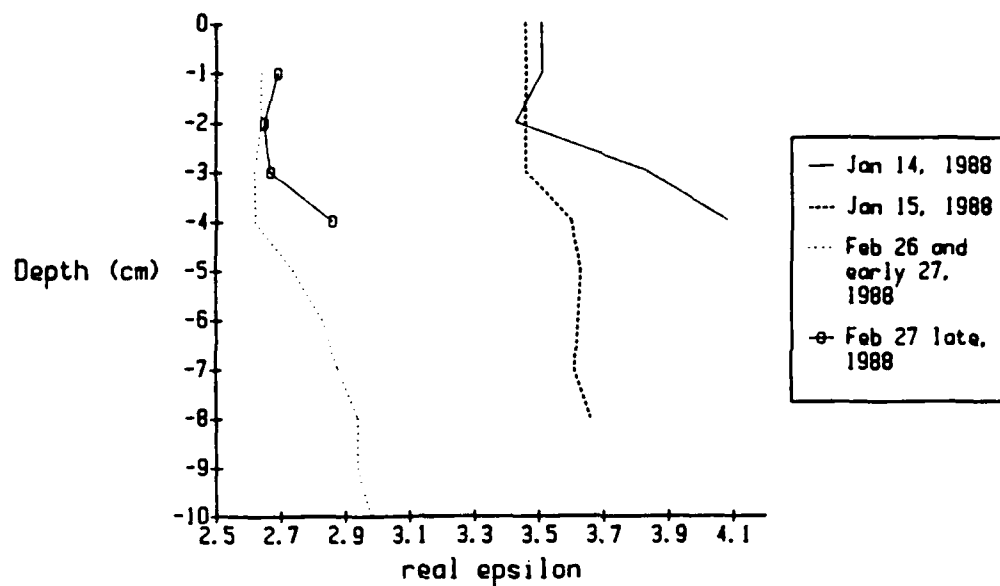
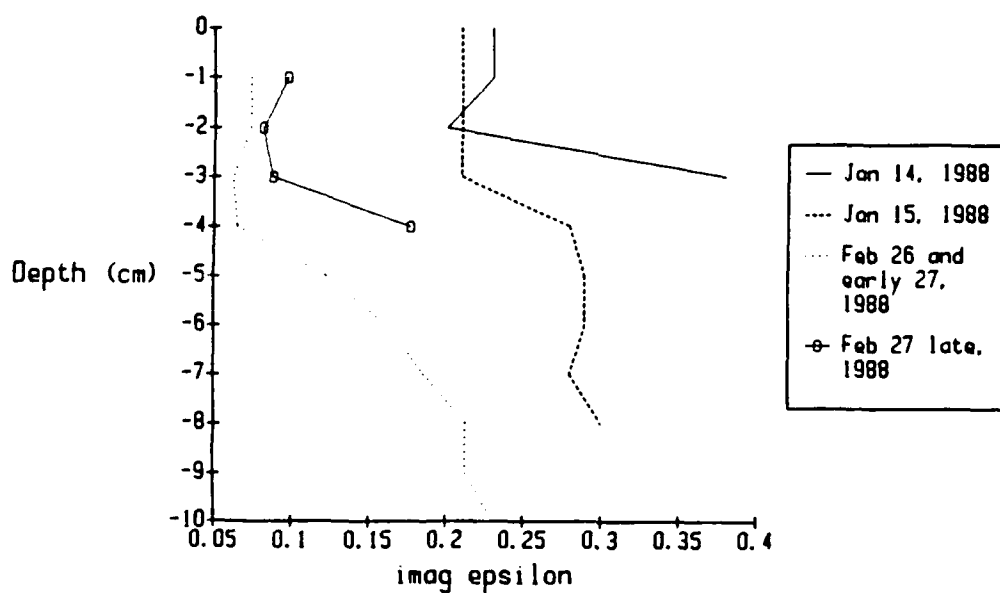


Figure 3.12: Temperature profiles of CRREL'88 ice sheet on dates measurements were taken.



(a)



(b)

Figure 3.13: Estimated dielectric constant profiles at C band on dates measurements were taken during the CRREL'88 experiment: (a) real component of epsilon (b) imaginary component of epsilon.

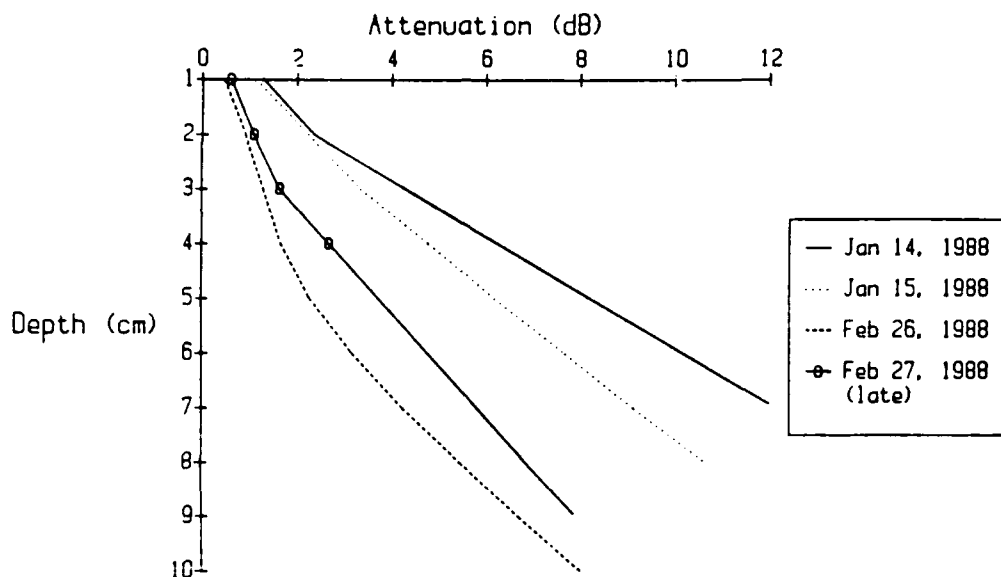


Figure 3.14: Two-way absorption loss at C band as a function of depth into the ice, computed from data of Fig. 3.13.

surface	rms height	s.d. of rms height	corr length	corr length +1 s.d.	-1 s.d.
Smooth saline ice (Jan. 14)	0.029	0.01	1.77	0.81	2.49
Roughened saline ice (Jan. 15)	0.45	0.14	0.98	0.56	1.96
Desalinated ice (Feb. 26,27,28)	0.18	0.07	2.5	1.88	4.52
volume	mean air bubble radius	air bubble corr length	density		
Desalinated ice (Feb. 26,27,28)	est. 67% ≈ 0.5 mm 32% 0.5-1 mm 1% 2 mm	unknown	unknown		

Table 3.2 Surface characteristics for CRREL '88 experiment (all dimension in cm unless otherwise indicated)

stored on pallets and allowed to desalinate. These blocks were then assembled, as shown in Fig. 3.15, to allow backscatter measurements. We performed measurements at C- and Ku- band for one and two layers of blocks.

3.3.2 Experimental procedure

For saline ice, backscatter was measured at 10, 20, 30, 40, and 50° for VV, HH, VH, and HV polarizations. For the desalinated ice block assemblage, measurements were made at incidence angles of 15, 25, and, for Ku-band, 35°. For saline ice, 5 statistically uncorrelated observations were made at each incidence angle. Only 3 statistically uncorrelated samples were possible for the desalinated ice because we performed measurements so as to avoid the effects of block edges. The system response was determined after every 2 or 3 samples and backscatter from a 8" Luneberg lens provided a calibration reference.

3.3.3 Measured surface physical characteristics

The salinity of the pond water was maintained at 24o/oo throughout the experiment, as in 1987 and 1988. Physical characteristics of the ice were measured in nearly the same manner as in 1988. In 1989, however, surface roughness was determined with a wire gauge

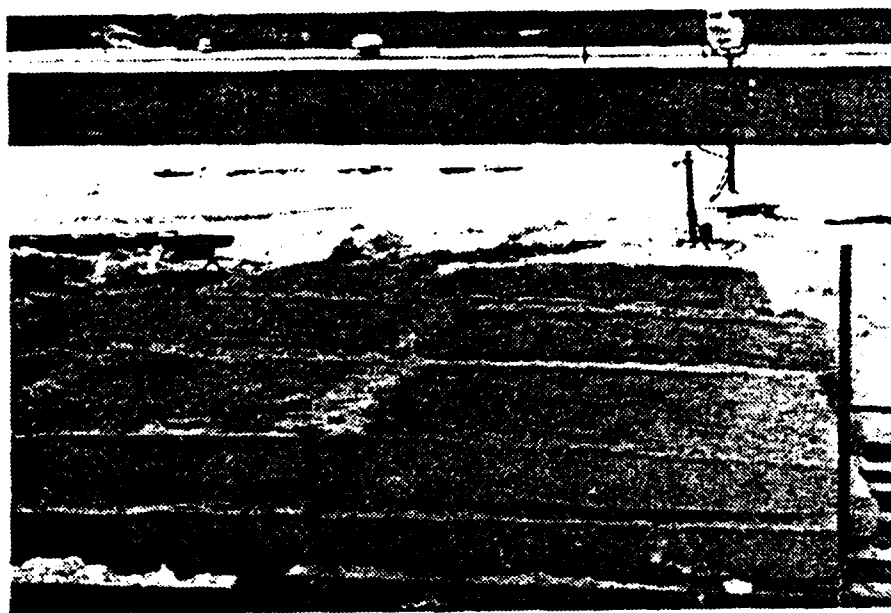


Figure 3.15: Desalinated ice blocks as studied during the CRREL'89 experiment.



Figure 3.16: Porous structure of ice as seen in horizontal thick section from top surface of a desalinated block shown in Fig. 3.15.

rather than from photographs, and we made a more thorough analysis of the air bubble structure of desalinated ice.

Figure 3.16 illustrates the porous structure of desalinated ice as observed in a horizontal section from near the surface of a block and Fig. 3.17 shows the air bubble size distribution at the top, middle and bottom of the block. Other structural parameters are listed in Table 3.3.

<u>surface</u>	<u>rms height</u>	<u>s.d. of rms height</u>	<u>corr length</u>	<u>corr +1 s.d.</u>	<u>corr -1 s.d.</u>
Bare smooth and snow covered saline ice (Feb 3)	0.024	0.012	1.2	1.1	1.46
Desalinated ice (Feb.4 , Feb. 5)	0.08	0.15	3.3	2.2	3.9

<u>volume</u>	<u>air bubble radius</u>	<u>dielectric constant</u>	<u>corr length</u>	<u>density</u>
Desalinated ice (Feb. 4, Feb. 5)	(see Fig. 3.17)	1.5 - 2.0 mm		0.844 (bulk)

<u>Snow</u>	<u>mean particle size</u>	<u>density</u>	<u>wetness</u>
Feb. 3 sheet	.1 x .2 cm	0.05 g/cm ³	<5%
surface rms height = 0.28 cm, corr length = 1.8 cm			

Table 3.3 Surface parameters for CRREL '39 experiment (all dimensions in cm unless otherwise indicated)

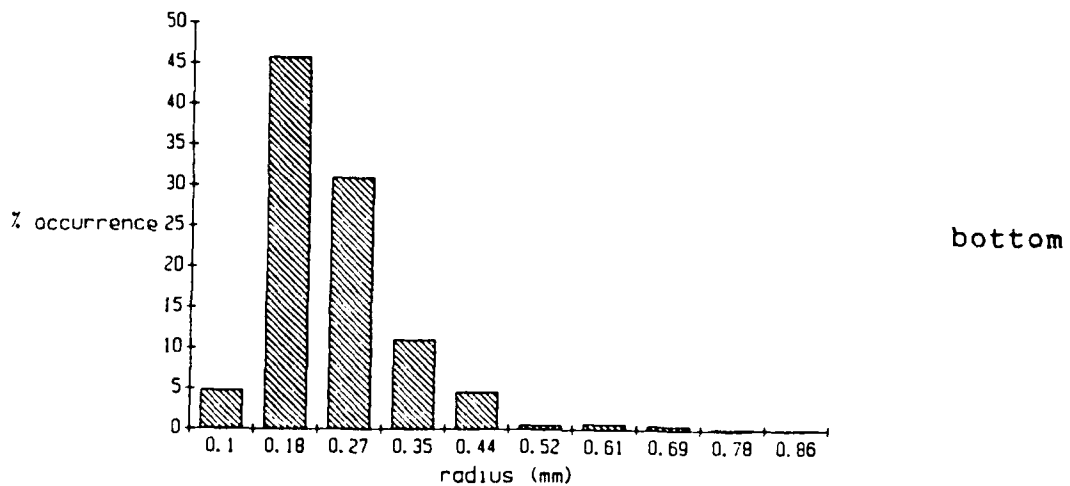
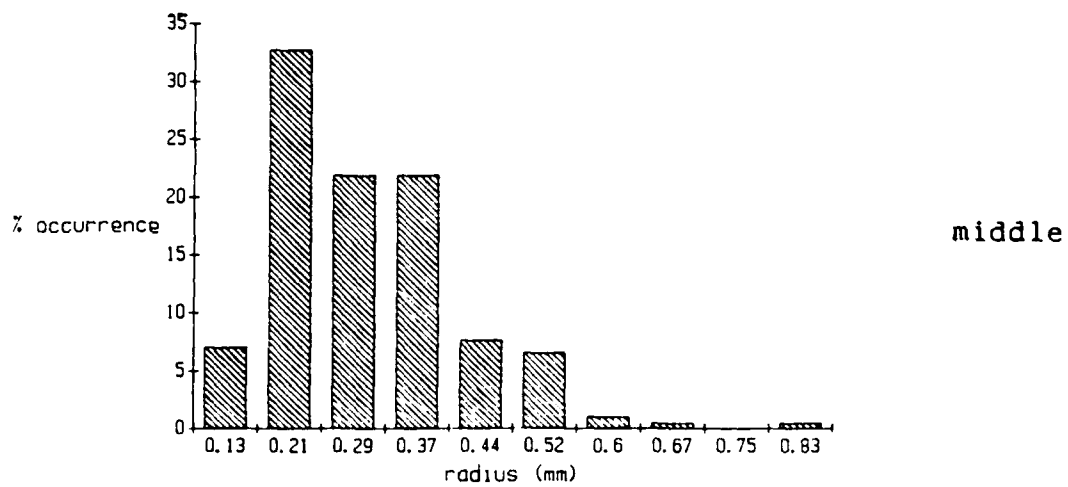
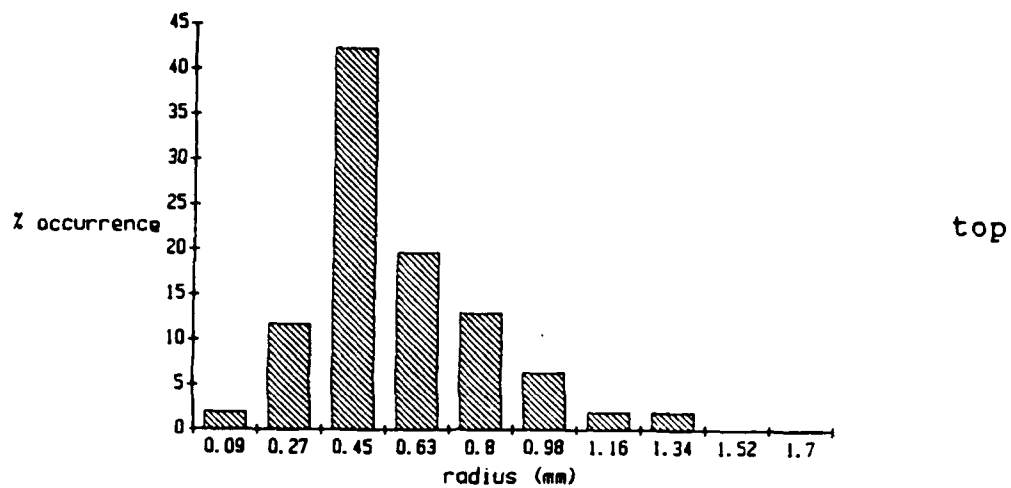


Figure 3.17: Air bubble size distribution in a block of desalinated ice shown in Fig. 3.15.

Figure 3.18 indicates the temperature profile of the saline ice sheet at the time of the backscatter measurements and Fig. 3.19 the ice sheet salinity profiles for the surfaces observed. We obtained the dielectric constant profiles in Fig. 3.20 using the empirical equations given by Garner and Frankenstein [1967]. Two-way absorption loss as-a-function-of-depth-into-the-ice for each ice sheet, obtained from the estimated dielectric constants, is shown in Fig. 3.21.

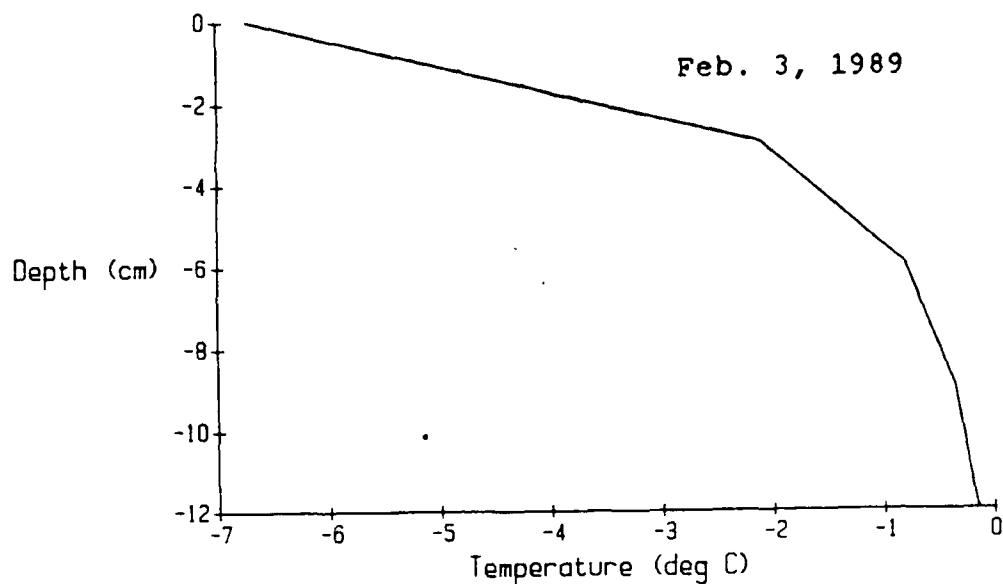


Figure 3.18: Temperature profile of saline ice sheet grown during the CRREL'89 experiment, on date measurements were taken.

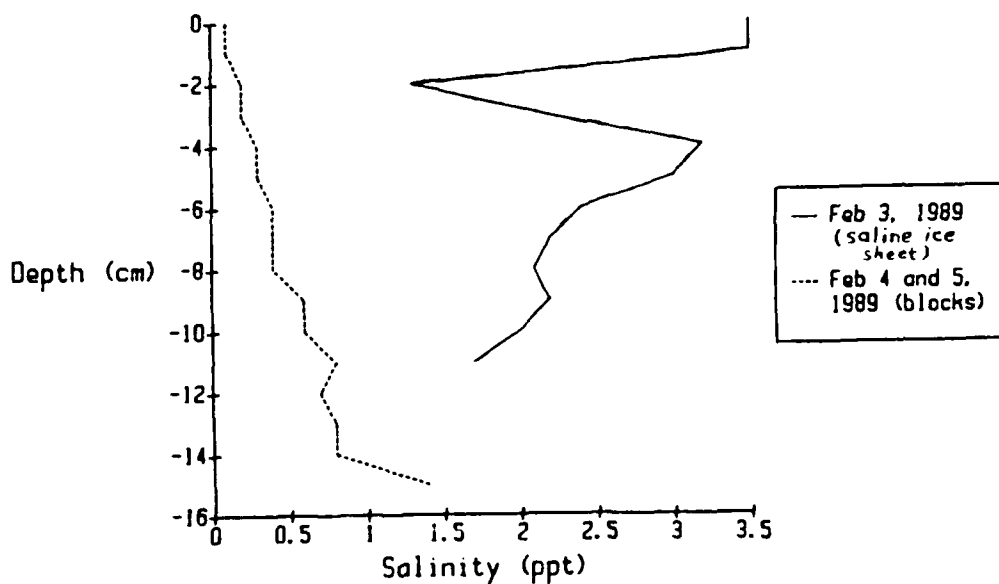
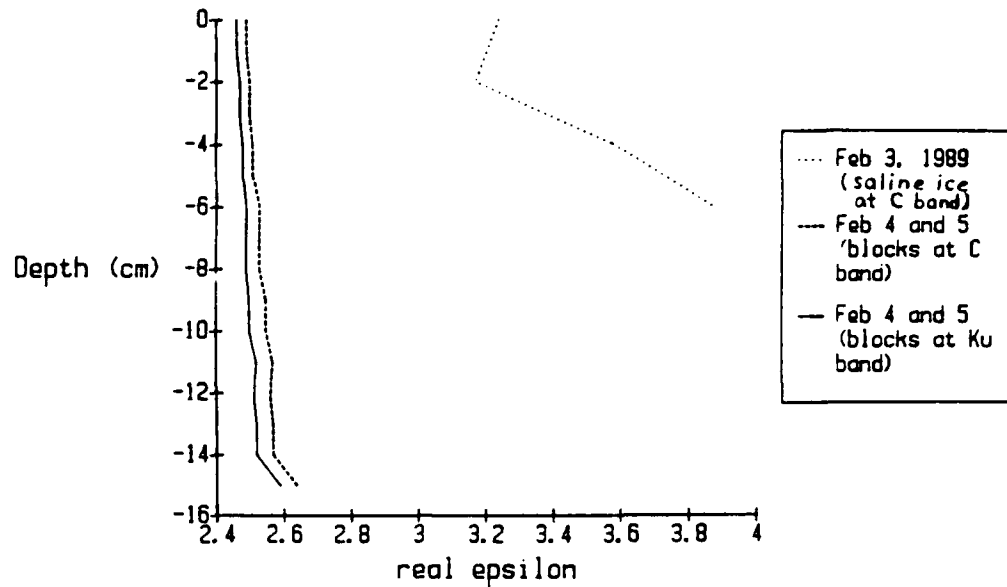
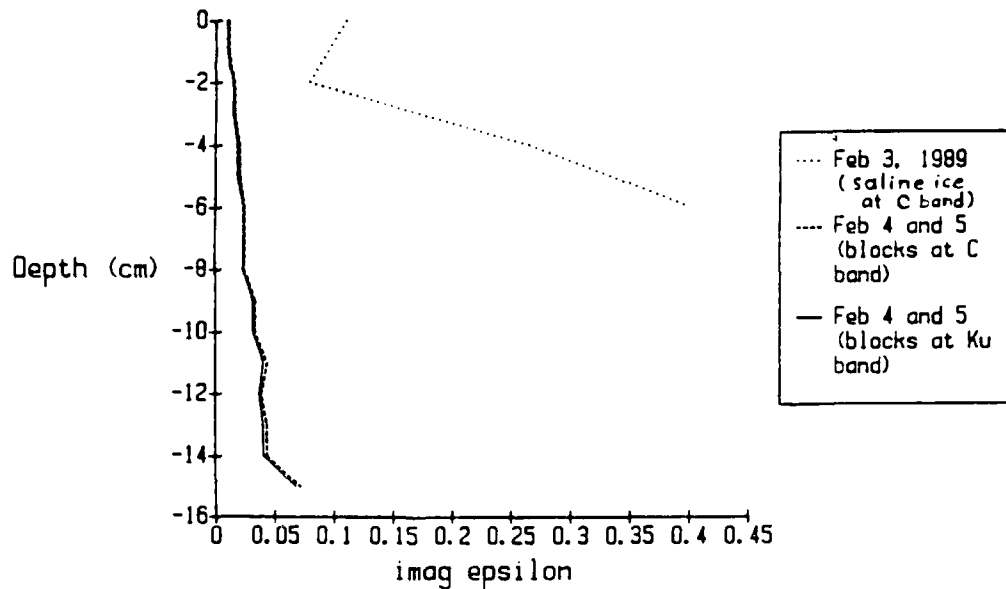


Figure 3.19: Salinity profiles of saline ice sheet and desalinated ice blocks on date measurements were taken during the CRREL'89 experiment.



(a)



(b)

Figure 3.20: Estimated dielectric constant profiles on dates measurements were taken during the CRREL'89 experiment: (a) real component of epsilon (b) imaginary component of epsilon.

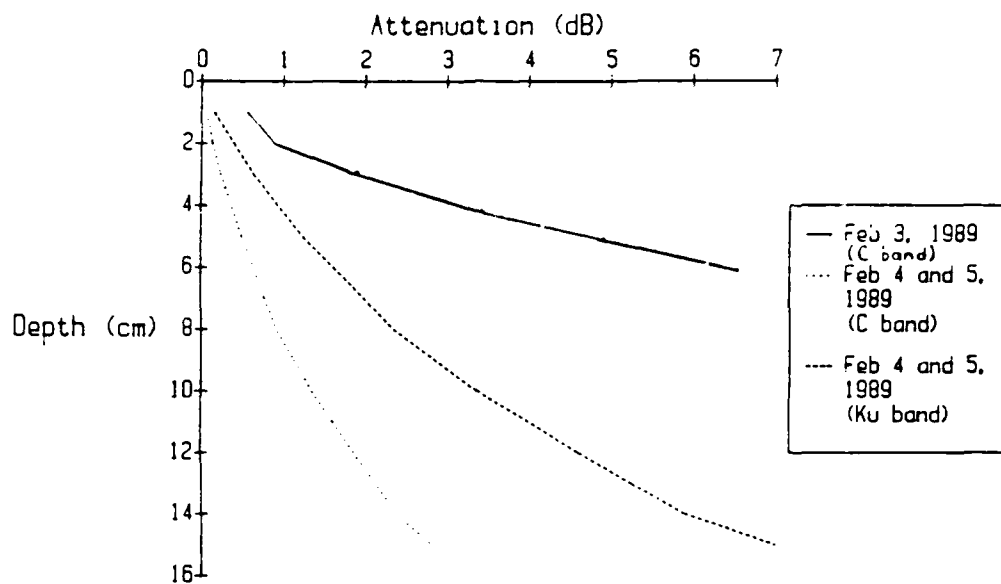


Figure 3.21: Two-way absorption loss as a function of depth into the ice, computed from data of Fig. 3.20.

4.0 The Radar Systems

Over the course of three years of experiments at CRREL three different radar systems were used. During the 1986-1987 experiment the X-band SOURCESCAT radar provided backscatter data; during the 1987-1988 experiment the first version of PAIR (Polarimetric Agile Instrumentation Radar) was used; and during the 1988-1989 campaign the second version of PAIR and a newly developed step frequency radar (STEFRAD) were employed.

4.1 Design considerations and operation

The constraints on the designs of our systems were imposed both by logistics and by our experiment objectives. The CRREL facility limited measurement ranges to a maximum of 4 to 5 meters. Our experiment objectives required fine resolution both in slant range and in azimuth. The 1987-1988 and 1988-1989 experiments further required copolar phase measurement capability.

4.1.1 The SOURCESCAT radar

A block diagram of the X-band SOURCESCAT radar is shown in Fig. 4.1. This radar is a simple single-antenna triangularly modulated FM-CW device ([Gogineni, 1984] and [Zoughi, 1984]). Fine resolution in slant range is obtained by modulating over an r.f. bandwidth of 2 GHz, giving an unweighted range resolution of

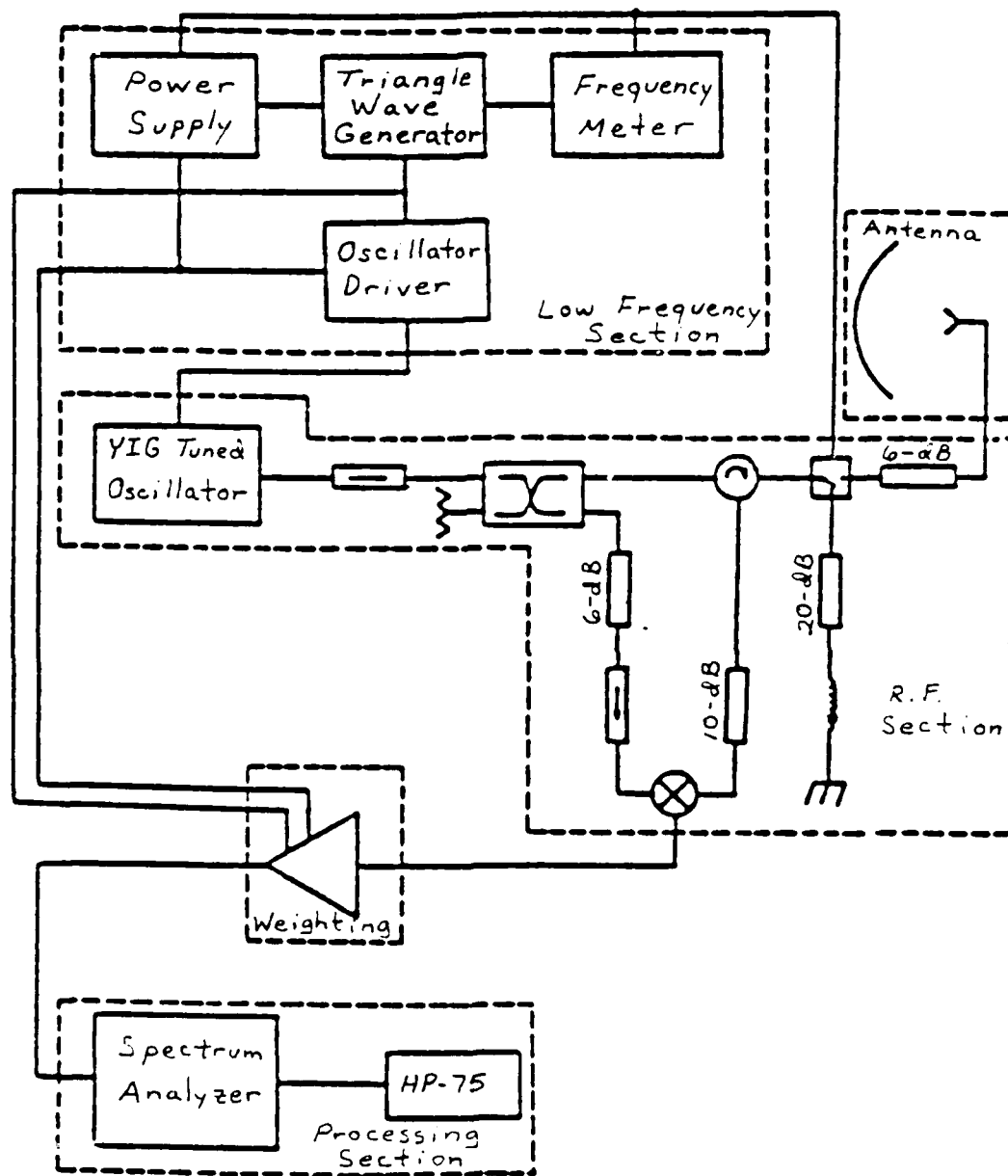


Figure 4.1: Block diagram of X-band SOURCESCAT radar (Zoughi, 1984).

Frequency	10 GHz
r.f. bandwidth	2 GHz
FM rate	100 Hz
range resolution (weighted)	12 cm
footprint (3.5 meter range)	20 x 20 cm

Table 4.1: SOURCECAT radar specifications.

$r_{res} = c/2B = 7.5$ cm. Fine resolution in azimuth and the plane wave condition are satisfied at ranges within the near and intermediate fields of the antenna by using a parabolic dish antenna with feed slightly displaced from the focal point. Pertinent system specifications are found in Table 4.1 (See [Zoughi, 1984] for a more detailed discussion of this radar).

4.1.2 PAIR

PAIR operates at C and X band and is shown in block diagram form in Fig. 4.2. Notice that this radar

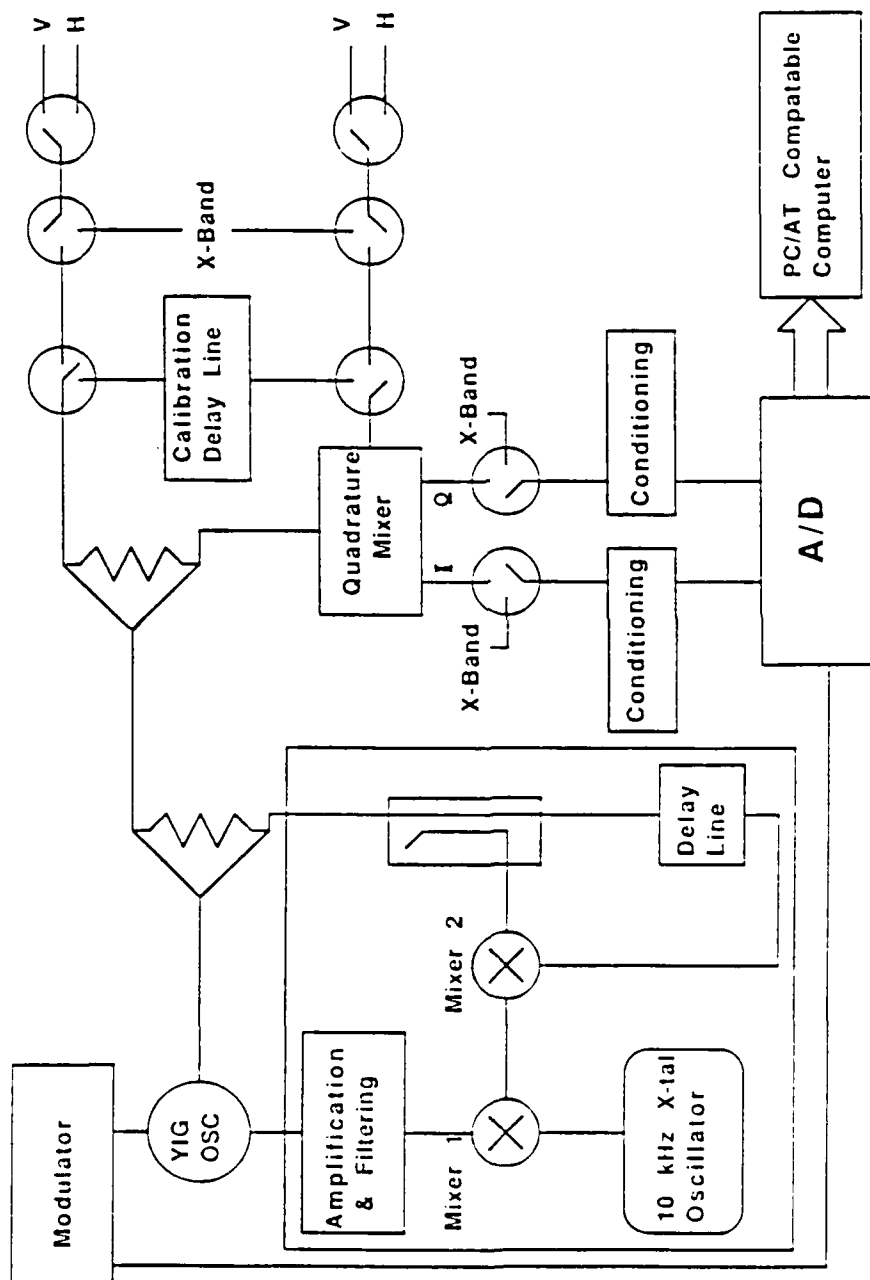


Figure 4.2: Block diagram of the C-band section of PAIR (the X-band section is nearly identical).

operating frequency	6 GHz	11 GHz
r.f. bandwidth	500 MHz	500 MHz
modulation	triangular	triangular
modulation rate	70 Hz	70 Hz
range resolution (without weighting)	30 cm	30 cm
footprint (3.5 m range)	20 x 20 cm	20 x 20 cm
dynamic range	>50 dB	>50 dB
transmit power	10 mW	10 mW

Table 4.2: PAIR specifications.

is a modified and enhanced version of SOURCESCAT.

Components of PAIR not found in SOURCESCAT include:

(1) a phase-locked-loop for frequency linearization and phase stabilization; (2) I and Q channels to provide amplitude and phase information; (3) digital data acquisition system to provide flexibility in signal processing; and (4) multipolarization capability.

Other enhancements include a focussed offset-fed parabolic-dish antenna to improve side-lobe and cross-polarization performance (version 2 of PAIR only).

Pertinent system specifications are found in Table 4.2.

4.1.2.1 Discussion of circuitry unique to PAIR

A phase-locked loop (PLL) is used to improve the performance of the YIG VCO. It does this by linearizing the frequency-versus-driving current characteristic of the oscillator - Caputi [1973] used this technique and provided an analysis of this technique for Backward Wave Oscillators. Oscillator nonlinearities increase the amplitude of range sidelobes and the change in such nonlinearities versus time and temperature adds uncertainty to phase measurements. Figure 4.3 illustrates the frequency-versus-driving current (f vs. i) response for a typical YIG oscillator. Maximum Δf in Fig. 4.3 is around 5-10 MHz for the oscillators we used. Deviations from linear are due to loading of the YIG sphere by the active element and to interaction between resonance modes within the sphere [Clark and Swartz, 1971]. Figure 4.4 illustrates the effect of bias level on the impedance of a typical active element (X-band oscillator diode) - this is important because the bias level can change with time and temperature. This impedance variation is sufficient to cause output frequency variations of 2 to 3 MHz per volt change of bias [Clark and Swartz, 1971]. Figure 4.5 shows what happens when a spurious resonance is excited within the sphere that crosses the main resonance at about 8.5 GHz

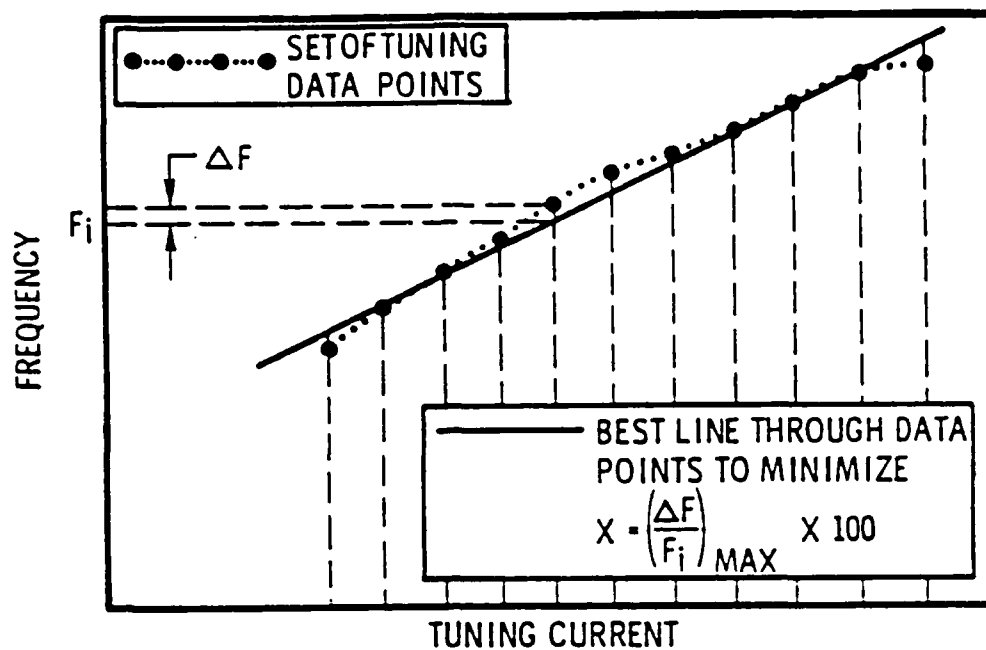


Figure 4.3: Frequency-versus-driving-current response of a typical YIG oscillator (Clark and Swartz, 1971).

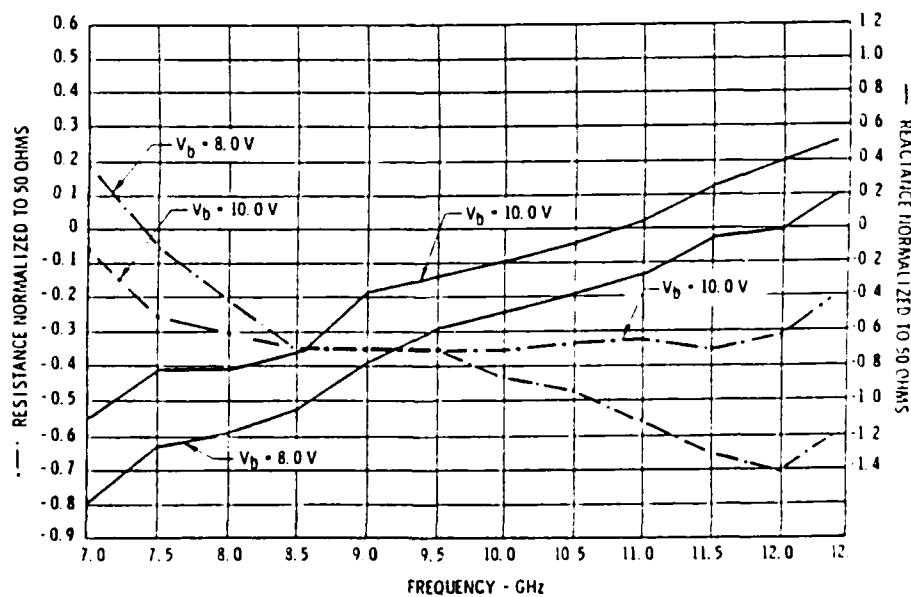


Figure 4.4: Effect of bias level on the impedance of a typical X-band oscillator diode (Clark and Swartz, 1971).

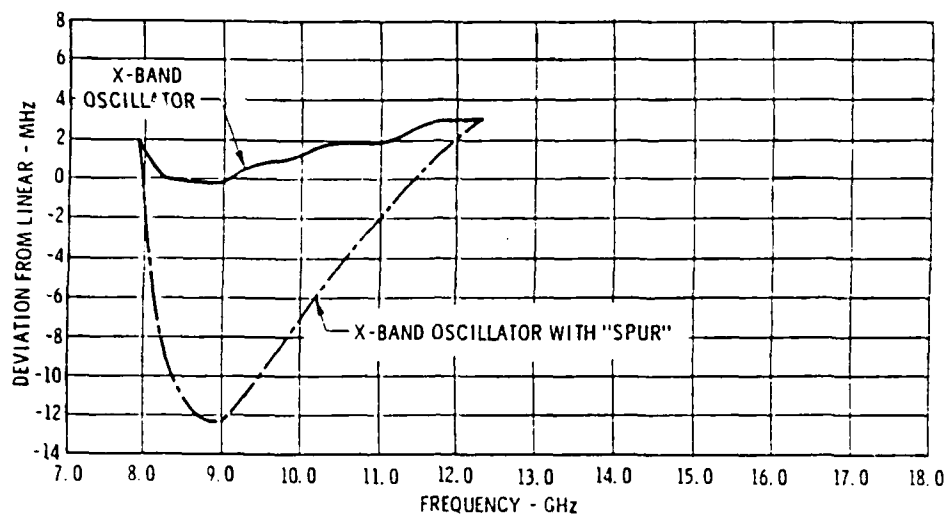


Figure 4.5: Effect of a spurious YIG-sphere resonance on linearity of a YIG-tuned oscillator (Clark and Swartz, 1971).

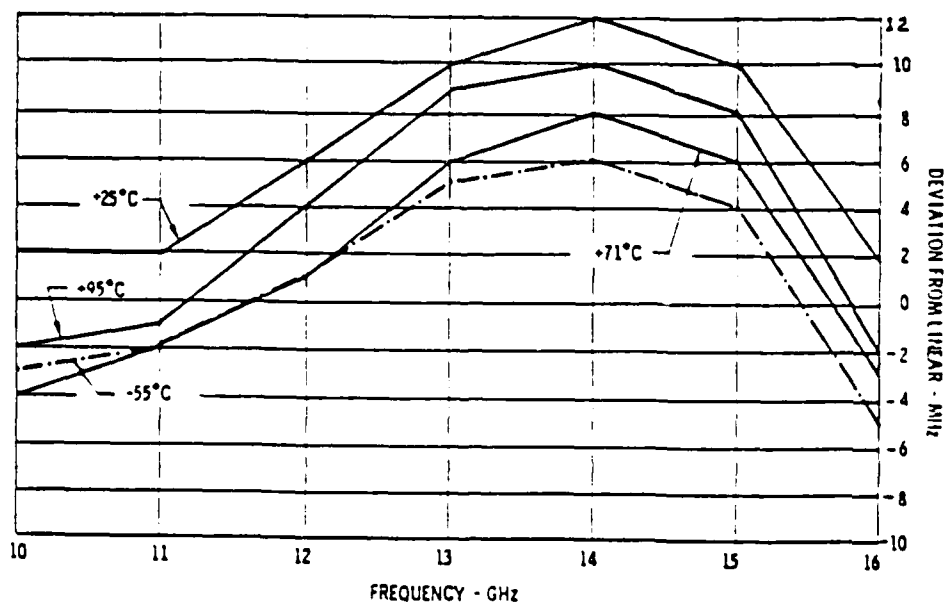


Figure 4.6: Effect of temperature on linearity of a typical heated YIG-tuned oscillator (Clark and Swartz, 1971).

[Clark and Swartz, 1971]. Figure 4.6 indicates several MHz variation in deviation from linear over the temperature range of -55°C to 100°C even when the YIG heater is used. See Clark and Swartz [1971] for a thorough discussion of factors which affect YIG oscillator linearity.

Both in-phase (I) and quadrature (Q) mixer products must be available to obtain phase information for a homodyne receiver such as ours. A commercially available quadrature mixer with phase imbalance of less than 6° and amplitude imbalance of less than 0.3 dB was selected to provide I and Q channel outputs.

Amplifiers and filters for the two channels were carefully designed and selected so that balance is maintained within one or two tenths of a dB in amplitude and a few degrees in phase. The low-noise amplifiers consist of two stages. The first stage uses LM194 matched transistor pairs, and the second stage uses AD625 instrumentation amplifiers. The two passive 10-section Bessel filters, a 2-kHz low-pass and a 15-kHz high-pass for each channel, are commercial units.

Processed I and Q channel outputs are digitized to 12 bits at a 40kHz rate by an Analog Devices RTI-860 board. A Compaq Portable II then reads the data from the RTI-860 and stores them on floppy disks or on Bernoulli cartridges. Programs stored on the Compaq

permit computer controlled acquisition of multipolarized data, data previewing with flexible windowing, and preliminary data analysis.

Multipolarization capability was added because of the current emphasis on polarimetric measurements. Use of a dual-polarization feed in an offset-fed parabolic dish configuration provides better performance than a standard center-fed configuration: higher cross-polarization sensitivity and lower side-lobes. A dual-polarization conical feed optimizes the antenna cross-polarization and side-lobe performance. It was used instead of a diagonal horn because of the convenience in machining.

4.1.3 STEFRAD

To obtain better performance than is possible with PAIR, we designed and built a step frequency radar to operate at 5.5 and 13.9 GHz. Improved stability is possible with this type of radar because a synthesized source (i.e., a source phase-locked to a crystal oscillator) can be used. Thus, problems associated with linearity and phase noise can be greatly reduced.

By incorporating commercially available network analyzers the design and construction of such radars becomes relatively easy. A high degree of accuracy in microwave vector measurements and dynamic range exceeding 100 dB are additional incentives for using

operating frequency	5.3 GHz	13.6 GHz
r.f. bandwidth	500 MHz	500 MHz
range resolution (without weighting)	30 cm	30 cm
footprint (3.5 m range)	1.2 x 1.2 m	1.2 x 1.2 m
dynamic range	>70 dB	>70 dB
transmit power	10 mW	10 mW

Table 4.3: STEFRAD specifications.

these devices.

A block diagram for STEFRAD is shown in Fig. 4.7. An HP-8753A network analyzer serves as the core. This unit compares the target return, in amplitude and phase, to a stable reference signal. The front-end consists of an up-converter, a down-converter, and appropriate antennas and switching. A filter in each section removes unwanted sidebands and an amplifier in each section compensates for mixing and cabling losses. Horn antennas were used because the systems have recently been built and are just now moving past the initial testing stage. Although these antennas have wide beamwidth and moderate side-lobe performance, they perform well in a cross-polarized configuration. See Table 4.3 for a list of pertinent system parameters.

4.2 Comparison of modes of operation

4.2.1 SOURCESCAT

The SOURCESCAT radar is triangularly modulated. The frequency of the output of this radar is thus proportional to target range. Consider the return for a point target: Let the transmitted signal be

$$A \cos(2\pi f_c t + 2\pi \Delta f t^2 + \phi). \quad (4.1)$$

At time $t + \tau$ the signal becomes

$$A \cos(2\pi f_c (t + \tau) + 2\pi \Delta f (t + \tau)^2 + \phi). \quad (4.2)$$

Then the return from the target is

$$A_t \cos[2\pi f_c (t + \tau) + 2\pi \Delta f t (t + \tau) + \phi - 2\beta_c z_t - \beta_s z_s + \phi_t], \quad (4.3)$$

where

A_t = amplitude of the return signal

Δf = time slope of frequency increase

= two-way propagation time

ϕ_t = phase shift due to the target

$\beta_c = 2\pi f_c / c$

f_c = lowest r.f. frequency transmitted

z_t = slant range to target

β_s = effective propagation constant within system
components at frequency f_c

z_s = effective length of system paths

The signal at the radar output is then

$$(AA_t/2) \cos((2\pi \Delta f \tau) t + 2\pi \Delta f \tau^2 + 2\beta_c z_t + \beta_s z_s - \phi_t). \quad (4.4)$$

If $\Delta f = B / (T_m/2)$,

where B = r.f. bandwidth

T_m = modulation period,

and $\tau = 2R/c$,

where R is the range to the target

and c is the speed of light,

then the frequency of the radar output signal is

$$\Delta f \tau = (B/(T_m/2))(2R/c) = 4BR/cT_m. \quad (4.5)$$

The return is not a single frequency, however, due to the change in phase of the return as the modulation slope changes sign. The actual voltage return spectrum, as determined by a scalar spectrum analyzer, is approximately

$$\begin{aligned} F(f) = & \left| \int_0^{T_m/2} \exp(j(2\pi\Delta f\tau - \omega)t) dt \right| \\ & + \left| \int_{T_m/2}^{T_m} \exp(j(2\pi\Delta f\tau - \omega)t) dt \right| \times (\delta(f - nf_m)) \\ = & 2[\sin((2\pi\Delta f\tau - \omega)(T_m/4)) / (2\pi\Delta f - \omega)] \times (\delta(f - nf_m)), \\ & n = 1, 2, 3, \dots \quad (4.6) \end{aligned}$$

For this radar we obtained data using an HP3585A spectrum analyzer and stored the data on mini data-cassettes via an HP-75 field computer. To obtain an accurate estimate of the target return envelope we set the resolution bandwidth of the spectrum analyzer to include at least one spectral line ($> f_m$) and set the video bandwidth to average about ten up and ten down sweeps.

Although SOURCESCAT is a simple, reliable, and

easy-to-use instrument, it does not provide for measurements of phase and flexibility in data analysis. These are the primary reasons that PAIR was built.

4.2.2 PAIR

With PAIR, target amplitude and phase spectra are obtained by performing a complex FFT on the average of ten time samples of I and Q channel data - the averaging is done to reduce system effects. The resulting spectrum for a point target is

$$\begin{aligned}
 F(k) &= \sum_{n=0}^{N-1} (AA_t/2) \exp[j(2\pi\Delta f \gamma n T_s + 2\pi\Delta f \gamma^2 + 2\theta_c z_t + \theta_s z_s - \phi_t)] \\
 &\times \exp(-j(2\pi k/NT_s) n T_s) \\
 &= (AA_t/2) \exp[j(2\pi\Delta f \gamma^2 + 2\theta_c z_t + \theta_s z_s - \phi_t)] \\
 &\times \exp[-j(((N-1)/2)(2\pi\Delta f \gamma - (2\pi k/NT_s))T_s)] \\
 &\times \sin[(NT_s/2)(2\pi\Delta f \gamma - (2\pi k/NT_s))] \\
 &/ (\sin[(T_s/2)(2\pi\Delta f \gamma - (2\pi k/NT_s))]) \quad (4.7)
 \end{aligned}$$

Target amplitude information is easily obtained.

Several other factors must be determined, however, before the target phase, ϕ_t , can be extracted.

Typically we are most interested in the copolar phase ($\phi_{tVV} - \phi_{tHH}$). Assuming that the system is stable, measurement of a known target such as a sphere allows us to find the target copolar phase. For a sphere we expect $\phi_{VV} = \phi_{HH}$. Thus, measuring the return from a sphere, we obtain

$$\phi_{VV\text{sph}} - \phi_{HH\text{sph}} = 2\pi\Delta f (\tau_{VV}^2 - \tau_{HH}^2) + \theta_s (z_{SVV} - z_{SHH}) - ((N-1)/4) (2\pi\Delta f (\tau_{VVs\text{ys}} - \tau_{HMs\text{ys}})) T_s \quad (4.8)$$

where T_s = sampling period

$\tau_{VVs\text{ys}}, \tau_{HMs\text{ys}}$ = system delay for VV and HH channels

τ_{VV}, τ_{HH} = system delay plus propagation delay to target and back for VV and HH polarizations

z_{SVV}, z_{SHH} = system path lengths for VV and HH channels

For a stable system $\theta_s(z_{SVV} - z_{SHH})$ and $2\pi\Delta f (\tau_{VVs\text{ys}} - \tau_{HMs\text{ys}})$ will be nearly the same when the target measurement is made. For short ranges and values of Δf that were used the $2\pi\Delta f (\tau_{VV}^2 - \tau_{HH}^2)$ term is negligible. Thus

$$\phi_{tVV} - \phi_{tHH} = \phi_{tVV\text{meas}} - \phi_{tHH\text{meas}} - (\phi_{VV\text{sph}} - \phi_{HH\text{sph}}). \quad (4.9)$$

For this type of scheme to produce accurate phase measurements it is essential that the system be very stable. The oscillator must be stable from VV measurement to HH measurement. A drift of 5 MHz in f_c causes 13° phase difference at a range of 5 m. Stability from measurement to calibration is also important but not as critical if care is taken in system design. A drift of 5 MHz in f_c in this instance only introduces an error of about 2° if there is a 10 cm difference between the HH and VV channel path lengths. Ideally one should phase-match the VV and HH

channels. In that case it is not necessary to use a sphere to determine the copolar phase.

4.2.3 STEFRAD

The step frequency radar operates in a mode similar to that of PAIR. At short ranges, the resulting equations for a point target return are identical. Conceptually the only difference is that a step frequency radar measures return amplitude and phase at a fixed number of discrete frequencies whereas an FM-CW radar measures amplitude and phase of a frequency shift.

Iizuka [1984] explained the operating mode in terms of a vector addition of returns from several targets. Consider a system using frequencies of $f_c + n\Delta f$, $n=0,1,2,\dots,N-1$. Measured amplitude and phase at $f_c + m\Delta f$ for a scene consisting of four targets (See Fig. 4.8) is

$$\begin{aligned} H_m = & s_0 E_0 / z_0^2 \exp(j(2(2\pi)(f_c + m\Delta f)/c)z_0) + \\ & s_1 E_0 / z_1^2 \exp(j(2(2\pi)(f_c + m\Delta f)/c)z_1) + \\ & s_2 E_0 / z_2^2 \exp(j(2(2\pi)(f_c + m\Delta f)/c)z_2) + \\ & s_3 E_0 / z_3^2 \exp(j(2(2\pi)(f_c + m\Delta f)/c)z_3) \end{aligned} \quad (4.10)$$

where s_0, s_1, s_2, s_3 = voltage scattering coefficients
of targets 0, 1, 2, and 3

z_0, z_1, z_2, z_3 = slant ranges to targets 0, 1, 2, and 3

E_0 = transmitted signal

For the case of N targets

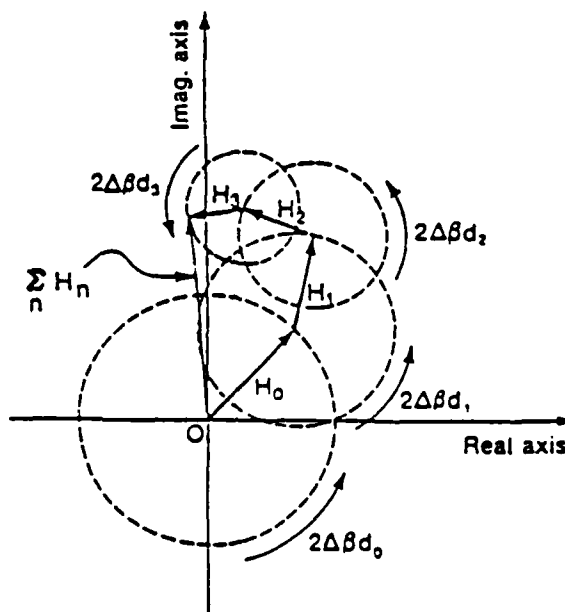


Figure 4.8: Vector addition of returns from four targets (Iizuka, 1984).

$$H_n = \sum_{k=0}^{N-1} s_k E_0 / z_k^2 \exp(j(2(2\pi)(f_c + n\Delta f)/c)z_k), \quad (4.11)$$

Consider the case of N targets at ranges of $z_0, z_0 + \Delta z, z_0 + 2\Delta z, \dots, z_0 + (N-1)\Delta z$ then

$$H'_n = (H_n \exp(-j2(2\pi)(f_c + n\Delta f)/c)z_0) = [\exp(-j2(2\pi)(f_c + n\Delta f)/c)z_0] \times \sum_{k=0}^{N-1} (s_k E_0 / z_k^2) \exp[j(2(2\pi)(f_c + n\Delta f)/c)k\Delta z] \quad (4.12)$$

If we let

$$h_k = (Ns_k E_0 / z_k^2) \exp[j(2(2\pi)(f_c/c)k\Delta z)] \quad (4.13)$$

then H'_n and h_k are related by a discrete Fourier Transform. That is,

$$H'_n = (1/N) \sum_{k=0}^{N-1} h_k \exp[j(2\pi)(kn/N)] \text{ and}$$

$$h_k = \sum_{n=0}^{N-1} H'_n \exp[-j(2\pi)(kn/N)] \quad (4.14)$$

where $N = c/2\Delta f\Delta z$.

Figures 4.9 - 4.11 are used to further illustrate how a step frequency radar works, assuming 8 stepped frequencies. The 8 waveforms in Fig. 4.9 correspond to phase shift encountered by the r.f. signal, of frequency $f_c + n\Delta f$, in propagating to the target and back, relative to phase shift similarly encountered by the r.f. signal of frequency f_c , for each of the 8 stepped frequencies and at 8 ranges from 0 up to the maximum unambiguous range. Note that one period of the waveform corresponds to a 2π phase shift. For example, $\pi/4$ phase shift occurs at Δf for a range of $R_u/8$, $\pi/2$ occurs at Δf for a range of $R_u/4$, etc.

The vector being measured by the network analyzer is of the form $A \exp(j\phi)$. Consider the measurements A_0 , $A_1 \exp(j4\pi\Delta f R)$, $A_2 \exp(j8\pi\Delta f R)$, ..., $A_7 \exp(j28\pi\Delta f R)$ by an 8-frequency step frequency radar and assume that $A_0 = A_1 = \dots = A$. At a range of $R = R_u/8$, the measurements

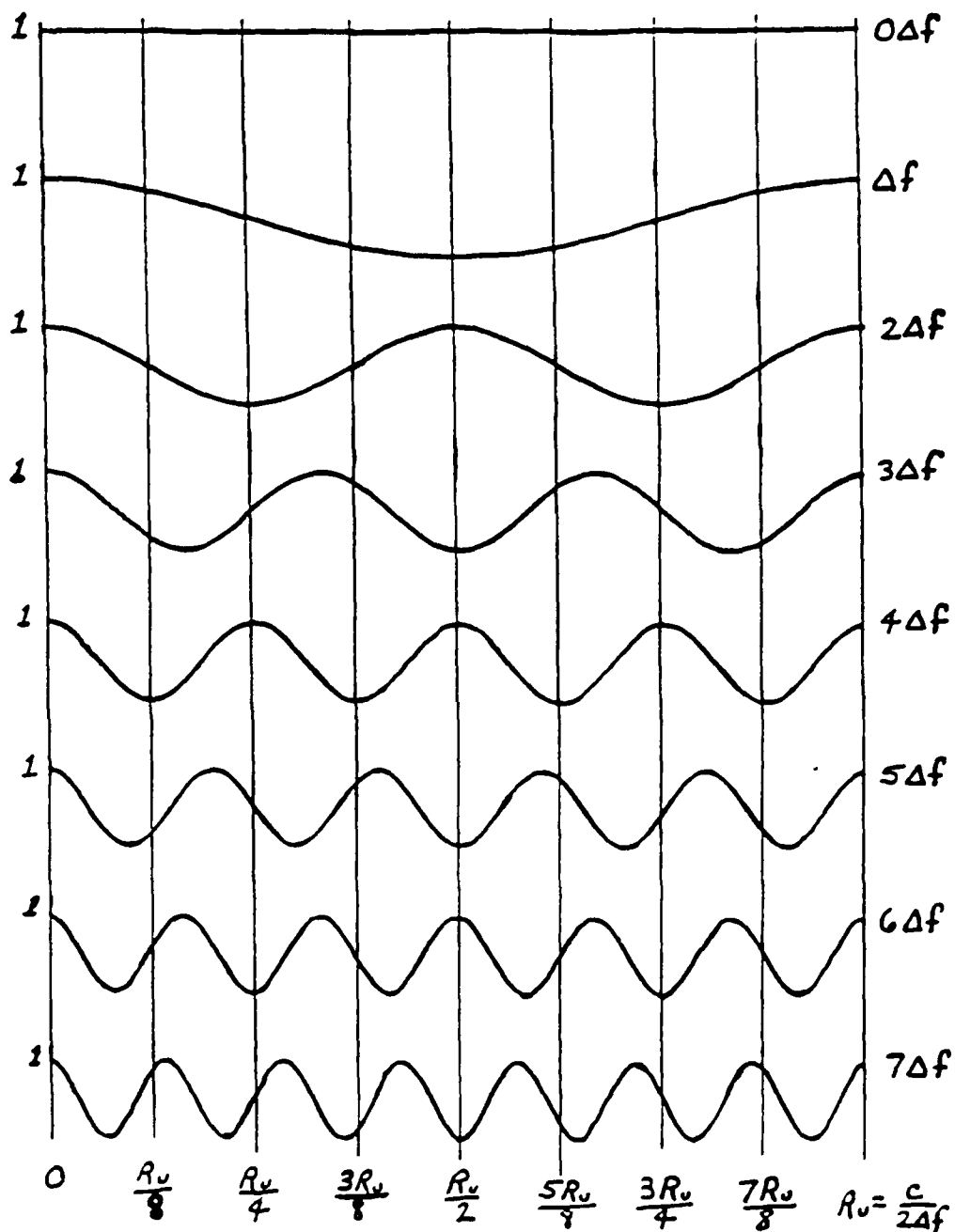


Figure 4.9: Relative phase shift encountered by r.f. signal in propagating to target and back, at all 8 frequency steps and various target ranges for an 8-frequency step frequency radar.

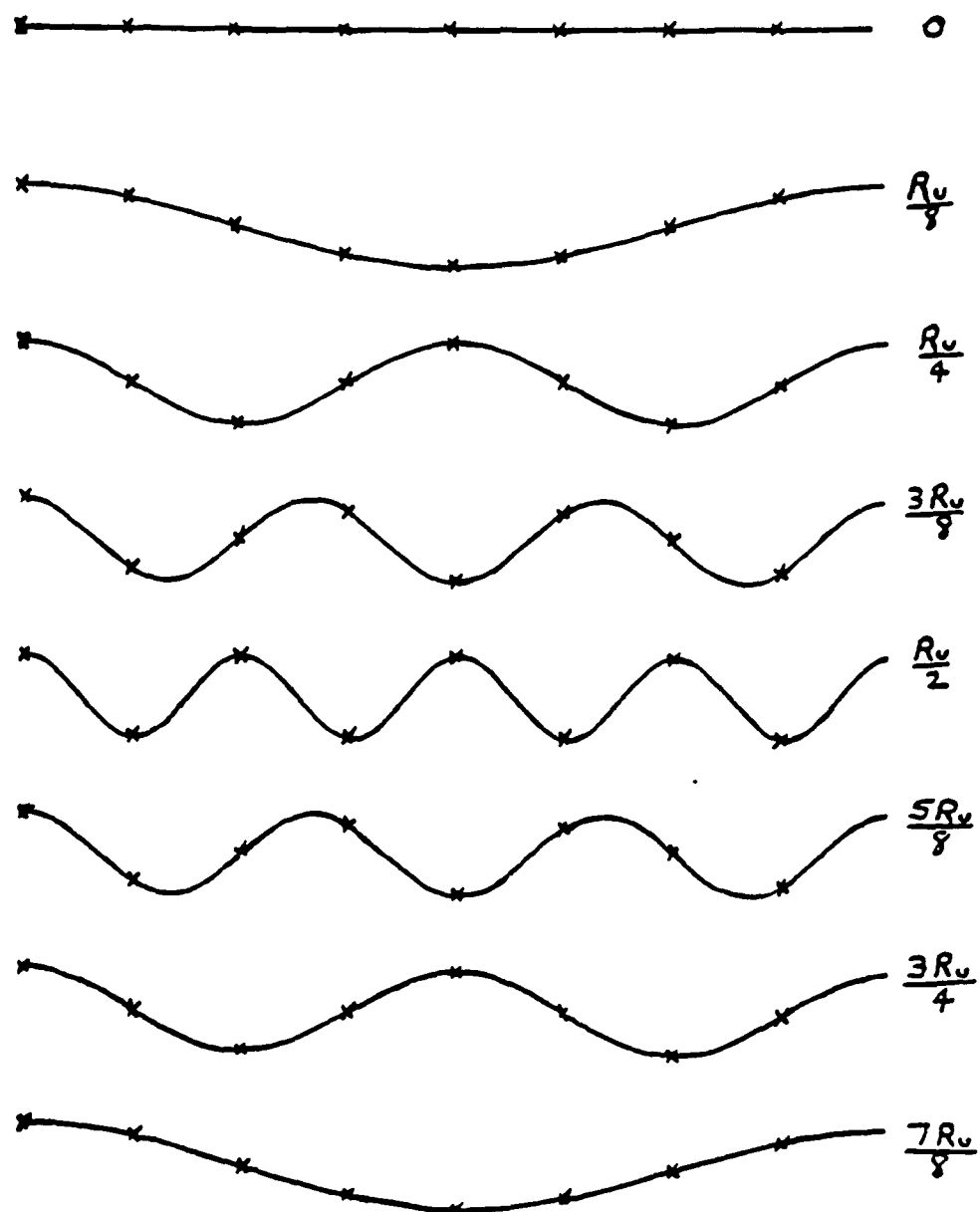


Figure 4.10: Real components of vectors sampled by an 8-frequency step frequency radar for various target ranges.

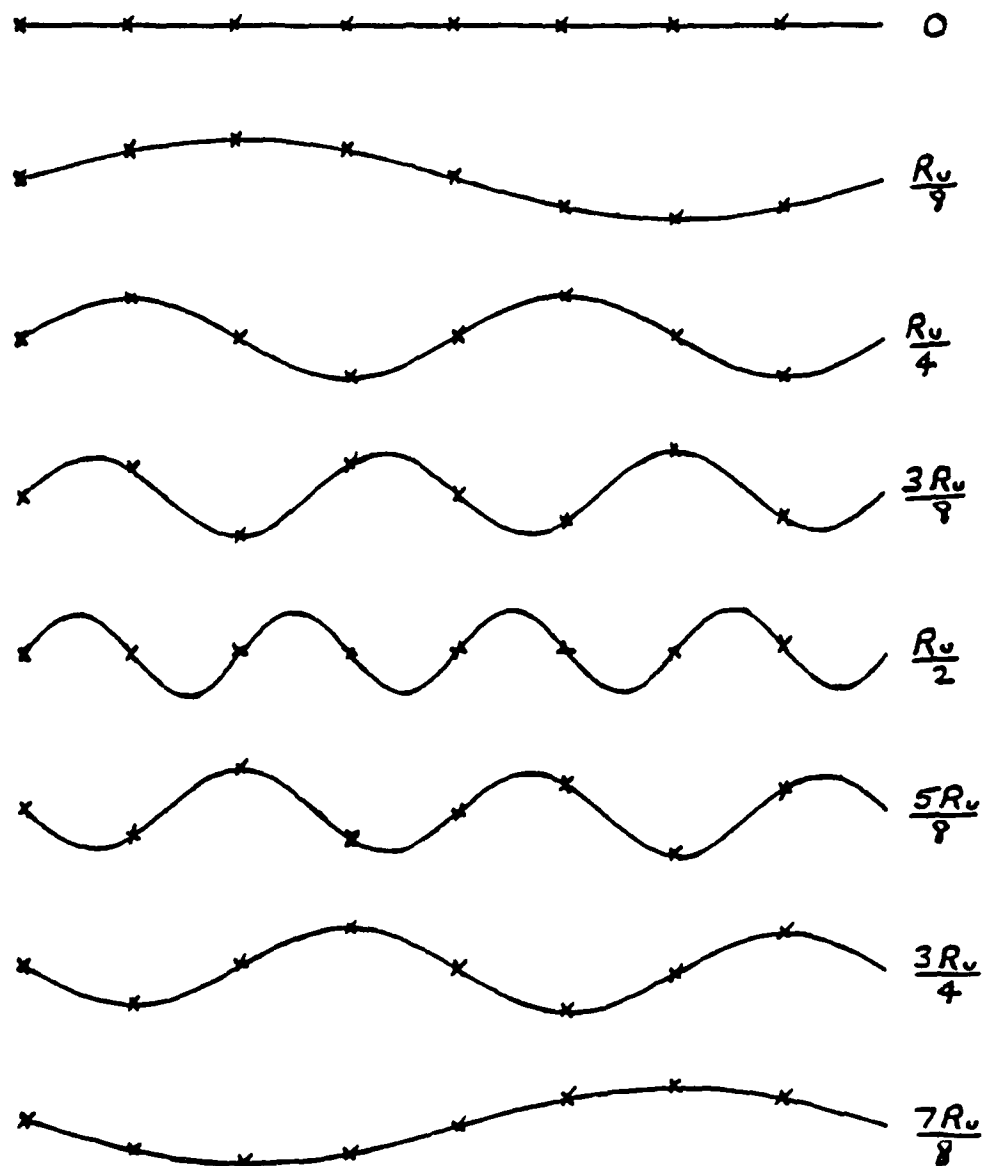


Figure 4.11: Imaginary components of vectors sampled by an 8-frequency step frequency radar for various target ranges.

correspond to A , $A \exp(j\pi/4)$, $A \exp(j\pi/2)$, ... , $A \exp(j7\pi/4)$ (See Fig. 4.9). The real components of this series are the indicated samples of the cosinusoidal wave shown in Fig. 4.10 at $R=R_u/8$, and the imaginary components are the indicated samples of the corresponding sinusoidal waveform in Fig. 4.11. Samples of waveforms for the other 7 ranges are shown as well in Figs. 4.10 and 4.11.

Notice that the frequency of the sampled waveform increases as the range increases to a range of $R_u/2$. At ranges greater than $R_u/2$ the frequency decreases and the sign of the sinusoidal waveform (i.e., the imaginary component) becomes negative. The sign change in the imaginary component makes it possible to distinguish between ranges of $R_u/2 < z < R_u$ and $0 < z < R_u/2$. We cannot distinguish ranges greater than R_u from ranges less than R_u due to the sampling process.

Assuming that the return amplitude is constant at each step, the return for a point target at a range of z_t is

$$\begin{aligned}
 h_k &= \exp(-j\phi_t) \exp((j4\pi f_c/c)z_t + j(2\pi f_c/c)z_s) \\
 &\times \sum_{n=0}^{N-1} A \exp((j4\pi n \Delta f/c)z_t) \exp(-j2\pi(kn/N)) \\
 &= \exp(-j\phi_t) \exp((j4\pi f_c/c)z_t + j(2\pi f_c/c)z_s)
 \end{aligned}$$

$$\begin{aligned}
& \times \exp(-j((N-1)/2)(2\pi(2\Delta f z_t / c - k/N))) \\
& \times \sin(N/2(2\pi(2\Delta f z_t / c - k/N)))/\sin(1/2(2\pi(2\Delta f z_t / c - k/N))) \\
& = \exp(2\theta_c z_c + \theta_s z_s - \theta_t) \\
& \times \sin(N/2(2\pi(2\Delta f z_t / c - k/N)))/\sin(1/2(2\pi(2\Delta f z_t / c - k/N)))
\end{aligned}
\tag{4.15}$$

Notice the similarity between this expression and the one shown for PAIR; only the $2\pi\Delta f \gamma^2$ term is absent here. As was the case with PAIR, amplitude data are easily obtained. Copolar phase is determined in the same manner as for PAIR.

The sense of the phasor rotation is somewhat arbitrary and depends on the phase reference. In our radar the phasor rotation opposes that of Iizuka such that

$$H_n = \sum_{k=0}^{N-1} (s_k E_0 / z_k^2) \exp(-j((4\pi(f_c + n\Delta f)/c)(z_0 + k\Delta z)))$$

If we set

$$H'_n = N H_n \exp(-j2(2\pi(f_c + n\Delta f)/c)(z_0)) \text{ and}$$

$$h_k = (s_k E_0 / z_k^2) \exp(-j(4\pi/c)(k f_c \Delta z)), \text{ then}$$

$$H'_n = \sum_{k=0}^{N-1} h_k \exp(-j(2\pi(kn/N)))$$

$$\text{and } h_k = (1/N) \sum_{n=0}^{N-1} H'_n \exp(j(2\pi(kn/N))). \tag{4.16}$$

That is, we use the inverse FFT to discriminate target ranges given the sampled vector measurements.

4.3 Calibration and performance

4.3.1 SOURCECAT

We used a 12" Luneberg lens to calibrate this radar during the 1987 experiment and found only about ± 1 dB variation in the return over a temperature range of -25°C to 5°C . Delay line readings were taken to track the variation.

4.3.2 PAIR

We used an 8" Luneberg lens and an active radar calibrator (ARC) to obtain calibration readings for this radar during the 1988 experiment. At the time we were unaware that a Luneberg lens does not work well for systems with small bistatic angles. Thus we had to rely on a comparison of returns from the lens and the not-well-characterized ARC to obtain a calibration value. Variations in the delay line readings were observed to be about ± 1 dB.

During the 1989 experiment we again used the 8" Luneberg lens, because of our single antenna configuration. We found a variation of about ± 2 dB in the return over a temperature range of -15°C to 5°C . Delay line readings were taken to track the variation.

The phase performance for this radar has not been well characterized. We observed, using an HP-3585 spectrum analyzer, that we were able to adjust the PLL to obtain a nearly ideal sinc function return for a

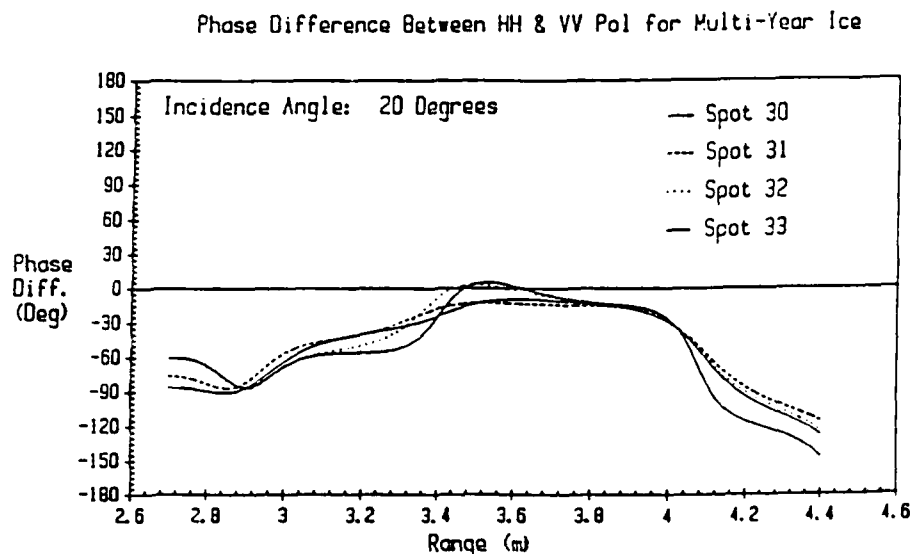


Figure 4.12: Uncalibrated copolar phase measured by PAIR for several spots on a smooth saline ice surface.

point target. We also found that the radar has reasonable phase stability; figure 4.12 indicates the copolar phase for several spots on a smooth ice surface at 20° incidence, taken over a one hour time interval. Thus we have some confidence in this radar.

The performance for weaker targets and long-term stability have not been determined.

4.3.3 STEFRAD

We used an 8" Luneberg lens and a diplane consisting of 2-10"x10" metal plates to calibrate this

radar during the 1989 experiment and found about ± 1 dB variation in the return over a temperature range of -15°C to 5°C . Delay line readings were taken to track the variation.

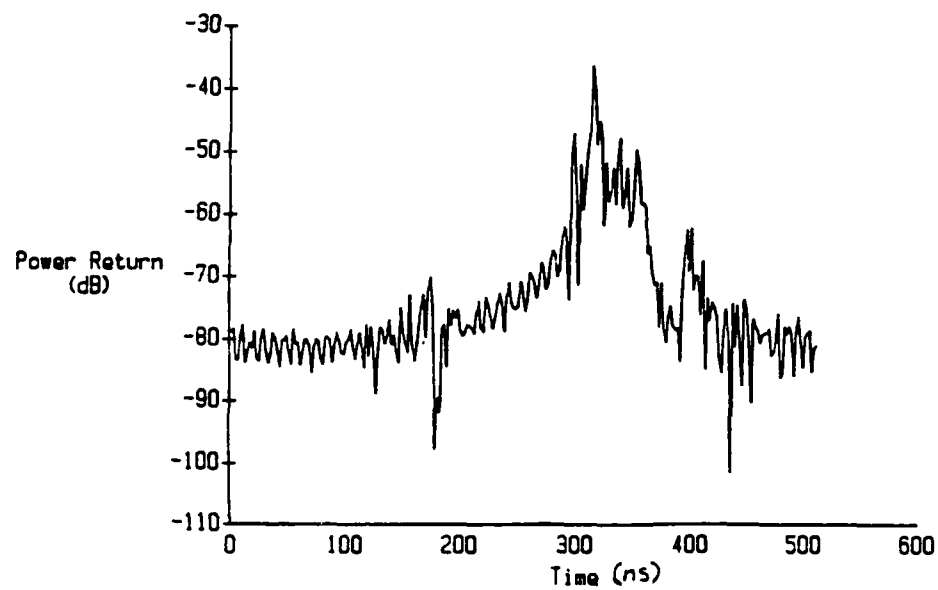
We have been able to study the phase performance in some depth. Figure 4.13 illustrates measured backscatter from an 8" sphere at C band, before and after subtraction of the phase response. Figure 4.14 shows the same measurement at Ku band. Note that the system response is reduced by nearly 40 dB for C band. In these cases the sky (system) and target responses were taken within a minute of each other, however.

The C-band radar is considerably less stable than the Ku- band radar over time. With the Ku-band radar we were able to remove >30 dB of the system response 30 minutes to 1 hour after a sky reading was taken. A sky reading for C band was good for less than 5 minutes.

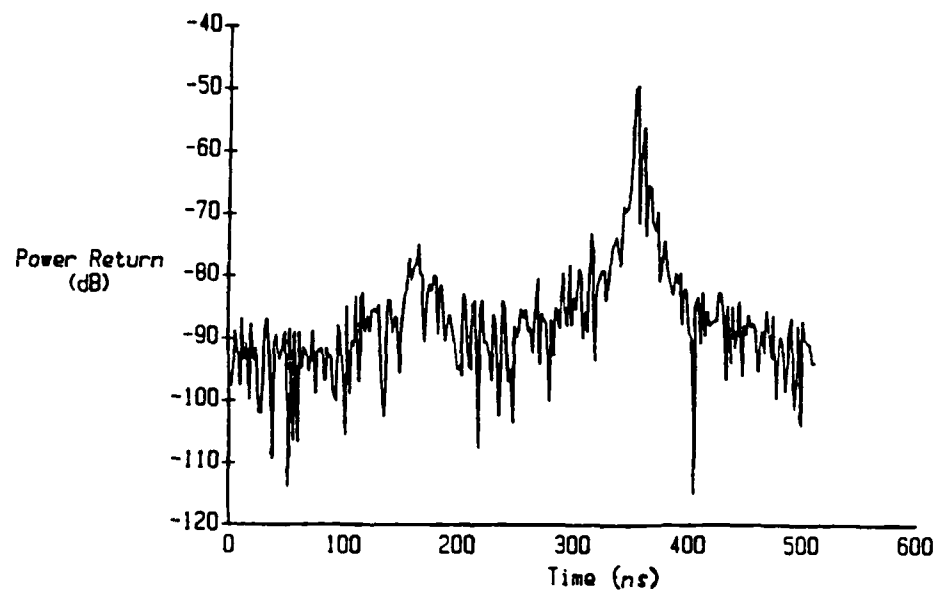
A simple experiment was done to study the copolar phase response: VV and HH polarization responses were determined for an 8" metal sphere. A known phase shift was then inserted in the VV channel and the measurements were repeated. After removing the system response of each sphere measurement we determined

$$\begin{aligned} \phi_{VV} - \phi_{i,H} &= \phi_{VV\text{insert}} - \phi_{HH\text{insert}} \\ &- (\phi_{VV\text{noinsert}} - \phi_{HH\text{noinsert}}) \end{aligned} \quad (4.17)$$

for each of three inserts. Figure 4.15 shows the

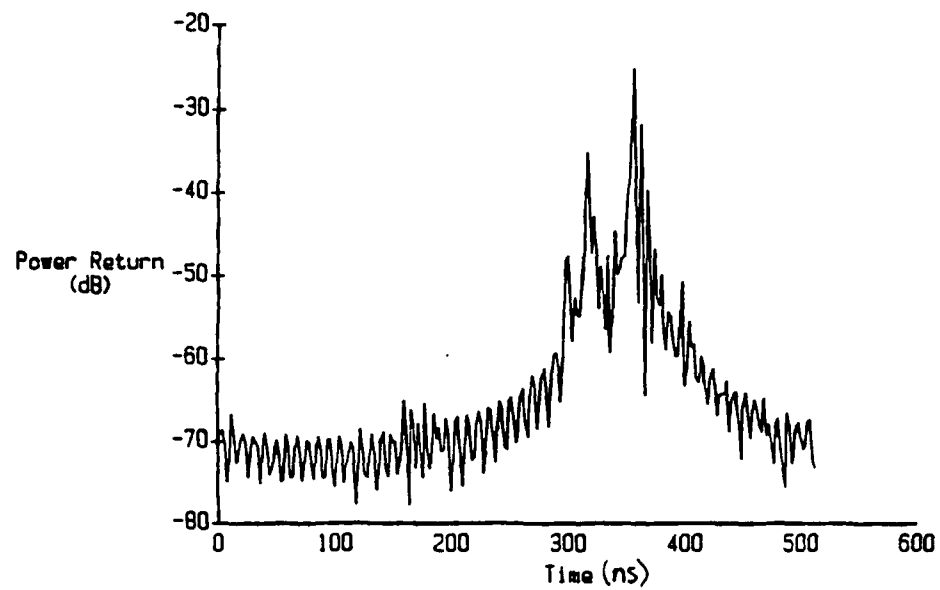


(a)

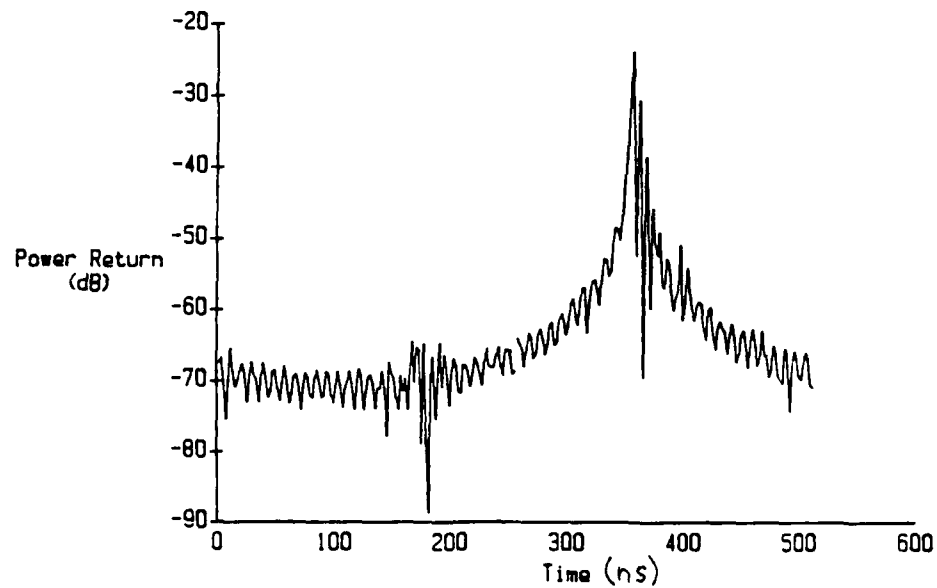


(b)

Figure 4.13: Return from an 8" sphere as output from C-band STEFRAD (a) before and (b) after removal of the system response.



(a)



(b)

Figure 4.14: Return from an 8" sphere as output from Ku-band STEFRAD (a) before and (b) after removal of the system response.

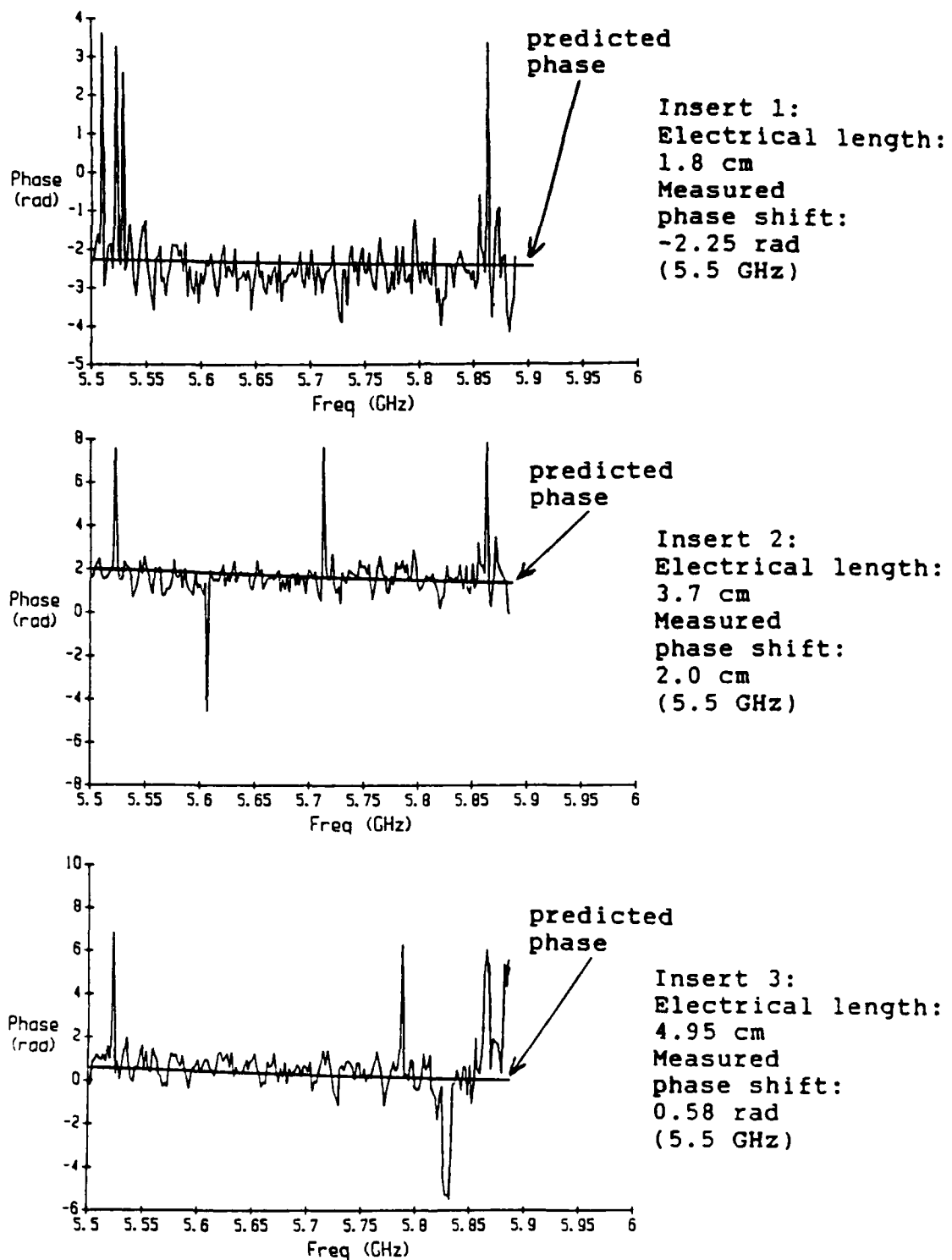


Figure 4.15: Results of C-band copolar phase experiment using inserts of known phase shift.

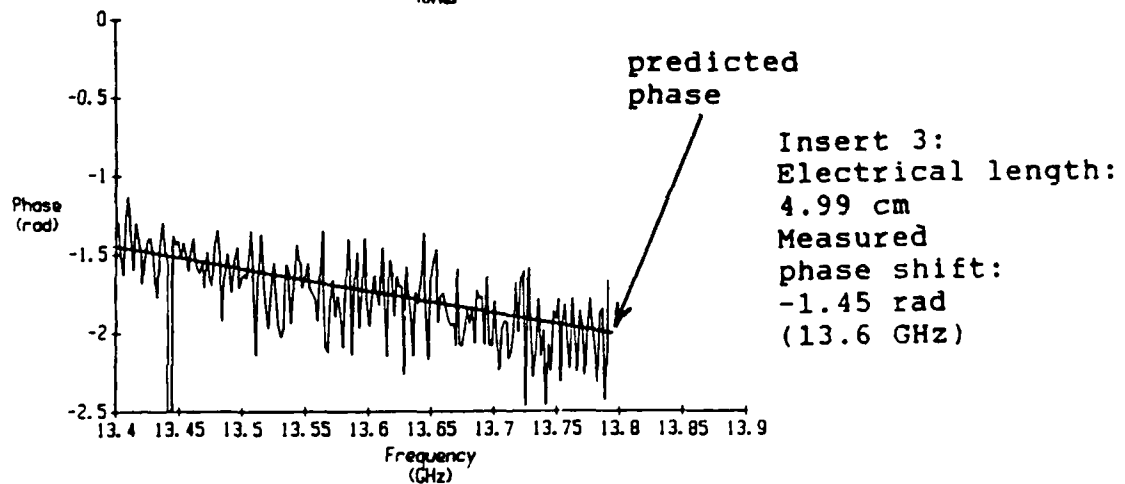
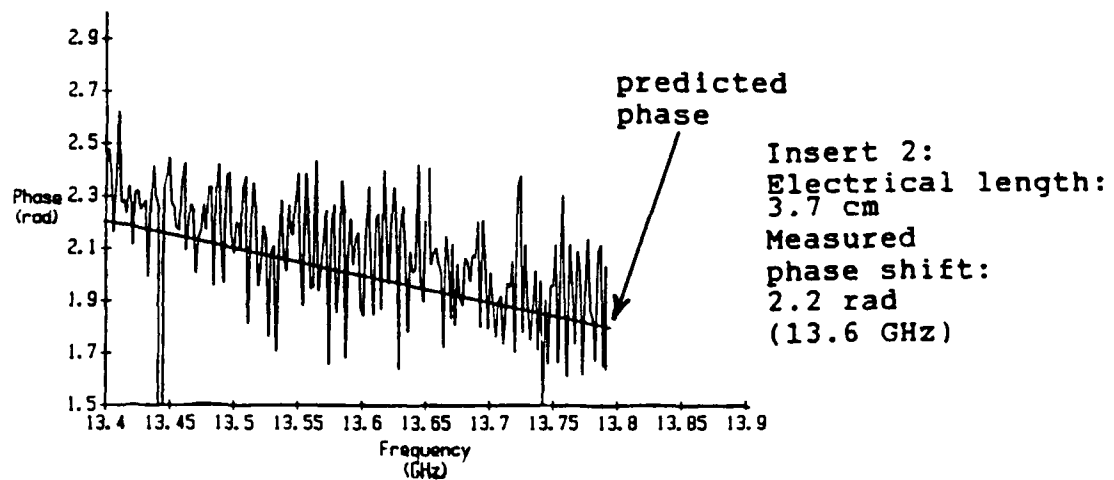
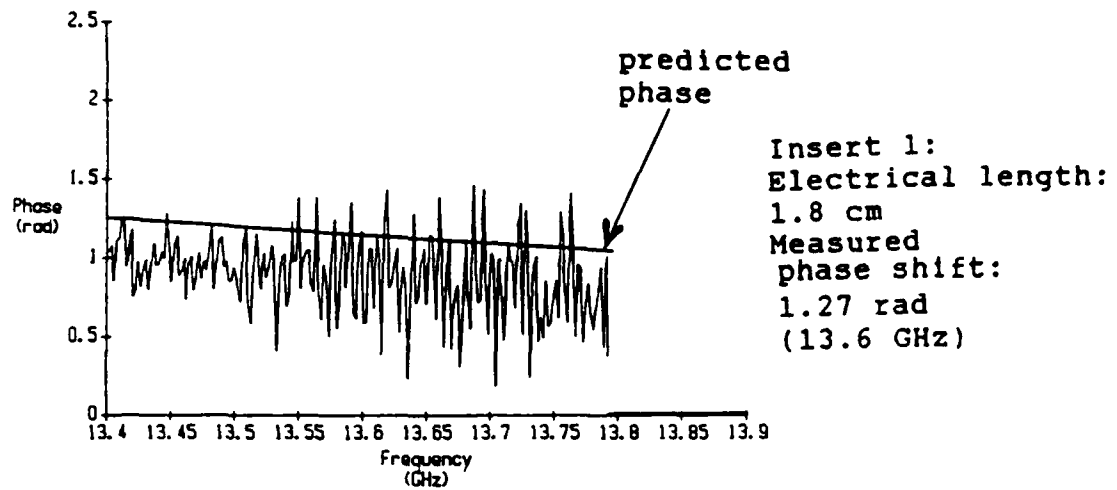


Figure 4.16: Results of Ku-band copolar phase experiment using inserts of known phase shift.

results for C band and Figure 4.16 the results for Ku band - notice that we plotted the phase as it was determined by the network analyzer; in the presence of multiple targets it is necessary to determine copolar phase at the appropriate peaks of the IFFT.

The measurements for C band were done outdoors using a styrofoam mount for the sphere. The measured phase was generally within $\pm 30^\circ$ of the predicted phase. Errors in the unwrapping routine are responsible for the large spikes; notice that these are of magnitude 2π . Motion of the mount, due to a slight breeze, caused most of the remaining variation.

The measurements at Ku band were conducted inside with antennas pointing directly into a large metal door which was partly covered with microwave absorbers. The measured phase was generally within $\pm 20^\circ$ of the predicted phase except for insert 1 (the offset for insert 1 can be attributed to a faulty connector). Errors in the unwrapping routine are responsible for the large spikes, the same as for the C band data. Vibration of the styrofoam stand by the room ventilation and interference from the door (the door return could not be completely removed due to blockage from the sphere) caused most of the remaining variation.

5.0 Analysis of ice sheet physical parameters

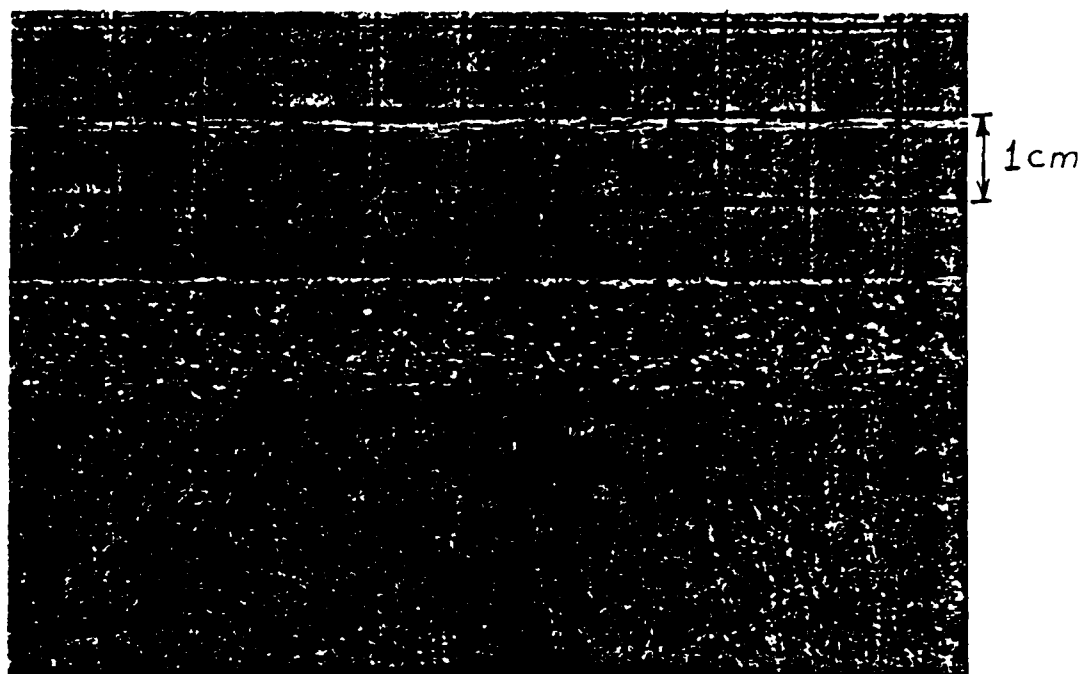
In this chapter we determine parameters to be used as inputs to the theoretical models discussed in Chapter 2, and thus prepare the groundwork for the comparisons of measurements and theory presented in Chapter 6. The ice sheet parameters we determined are listed in Tables 3.2 and 3.3.

5.1 Surface roughness

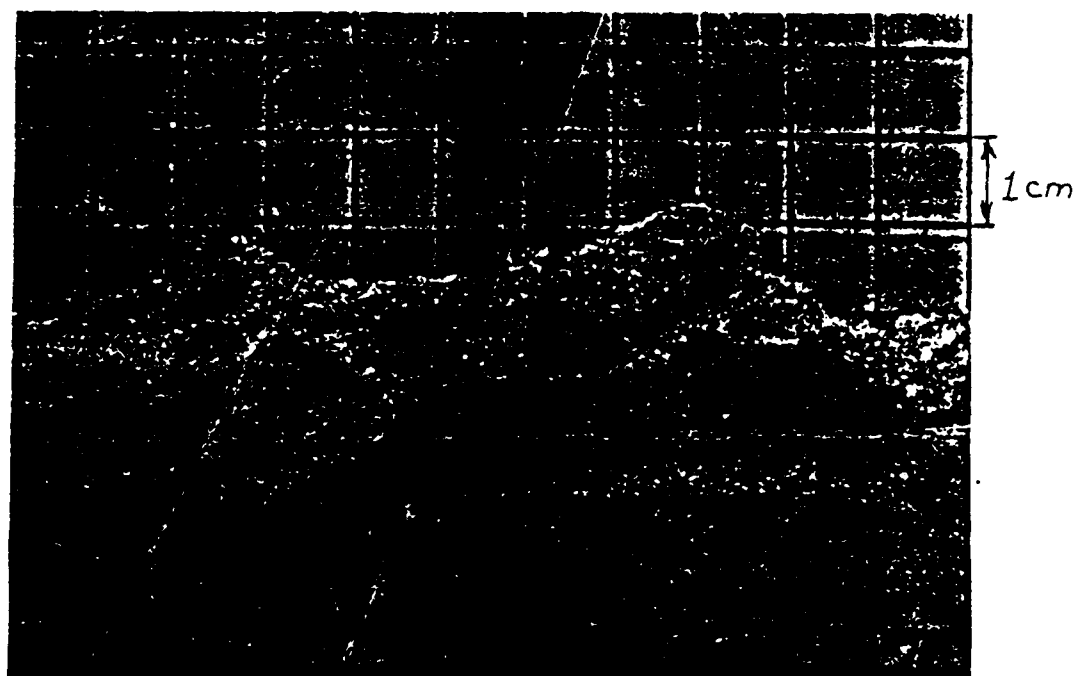
During 1987 we estimated rms height by inspection and used contextual information, previously reported surface measurements, and fits to theory to estimate correlation length. These techniques were unsatisfactory because of the large uncertainty.

During 1988, for each ice sheet, a sample was cut from the ice and photographed. The resulting surface profiles for smooth and rough saline ice are shown in Figs. 5.1. Although good profiles were obtained, these results were still lacking in two respects: (1) only one surface profile was done for each ice sheet; and (2) the block was removed so as not to interfere with subsequent measurements; i.e., a block was cut outside of the area being studied.

During 1989, a wire gauge was used to monitor roughness. With this device it was possible to obtain many profiles within the area being studied, but, unfortunately, with reduced accuracy. Typical surface



(a)



(b)

Figure 5.1: Surface profiles for (a) smooth and (b) rough saline ice studied during the CRREL'88 experiment.

roughness profiles measured with this device are shown in Fig. 5.2a, for smooth saline ice, and in Fig. 5.2b, for desalinated ice.

We determined rms height and autocorrelations, and the corresponding uncertainties, for the surfaces observed during 1988 and 1989. The rms height we determined as

$$\sigma = \left\{ (1/N) \sum_{i=1}^N [z_i - \bar{z}]^2 \right\}^{0.5} \quad (5.1)$$

where z_i are surface height measurements at spatial intervals of about 3 mm and

$$\bar{z} = (1/N) \sum_{i=1}^N z_i$$

The autocorrelations we determined as

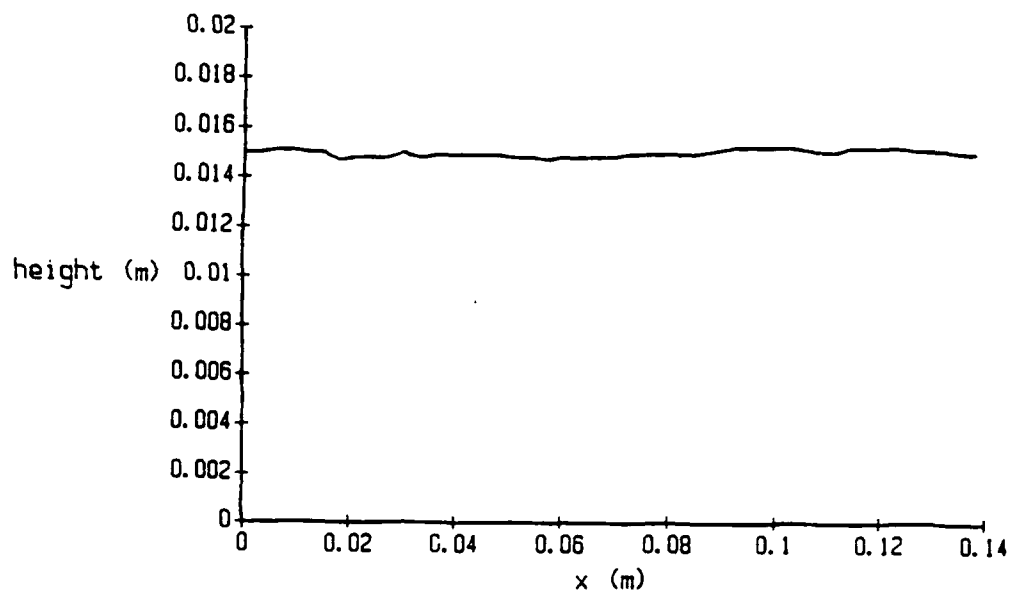
$$R_{xx_i} = (1/N) \sum_{j=1}^{N-i} [(z_j - \bar{z})(z_{j+i} - \bar{z})]$$

and normalized autocorrelations as

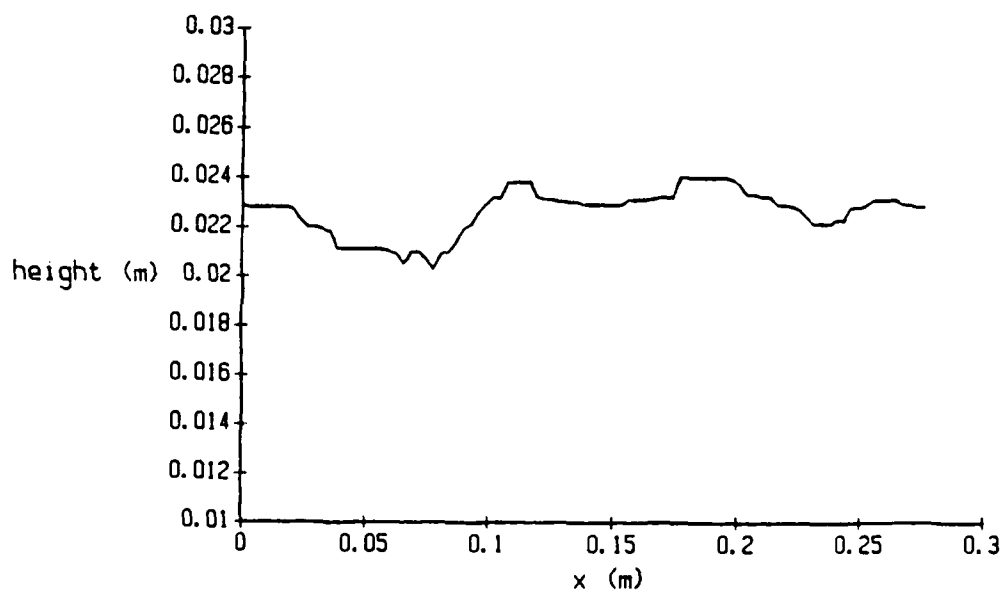
$$r_{xx_i} = R_{xx_i} / R_{xx_0}$$

$$\text{where } i = 0, 1, 2, \dots, N-1 \quad (5.2)$$

As a first approximation we fit each autocorrelation to an exponential function of the form $\exp(-x/l)$, where l is the correlation length and $l = 0.003k$, where k is the value of i corresponding to $r_{xx_i} = 1/e$. The autocorrelations and corresponding fits for the smooth saline, rough saline, and desalinated ice surfaces of 1988 are shown in Fig. 5.3 and those



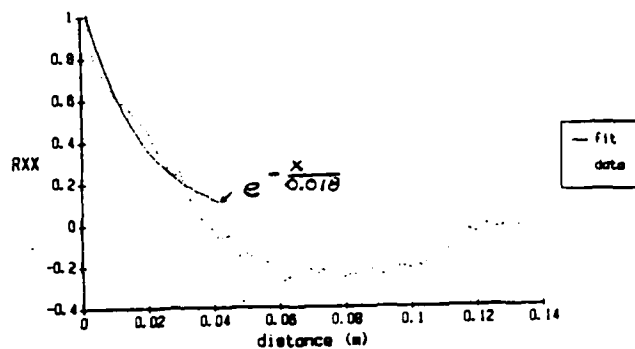
(a)



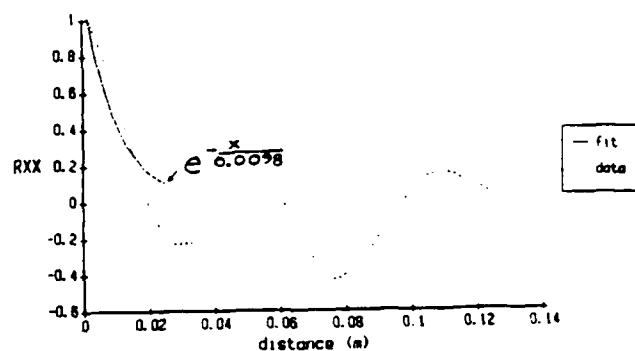
(b)

Figure 5.2: Surface profiles for (a) smooth saline ice sheet and (b) desalinated ice blocks studied during the CRREL'89 experiment.

(a)



(b)



(c)

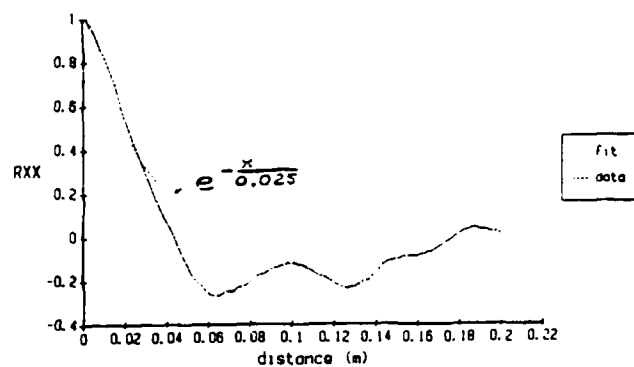
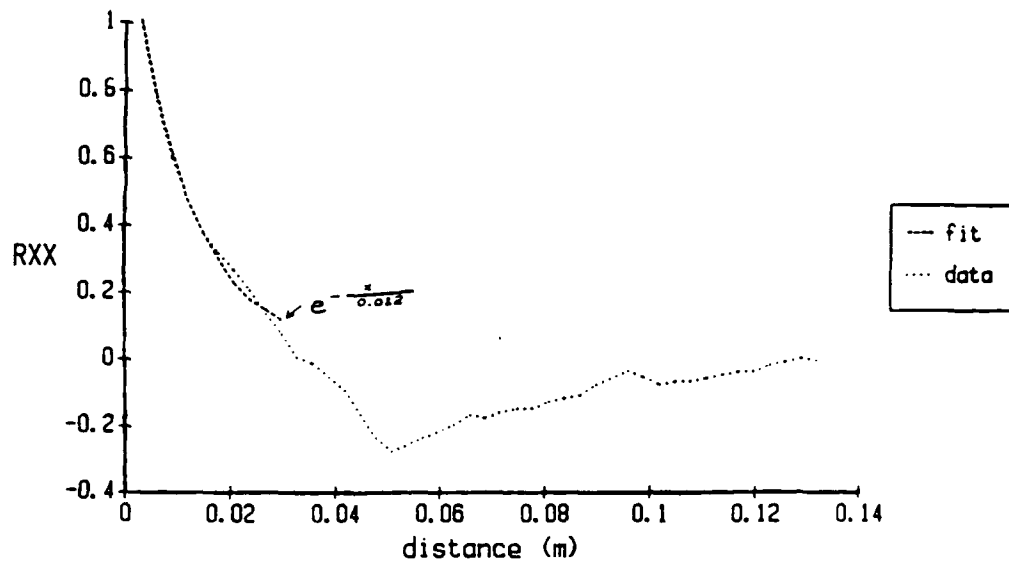
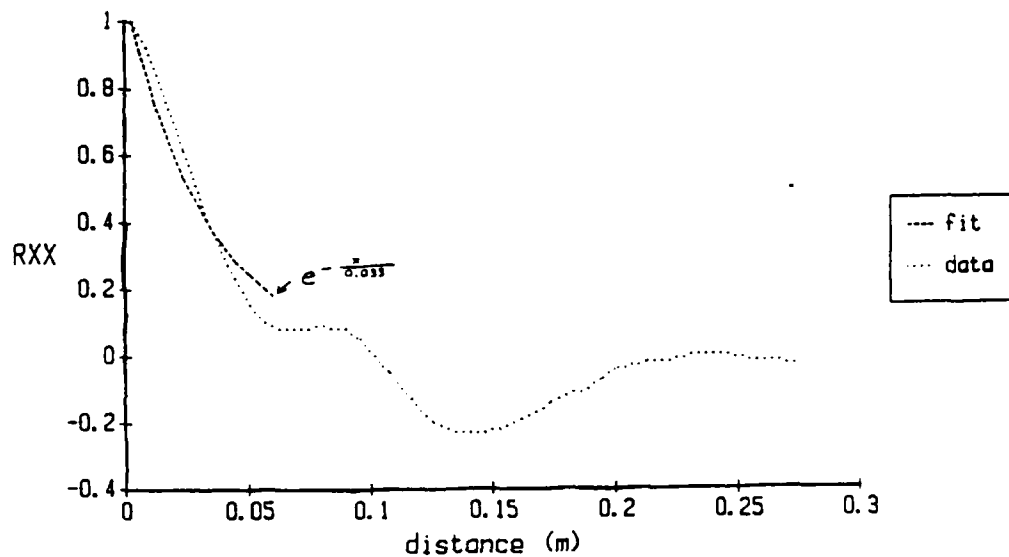


Figure 5.3: Computed autocorrelations and minimum-mean-square exponential fits for surfaces of (a) smooth saline, (b) rough saline, and (c) desalinated ice sheets studied during the CRREL'88 experiment.



(a)



(b)

Figure 5.4: Computed autocorrelations and minimum-mean-square-exponential fits for surfaces of (a) smooth saline ice sheet, and (b) desalinated ice blocks studied during the CRREL'89 experiment.

for the smooth saline and desalinated ice surfaces of 1989 are shown in Fig. 5.4. The correlation lengths for each surface are listed in Tables 3.2 and 3.3.

We then sought to determine standard deviations for the rms heights and correlation lengths, which are nonzero because of finite sample sizes, so that bounds for theoretical predictions, accounting for uncertainty (i.e., rms height ± 1 standard deviation and correlation ± 1 standard deviation) in our parameter estimates, could be obtained. Since the surface profiles of 1988 consisted of 1 profile for each surface it was not possible to obtain those statistics from the data. Hence we performed Monte Carlo simulations to obtain more profiles, making the following assumptions about the statistical distributions of the measured surface heights. We assumed that the surface height data were wide-sense stationary, gaussian distributed, and exponentially correlated, and plotted histograms of the measured data to verify that these assumptions were reasonable.

To generate samples with these statistical properties one can pass samples from a white gaussian distribution (i.e., $w(x)$) through a linear first-order system of the form

$$dz(x)/dx + Az(x) = Bw(x) \quad (5.3)$$

where A = inverse of the correlation length

B is adjusted so that $B\sigma = \text{rms surface height}$

$$\sigma^2 = E\{w^2(x)\}$$

$z(x)$ is the output.

The statistical parameters of $z(x)$ are related to the system parameters, A, B and $w(x)$ by

$$E\{z^2(x)\} = B^2 \sigma^2$$

and

$$E\{z(x)z(x+x')\} = B^2 \sigma^2 \exp(-A|x'|).$$

For convenience we implemented a discrete version of this system, i.e.,

$$z_{k+1} = Fz_k + Gw_k \quad (5.4)$$

on a personal computer. The continuous and discrete systems give approximately the same results for small spatial sampling interval, Δx , if

$$F = \exp(-A\Delta x),$$

$$G = (1/A)(1 - \exp(-A\Delta x))B, \text{ and}$$

$$w_k = w(x)/\sqrt{\Delta x} \quad (5.5)$$

[Brown, 1983].

For each surface of 1988 we simulated 20 profiles the length of the measured profile to obtain estimates of the standard deviations of the rms height and autocorrelation. Because the autocorrelations of 10 measured profiles were averaged to obtain an autocorrelation for each surface of 1989, we simulated 200 profiles the length of the measured profiles, computed the autocorrelations for each profile,

averaged them by 10's, and used the 20 averages to obtain the standard deviation limits of the autocorrelation computed from measurements. Standard deviation of the rms height was similarly computed from 20 averages of 10 rms heights.

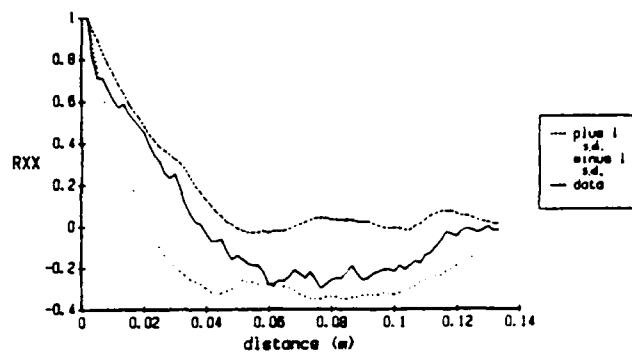
The autocorrelations and estimated ± 1 s.d. limits for each surface are shown in Fig. 5.5 for the 1988 surfaces and in Fig. 5.6 for the 1989 surfaces. Only the rough ice surface autocorrelation (Fig. 5.5b) deviates greatly from its limits, implying that it may not be exponential. As a first approximation the exponential form is considered because there are not enough data points to determine if the secondary peaks of Fig. 5.5b are statistically significant. Notice that the uncertainties for 1989 tended to be smaller than those for 1988 because more profiles were obtained for each surface in 1989.

5.2 Internal structure

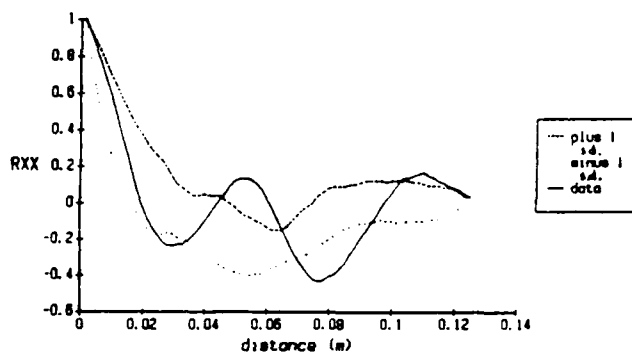
Thin section photographs of saline ice have been supplied by CRREL. In addition, during 1989, we photographed small samples and horizontal and vertical thick sections from near the top, middle and bottom of the desalinated ice blocks (See Chapter 3).

From the thick section photographs we located as many of the air bubbles as we could identify and highlighted them with a marking pen. We then made

(a)



(b)



(c)

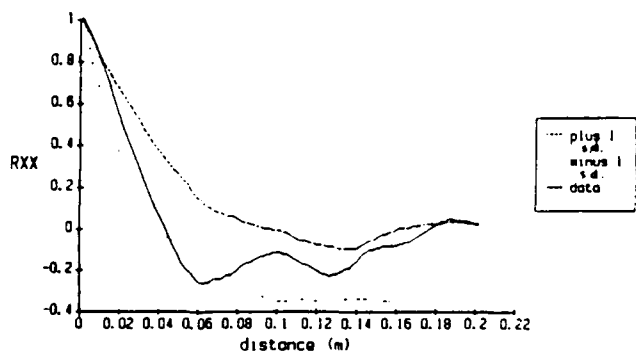
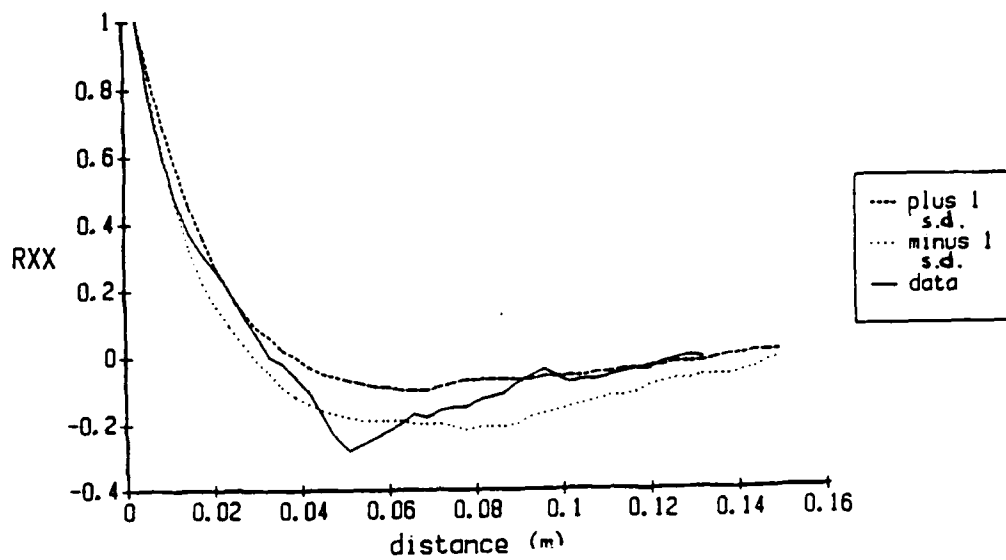
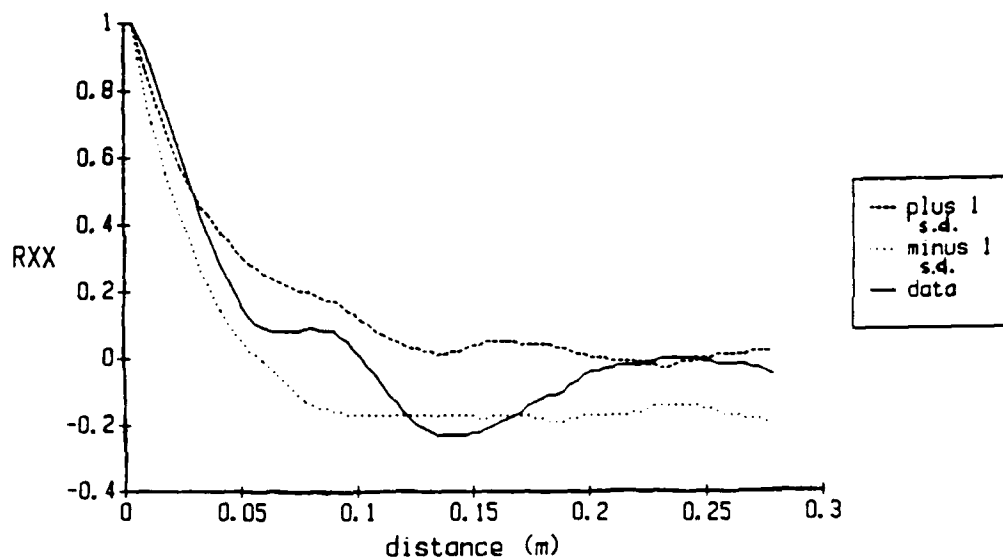


Figure 5.5: Computed autocorrelations and ± 1 standard deviation limits obtained from Monte Carlo simulations for surfaces of (a) smooth saline, (b) rough saline, and (c) desalinated ice sheets studied during the CRREL'88 experiment.



(a)



(b)

Figure 5.6: Computed autocorrelations and ± 1 standard deviation limits obtained from Monte Carlo simulations for surfaces of (a) smooth saline ice sheet, and (b) desalinated ice blocks studied during the CRREL '89 experiment.

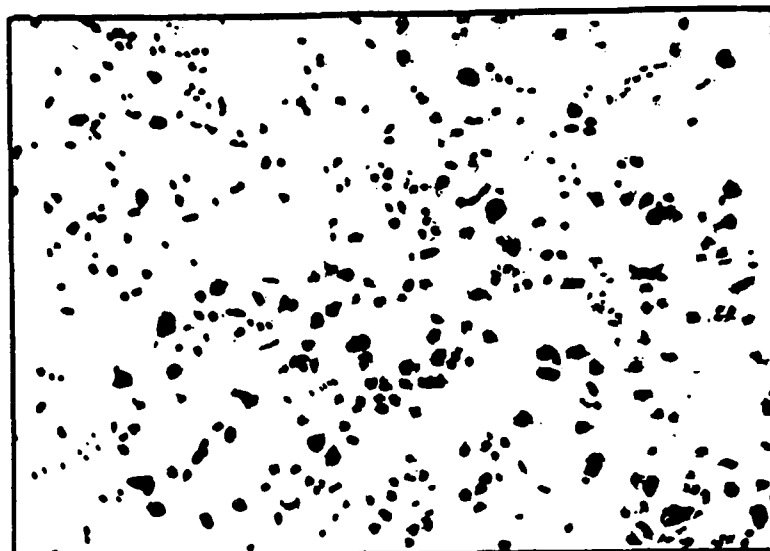


Figure 5.7: Bubbles in a 3-mm thick section taken from the top of a sample of a desalinated ice block studied during the CRREL'89 experiment, as visually identified in a thick-section photograph.

photocopies of the photographs, used white-out where necessary to eliminate the background and made more photocopies (See Fig. 5.7). We then sent these to CRREL where an image processor was used to determine correlation lengths of the spacings between air bubbles. The analysis of each processed thick section was performed assuming air bubbles were of value 1 (i.e., the relative dielectric constant of air) and the background was of value 3 (i.e., the relative dielectric constant of ice). Mean and standard

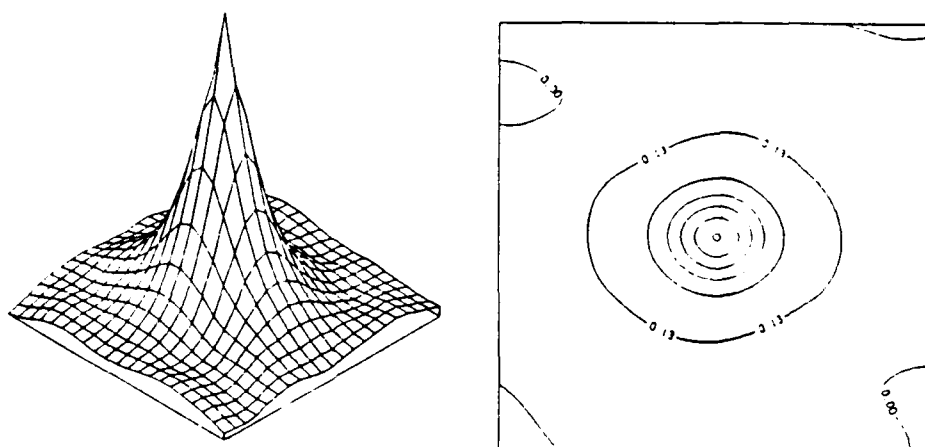
<u>Case</u>	<u>L1</u>	<u>L2</u>
Upper 3 mm horiz sect	2.00	1.77
Middle 3 mm horiz sect	2.05	2.65
Bottom 3 mm horiz sect	2.17	2.17
Upper 3 cm vertical	2.00	1.37
Middle 2 cm vertical	2.79	1.48
Bottom 2 cm vertical	4.28	2.11

L1 and L2 are correlation lengths in mm on major and minor axis of correlation ellipse.

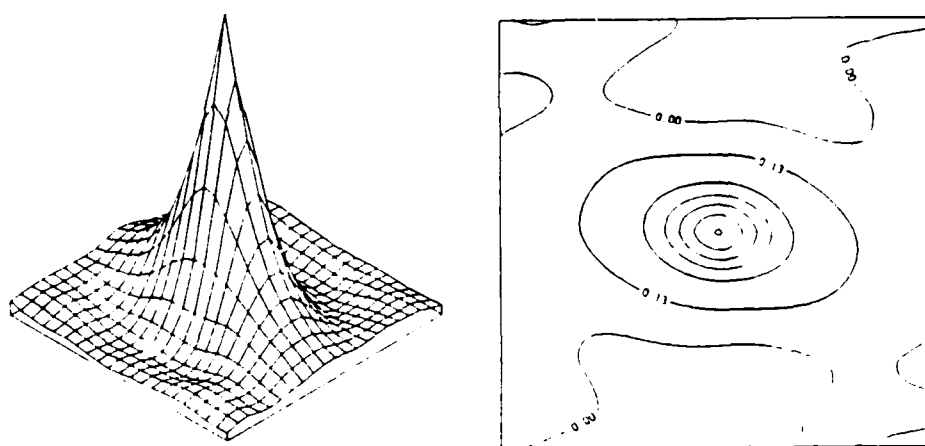
Table 5.1: Correlation lengths of air bubbles in a sample taken from a desalinate ice block studied during the CRREL'89 experiment, computed from thick-section photographs that were processed as shown in Fig. 5.7.

deviation of the image and a corresponding subimage, near the center of the image, were compared to be sure that the statistics were the same. Then the subimage was moved across the image to obtain a two-dimensional autocorrelation such as that shown in Fig. 5.8a for the upper 3 mm horizontal section and in Fig. 5.8b for the middle 2 cm vertical section (Autocorrelations of the other sections are similar to one of these two).

The correlation lengths (i.e., spacing between points along the plane of the thick section which results in a normalized autocorrelation of $1/e$) along



(a)



(b)

Figure 5.8: Autocorrelation of air bubbles in (a) a 3-mm thick horizontal section of the top and (b) 3-mm thick vertical section near the middle of a sample taken from the desalinated ice blocks studied during the CRREL'89 experiment, computed from thick-section photographs that were processed as shown in Fig. 5.7. (Courtesy of CRREL)

the major and minor axes of autocorrelation plot were then determined and are listed in Table 5.1. Notice that the correlation lengths of the horizontal sections are nearly symmetric whereas those of the vertical sections have correlation length ratios (major axis/minor axis) of 1.5 - 2, increasing with depth - a number of vertically oriented ellipsoidal bubbles in the lower half of the ice were responsible for this.

From the plots in Fig. 5.8 it seems reasonable to estimate the autocorrelation function as exponential. Simulations similar to those done for the surfaces would be informative but were not done.

A volume fraction profile of the air in the desalinated ice was estimated using measured bulk density, air bubble size distributions, and approximate bubble densities (number of bubbles/cm³). We used the air bubble distributions and bubble densities, computed from processed horizontal thick sections taken from near the top, middle and bottom of the desalinated ice, to determine a relative volume fraction profile. We then used these values and the bulk density measurement of 0.844 g/cm³, assuming the ice consisted only of pure ice and air, to determine absolute values for the volume fraction profile. The profile listed in Table 5.2 was obtained assuming that the ice consisted of three equal-size layers, with bubble distribution and

<u>Case</u>	<u>Volume fraction of air</u>
Top 4.5 cm	20.3%
Middle 4.5 cm	2.2%
Bottom 4.5 cm	0.12%

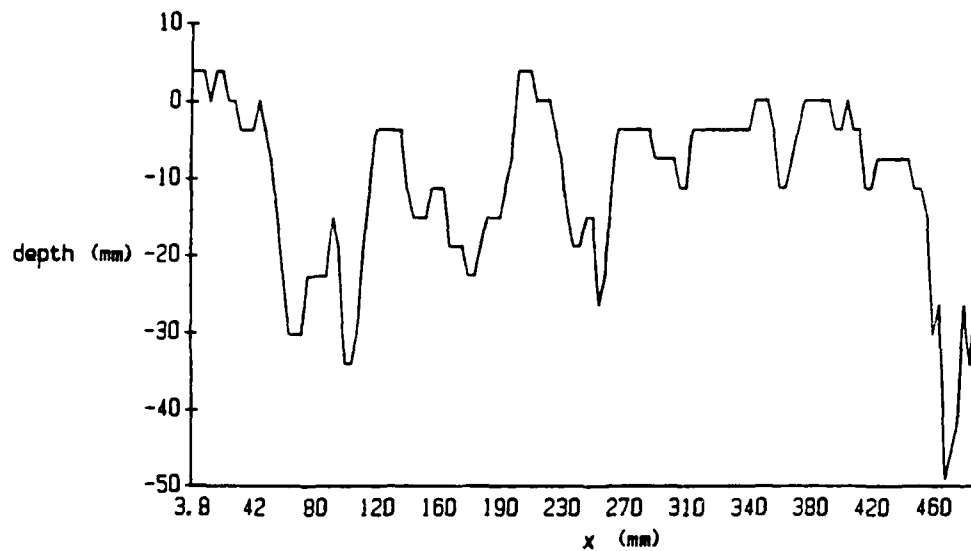
Table 5.2: Volume fraction profile of air in the desalinated ice blocks observed during the CRREL '89 experiment, computed from estimated air bubble density and size distributions, and a bulk density measurement.

density in each layer being the same as that measured for the corresponding horizontal section.

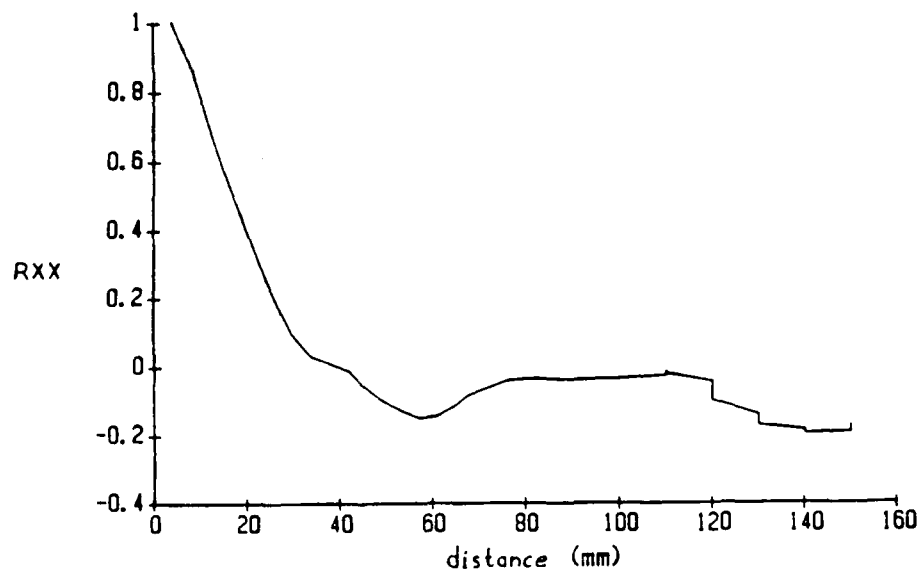
5.3 Snow cover

One useable snowfall occurred during the 1987 experiment. Unfortunately the snow parameters were not measured. One snowfall also occurred during 1989. The parameters of this snow are listed in Table 3.2.

The surface profile of the 1989 snow was estimated from a photograph. A plot of roughness and correlation function for the snow cover of 1989 are shown in Figs. 5.9.



(a)



(b)

Figure 5.9: (a) roughness and (b) computed autocorrelation of the surface of the snow covering the saline ice sheet on Feb. 3, 1989.

6.0 Data Analysis and comparison with theory

We used an analog spectrum analyzer to convert the SOURCESCAT output signal into a more useable range-discriminated form (frequency domain). For PAIR and STEFRAD a Discrete Fourier Transform (DFT) program performed the same function. Note that the output of STEFRAD is equivalent to the time domain outputs of SOURCESCAT and PAIR - see Chapter 4 for a discussion of point target returns for each of the radars.

The BASIC routines we used to study and process the SOURCESCAT data were slow and relatively inflexible, so we wrote a comprehensive data analysis program in TURBO Pascal to study and process PAIR and STEFRAD data. The most important components of our data analysis software are: (1) a flexible CRT graphics display routine; (2) an efficient FFT algorithm; and (3) an accurate integration routine. Other important components of our software include routines to subtract system response, unwrap phase, and determine phase differences. This package enabled us to study amplitude and phase of the return signal, in both the time and frequency domains, and to integrate over selected intervals.

6.1 Computation of σ^0

In determining σ^0 , it is necessary to compute the total power returned from the target. Total target

power is obtained by integrating over the appropriate segment of the range-discriminated signal (i.e., frequency domain). (Note that range discrimination is necessary even in the apparent absence of other targets due to radar system reflections and feedthroughs as shown in Figs. 6.1). The integration for SOURCESCAT was performed as

$$P = \sum_{i=m}^n P(\omega_i) \quad (6.1)$$

where $P(\omega_i)$ = power density at frequency ω_i as obtained from the analog spectrum analyzer

ω_m = low frequency limit of target return

ω_n = high frequency limit of target return

The integration for PAIR and STEFRAD was performed as

$$P = \sum_{i=m}^n X(\omega_i) X^*(\omega_i) = \sum_{i=m}^n |X(\omega_i)|^2 \quad (6.2)$$

where $X(\omega)$ is the DFT of the radar output and ω_m and ω_n are defined above.

Once total power values were obtained, standard narrow-beam techniques were used to obtain σ^0 ; i.e.,

$$P_{r,t} \approx CP_t G_t A_e \sigma^0 A / (4\pi)^2 R^4 \quad (6.3)$$

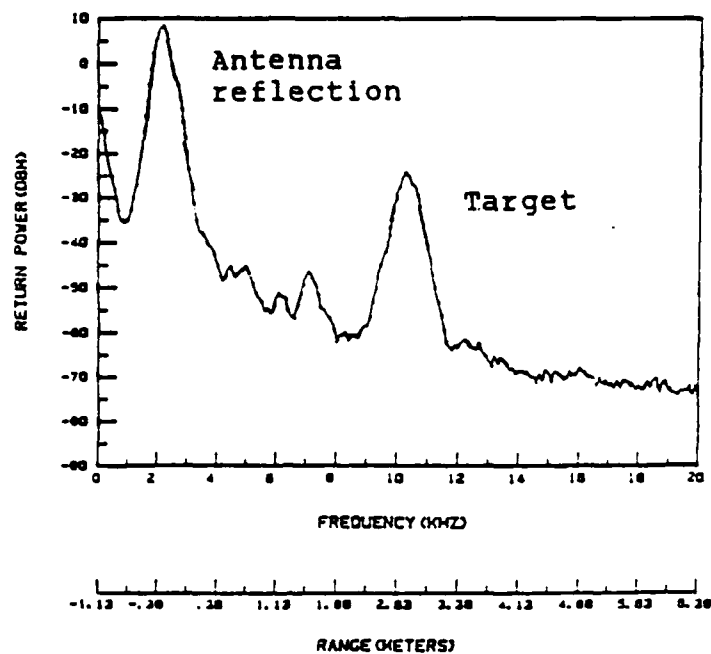
where $P_{r,t}$ = total return power from target

P_t = transmitted power

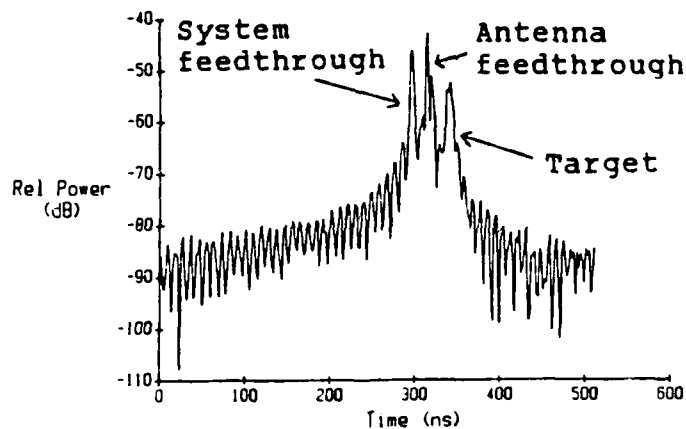
G_t = antenna gain

A_e = antenna effective aperture

σ^0 = characteristic cross-section of target



(a)



(b)

Figure 6.1: Returns from target and system as seen in range-discriminated outputs of (a) X-band SOURCESCAT (b) Ku-band STEFRAD.

A = illuminated area of target
 R = slant range to the target
 C = constant to account for system parameters
not in radar equation; e.g., system
transfer functions and loss

Since many of these parameters were not accurately known, measurements of an internal reference (delay line) were used to monitor system changes to allow comparing target returns with return from a target of known cross-section, σ . Let

$$\begin{aligned}
P_{DLt} &= K_2 K_t L \quad \text{and} \\
P_{rt} &= K_1 K_t \sigma^0 A / R_t^4, \quad (6.4)
\end{aligned}$$

assuming K_t does not change from target measurement to delay line reading, and

where P_{rt} is defined above and

P_{DLt} = delay line return power at the time of target measurement

K_1, K_2 = transfer functions of stable system paths of radar in radar mode and delay-line mode respectively

K_t = transfer function of time- and temperature-varying system path at time of target measurement

L = delay line loss

R_t = slant range to the target

Also let

$P_{DLc} = K_2 K_c L$ and

$$P_{rc} = K_1 K_c \sigma / R_c^4, \quad (6.5)$$

assuming K_c does not change from calibration measurement to delay line reading. K_1, K_2 , and L are defined above and

P_{DLc} = delay line power at the time of calibration measurement

P_{rc} = power return from known target

K_c = transfer function of time- and temperature-varying system path at time of calibration measurement

R_c = slant range to calibration target

σ = cross-section of known target.

then σ° can be related to σ via a series of ratios.

$$\begin{aligned} P_{rt} / P_{rc} &= (K_t / K_c) (\sigma^\circ A / \sigma) (R_c^4 / R_t^4) \\ &= (P_{DLt} / P_{DLc}) (\sigma^\circ A / \sigma) (R_c^4 / R_t^4) \end{aligned}$$

and

$$\sigma^\circ = (P_{rt} / P_{rc}) (P_{DLc} / P_{DLt}) (\sigma / A) (R_t^4 / R_c^4) \quad (6.6)$$

Once narrow-beam values were obtained, a routine by Kim [1982] was used to determine if σ° variation within the beam was sufficiently small so that the narrow-beam approximation was valid. In addition, a routine by Wang [1989] was used to make necessary corrections for antenna separation.

6.1.1 Consideration of errors

The calibration targets used were 8" and 12"

Luneberg lenses, a diplane constructed of 2 10"x10" metal plates, and an active radar calibrator. Returns from the diplane ($\sigma = 4\pi A_{\text{eff}}^2 / \lambda^2 = 16.2$ dB at C band and 23.3 dB at Ku band) were used to verify the predicted cross-section of the 8" Luneberg lens (1 to 2 dB less than $4\pi^3 r^4 / \lambda^2$, or 6 dB at C-band and 12 dB at Ku band). The predicted cross-section of the 12" Luneberg lens (1 or 2 dB less than $4\pi^3 r^4 / \lambda^2$, or 17 dB) was not properly verified - this is not crucial to the discussion to follow in that only a qualitative description of the data depending on calibration with this lens is given (i.e., the CRREL'87 data).

The calibration measurements of the 1988-1989 experiment were done with the 8" Luneberg lens and are accurate to within about ± 1 dB, assuming a calibration range uncertainty of ± 10 cm and allowing for a few tenths of a dB uncertainty to account for pointing error between the antenna and lens. The calibration measurements of the 1986-1987 experiment were done with the 12" lens and are, somewhat arbitrarily, assigned an uncertainty of ± 2 dB to allow for uncertainty in the 12" lens cross-section. The C-band calibrations of the 1987-1988 experiment were done with the 8" Luneberg lens and have a somewhat wider uncertainty than those of the other 2 experiments (i.e., ± 3 dB) because we later discovered that a Luneberg lens is not a suitable

calibration target for a system with a bistatic angle between transmit and receive antennas (See Fig. 6.2). The lens beamwidth at C band is about twice that shown in Fig. 6.2 since the measurements shown in the curve were done at X band; thus our calibration readings would have been about 5 dB below the peak return of the lens. The uncertainty was estimated to be ± 3 dB to allow for uncertainty in the bistatic angle - notice the steepness of the curve in the vicinity of -5 dB.

Other uncertainties, including target range and error due to use of the narrow-beam approximation, account for a maximum error of ± 1 dB. These uncertainties are referred to as target measurement uncertainty in the following discussion.

Another consideration in estimating σ^0 is uncertainty due to fading - because the number of data points obtained in each case is too small to be used to estimate the actual distribution, a typical exponential distribution is assumed. During the 1987 campaign we obtained a minimum of 10 uncorrelated samples for each measurement. Assuming Rayleigh fading $1 \pm \mu/\sigma = 1.19$, -1.65 dB. During the 1988 and 1989 campaigns we were able to obtain only 5 uncorrelated samples, in most instances, and 3 in some cases. Assuming an exponential distribution, $1 \pm \mu/\sigma = 1.6$, -2.7 dB for 5 uncorrelated samples and $= 2.0$, -3.74 dB for 3 uncorrelated samples.

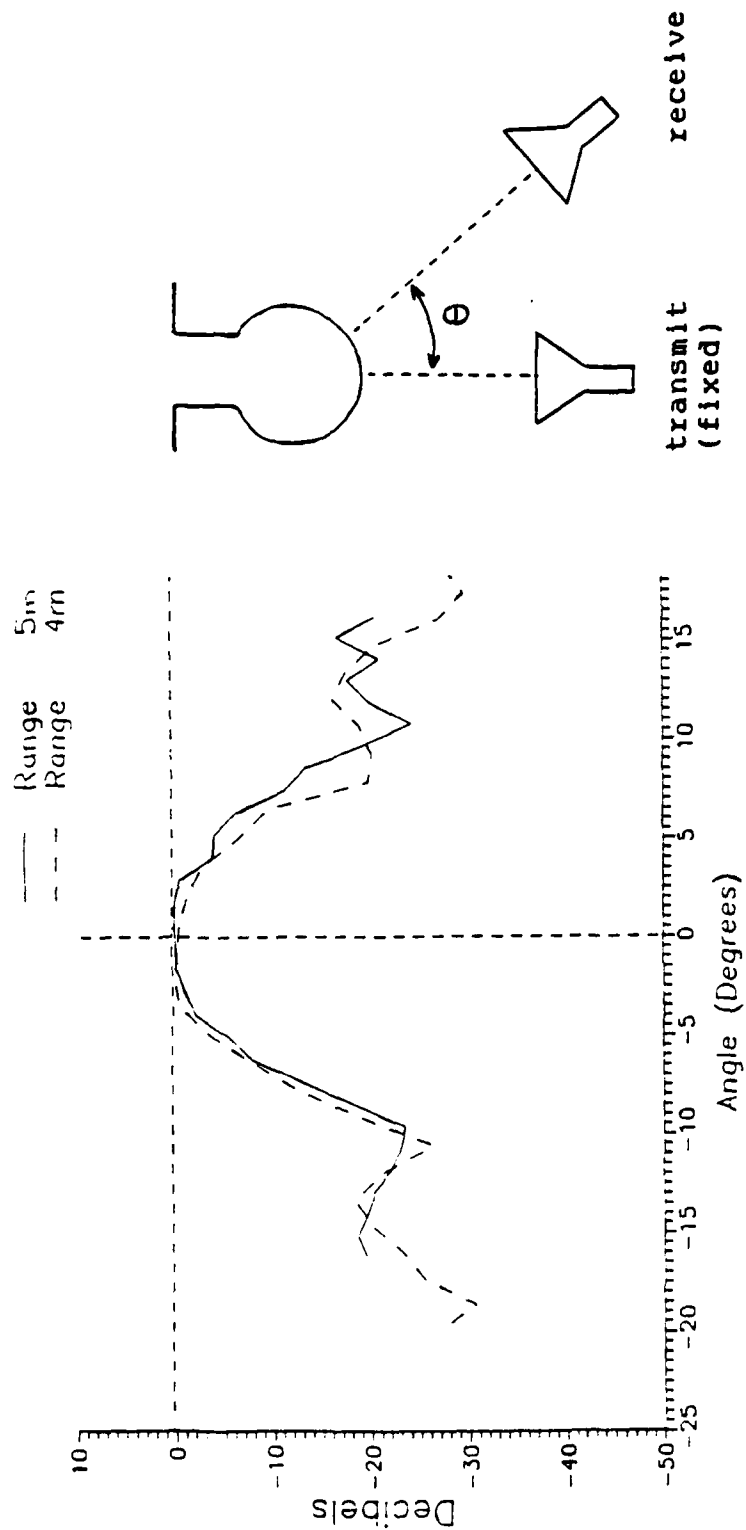


Figure 6.2: Relative power return at X band from an 8" Luneberg lens as the bistatic angle, θ , is varied (courtesy of P. Racette and R. Forster [1989]).

To consider the combined effect of calibration and target measurement uncertainties and fading on σ^0 , we express equation (6.6) in the form

$$\sigma^0 = kFP_{rt}\sigma \quad (6.7)$$

where k = constant

F = factor to account for target measurement uncertainty

P_{rt} = return power obtained from a average of a designated number of independent samples

σ = lens cross section.

We then make the assumption that F , P_{rt} and σ are statistical parameters with F accounting for target measurement uncertainty, P_{rt} accounting for fading, and σ accounting for calibration uncertainty. The combined uncertainty can then be estimated by expanding $10\log(\sigma^0)$ in a Taylor series around μ_F , $\mu_{P_{rt}}$ and μ_σ and taking expected values. From Breipohl [1970]:

If $Y = g(X_1, X_2, \dots, X_n)$ and $\mu_i = E[X_i]$ then

$$Y \approx g(\mu_1, \mu_2, \dots, \mu_n) + \sum_{i=1}^n \left[\frac{\partial g(\mu_1, \mu_2, \dots, \mu_n)}{\partial X_i} \right] (X_i - \mu_i)$$

and

$$\sigma_Y^2 \approx \sum_{i=1}^n \left[\frac{\partial g(\mu_1, \mu_2, \dots, \mu_n)}{\partial X_i} \right]^2 \sigma_i^2 \quad (F, P_{rt}, \sigma \text{ independent})$$

(6.8)

So if

$$10\log(\sigma^0) = 10\log(k) + 10\log(F) + 10\log(P_{rt}) + 10\log(\sigma)$$

then

$$\sigma_y^2 = (10\log(e))^2 [(\sigma_F/\mu_F)^2 + (\sigma_\sigma/\mu_\sigma)^2 + (\sigma_{P_{rt}}/\mu_{P_{rt}})^2]$$

(in dB)

The estimated total uncertainty values were obtained as $\pm\sigma$ and are listed in Table 6.1. They are also included on plots containing measured data points as vertical bars.

	uncertainty target		Fading	Total
	cal.	meas.	uncertainty	uncertainty
1987				
all surfaces	± 2	± 1	-1.7, +1.2	± 3
1988				
smooth	± 3	± 1	-2.7, 1.6	± 4.9
saline ice				
rough saline	± 3	± 1	-1.7, 1.2	± 4.7
ice				
desalinated	± 3	± 1	-2.7, 1.6	± 4.9
ice				
1989				
smooth and	± 1	± 1	-2.7, 1.6	± 2.5
snow covered				
smooth saline				
ice				
desalinated	± 1	± 1	-3.7, 2	± 3
ice blocks				

Table 6.1: Estimated measurement and fading uncertainty (in dB) for the three years of experiments.

6.2 Results

In this section, the processed data are presented.

In particular we treat the effects of surface roughness, snow cover, and volume inhomogeneities. The Kirchhoff scalar approximation and Small Perturbation Method surface scatter models and the Effective Medium volume scatter theory (see Chapter 2) are used in the comparisons between results and theoretical predictions.

6.2.1 Smooth saline ice

Backscatter from smooth saline ice at X band (on Jan. 17, 1987) is illustrated in Fig. 6.3. Notice that σ_{VV}^0 and σ_{HH}^0 are not statistically different. We determined the penetration depth of the ice to determine if measurable volume backscatter was possible and used the Kirchhoff surface-scatter model, with estimated surface parameters as inputs, to determine if surface scatter alone could account for our results.

We determined the penetration depth from estimates of the ice dielectric constant, using the model of Frankenstein and Garner [1967] with the salinity profile of Fig. 3.5, and assumed linear temperature variation as a function of ice depth (-15°C , or air temperature, at the surface to near 0°C at the water surface). Returns from the ice-water interface (at 6 cm depth) were negligible, since they were attenuated by more than 12 dB. Other contributions from within the ice were not ruled out; e.g. return from the

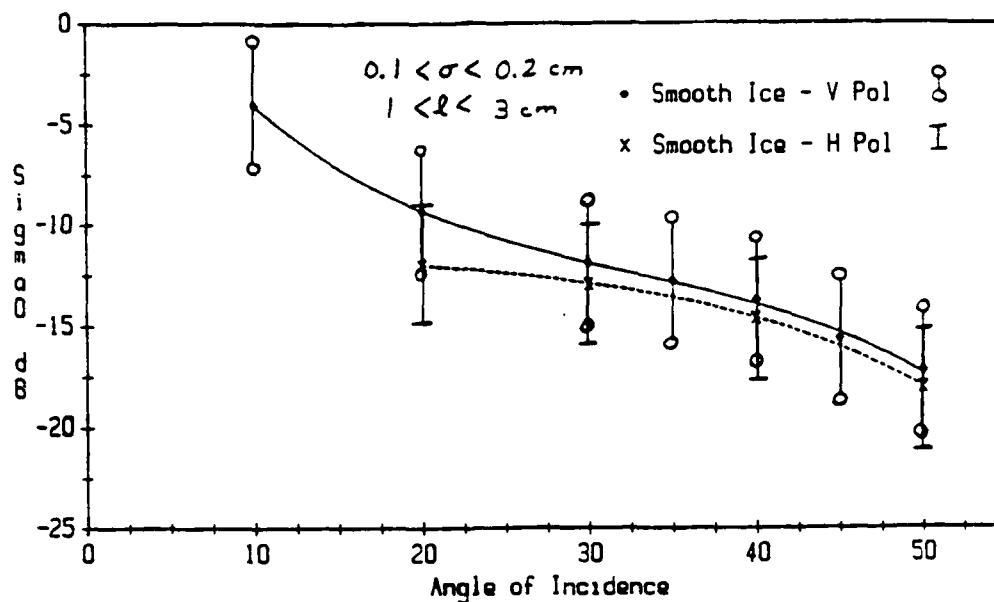


Figure 6.3: Backscatter cross-section of smooth (i.e., rms height < 0.1 cm) saline ice sheet at X band, as determined from data obtained during the CRREL'87 experiment.

interface between the more granular and less granular ice at a depth of about 3 cm (see Fig. 3.4).

We used the estimated rms surface height and adjusted values of the correlation length in the Kirchhoff surface scatter model. By adjusting the correlation length (to a reasonable value) we were able to obtain predicted values that were within a few dB of the measured data.

The range-discriminated radar output data from which Fig. 6.3 is derived showed that the returns from

the surface were broader than would be expected for surface scatter only. We performed a simulation to show that this broadening may have been due to a small volume scatter component. The point target return is contrasted to the ice surface return in Fig. 6.4a, where the footprint on the ice surface was approximately a circle of 12" radius. To simulate the broadening effect (See Fig. 6.4b) we assumed that σ^0 at 50° incidence was due solely to volume scatter, that the narrow-beam approximation was valid, and that the volume scattering coefficient, σ_v , was constant such that (from Ulaby et al., [1982])

$$\sigma^0(50^\circ) = \sigma_v^0(50^\circ) = \{T^2(50^\circ) \int_0^\infty \sigma_v \exp(-2\alpha z) dz\} \cos\theta' \quad (6.9)$$

where α = power absorption coefficient of the ice
calculated using the estimate dielectric
constant

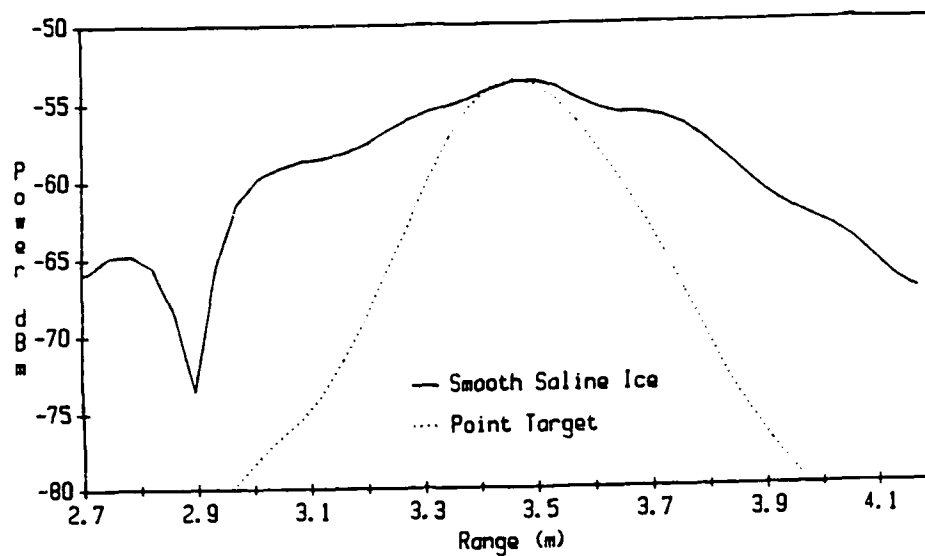
z = distance of penetration into the ice

T = transmission coefficient at air-ice interface
assuming a smooth interface

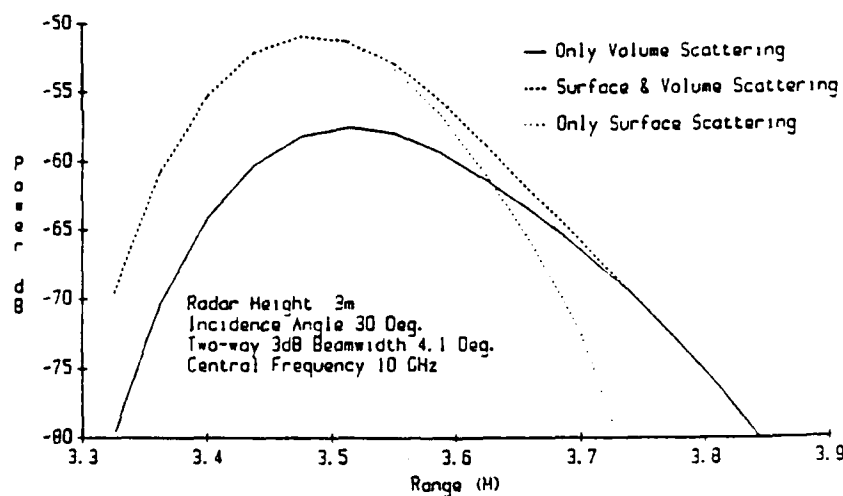
θ' = angle of refraction in saline ice

σ_v^0 = volume scatter contribution to σ^0

We then divided the simulated target into range cells, determined the surface and volume contributions from each range cell to $\sigma^0(30^\circ) = \sigma_s^0(30^\circ) + \sigma_v^0(30^\circ)$, using $\sigma^0(30^\circ)$ obtained from measurements and equation (6.9) to determine σ_v^0 . This information, the known slant



(a)



(b)

Figure 6.4: (a) measured backscatter from artificially grown sea ice at X band and 30 degrees incidence, contrasted with point target return (b) simulation of relative contributions of surface and volume scatter to backscatter from artificially grown sea ice at X band and 30 degrees incidence.

range, illuminated area and antenna beamwidth were used into the radar equation to calculate the return power as a function of range.

We concluded that the return from this ice surface was dominated by surface scatter but that a small volume-scattering component was probably present.

The ice structure and dielectric profile on Jan. 21, 1987 were nearly the same as they were on Jan. 17. The major differences in the ice sheet were a 6 cm increase in thickness and a modified roughness. The comments concerning volume scatter made for the sheet of Jan. 17 are applicable here. We again assumed that surface scatter dominated the return due to the relatively high absorption of the ice. We used the Small Perturbation Model with the estimated rms height and a correlation length adjusted to achieve a best fit with the data (see Fig. 6.5). Notice how the slope of the $\sigma^0(\theta)$ curves, especially the HH curve, differed from those of Jan. 17 (Fig. 6.3).

According to the Small Perturbation Method, the change in backscatter as a function of incidence angle that occurred from Jan. 17 to Jan. 21 can be explained by a change in correlation length (Figure 6.6a illustrates the effect) and a slight change in rms height (See Fig. 6.6b), or by a change in correlation function. The latter possibility cannot be ruled out

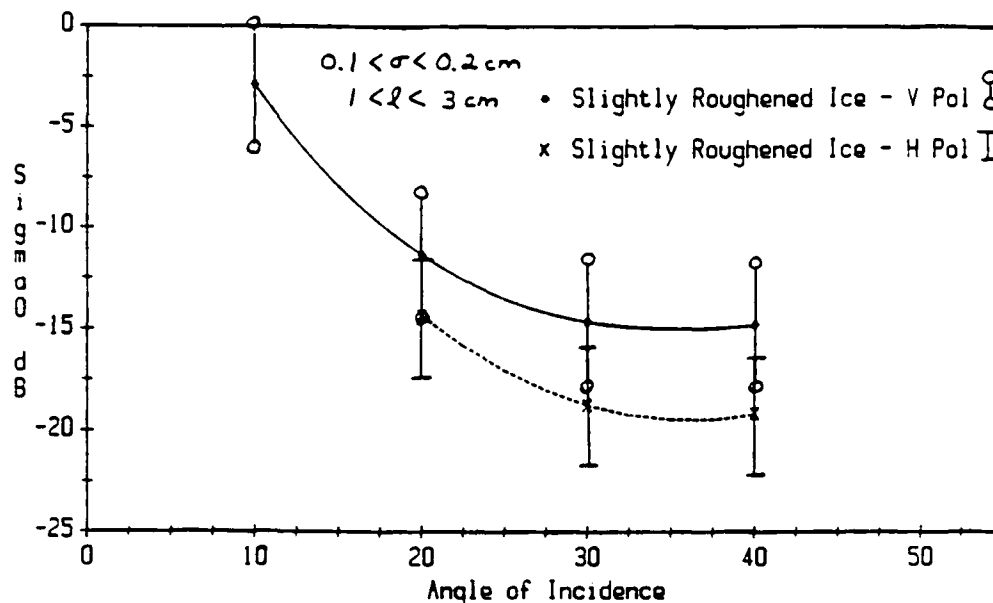
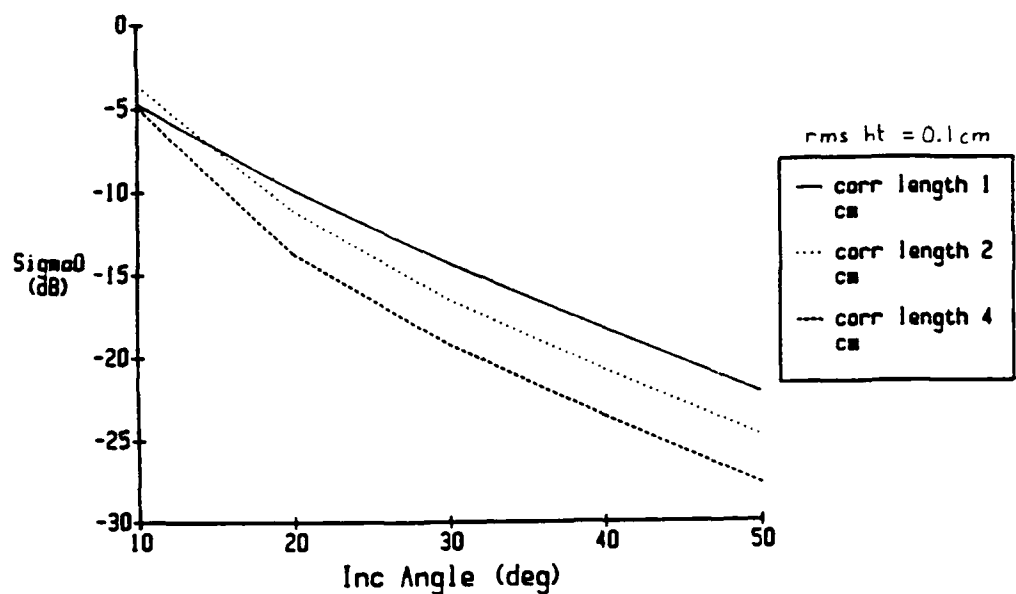


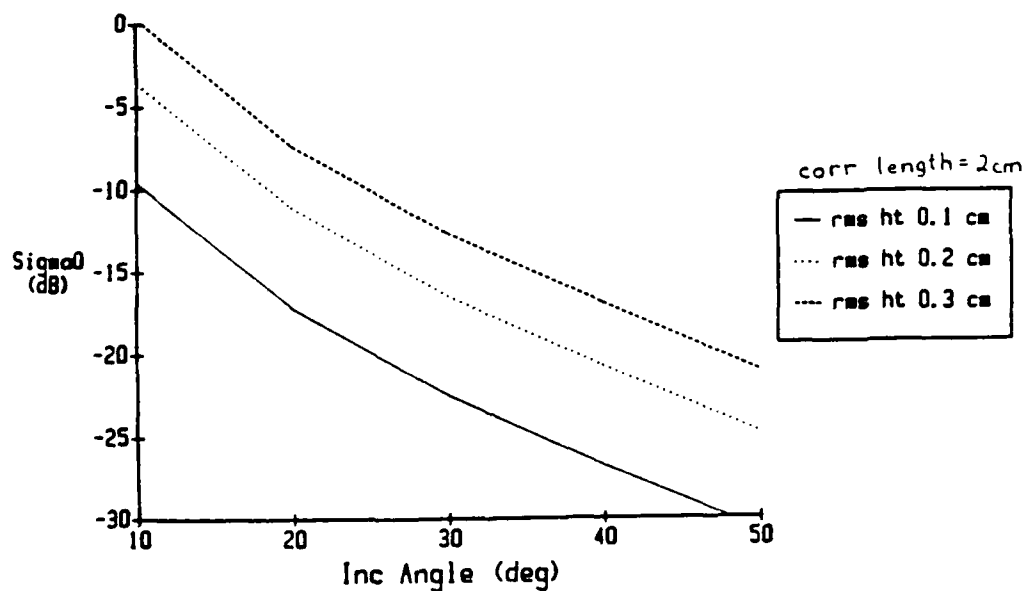
Figure 6.5: Backscatter cross-section of textured saline ice sheet at X band, as determined from data obtained during the CRREL'87 experiment.

since we textured the ice. The observed difference between VV and HH polarizations in Fig. 6.5 is predicted by the Small Perturbation Method. The change in this difference between Jan. 17 and Jan. 21 cannot be. With the first-order Small Perturbation Method, only a change in dielectric constant can change the difference between VV and HH, and the effect is small (tenths of a dB as ϵ' changes from 2.5 to 4).

Backscatter from a smooth saline ice sheet at C band (Feb. 3, 1989) is shown in Fig. 6.7. The 2



(a)



(b)

Figure 6.6: Effect of variation in (a) correlation length and (b) rms height on predictions of the Small Perturbation Method at X band.

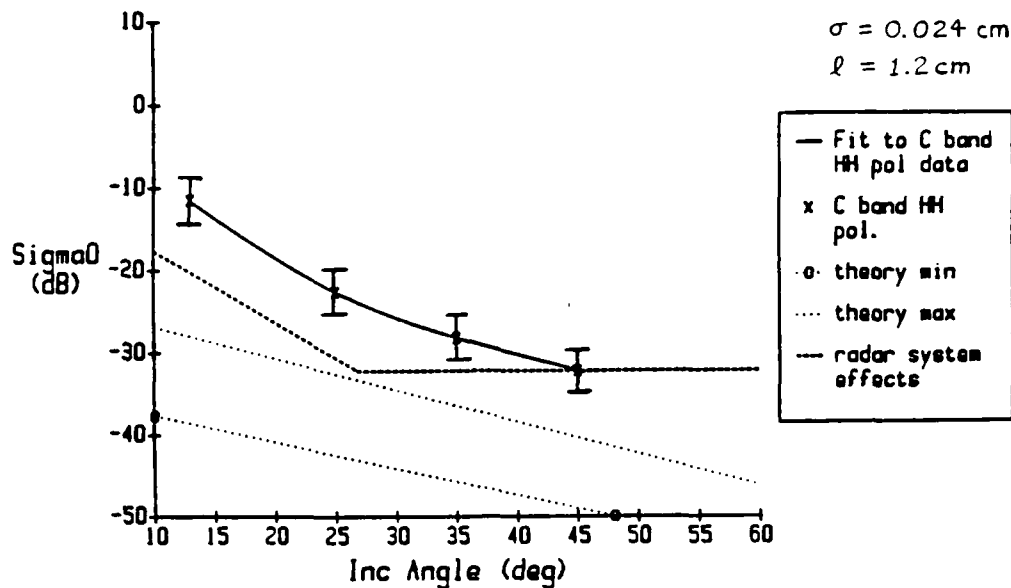


Figure 6.7: Backscatter cross-section of smooth saline ice sheet at C band, as determined from data obtained during the CRREL'89 experiment, compared with Small Perturbation Method predictions.

dotted curves indicate the maximum and minimum Small Perturbation predictions of $\sigma_0(\theta)$ based on the rms height ± 1 standard deviation and the correlation length ± 1 standard deviation of the surface. The dashed line indicates the noise level of the STEFRAD radar. Notice that this radar is incapable of measuring the predicted return.

The discrepancy between measurement and theory can be attributed to volume scattering, radar system effects, and uncertainty in surface characterization.

To illustrate the volume scattering effect, consider the volume scattering component as an equivalent rough surface - this has some merit in light of the abrupt change in dielectric constant at depths of 2-4 cm observed for Feb. 3, 1989 (see Fig. 3.20a). Assuming the proposed model σ^o is computed as

$$\sigma^o = T^2 (\sigma_{\text{equiv surface}}^o * \exp(-2\alpha d \sec \theta')) + \sigma_{\text{ice}}^o \quad (6.10)$$

where α = power absorption coefficient of the ice calculated using the estimated dielectric constant

T = the air-ice transmission coefficient assuming a smooth interface

σ = the power absorption coefficient determined from the estimate dielectric constant

d = the depth of the equivalent surface in the ice

θ' = angle of refraction in saline ice

σ_{ice}^o = radar cross-section of the ice surface determined from the Small Perturbation Method

$\sigma_{\text{equiv surface}}^o$ = radar cross-section of the equivalent surface determined from the Small Perturbation Method

The application of this model to the saline ice sheet of Fig. 6.7 is illustrated in Fig. 6.8, with equivalent rough surface parameters of $\epsilon'_f = \epsilon'_{\text{med } 2}$, $\epsilon'_{\text{med } 1} = 1.2$, $\sigma_{\text{rms}} = 0.5$ cm, and $l = 1.8$ cm. Notice that this model can account for the level of most of the data points.

Radar system effects are shown in Fig. 6.7 and

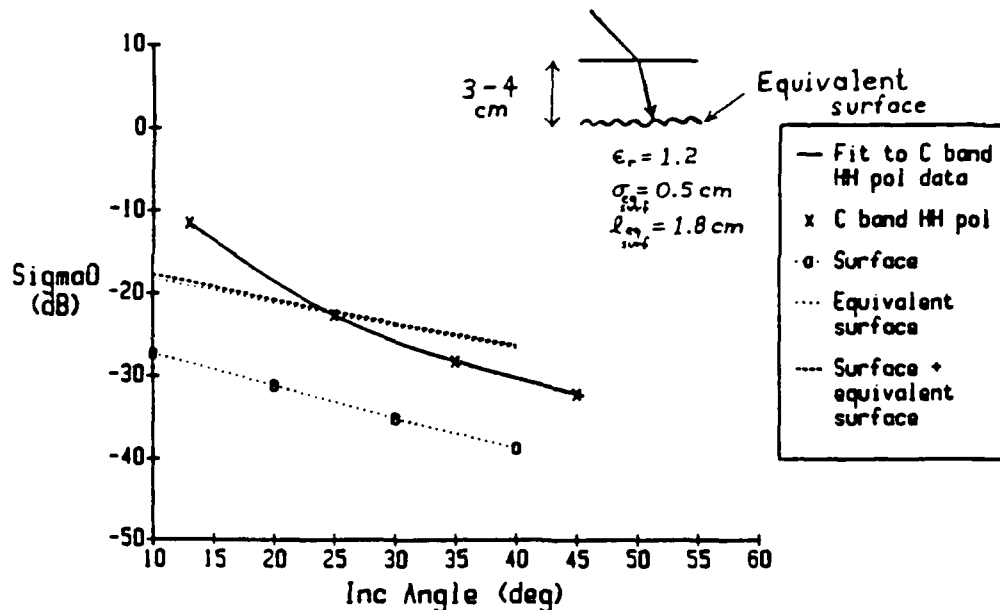


Figure 6.8: Backscatter cross-section of smooth saline ice sheet at C band, as determined from data obtained during the CRREL'89 experiment, compared with predictions of a simple layer model.

include system noise and coherent contributions due to the wide beamwidth of the antennas. As can be observed, these effects are still several dB below the measured values.

Uncertainties due to the statistical nature of the ice surface were discussed in Chapter 5. Uncertainty in surface roughness measurements contributes a less well-characterizeable uncertainty that can be large for smooth surfaces. For example, from the photograph we used to determine roughness for one of the 1988 ice

sheets, another group determined a σ_{rms} value 15% higher than our $\sigma_{rms} + 1$ standard deviation. But even their estimates give theoretical predictions that are about 6 dB lower than what we measured.

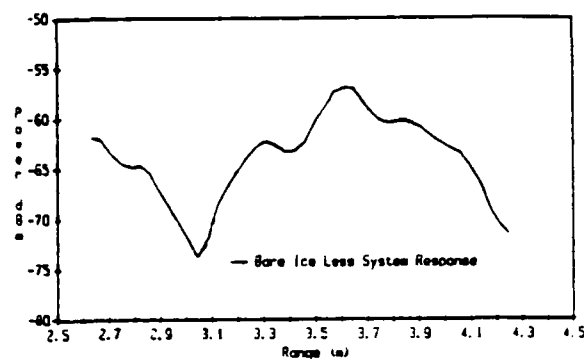
We conclude that volume scatter contributes measurably to backscatter from smooth saline ice at C band. We have not been able to quantify the effect however.

6.2.2 Snow cover effects

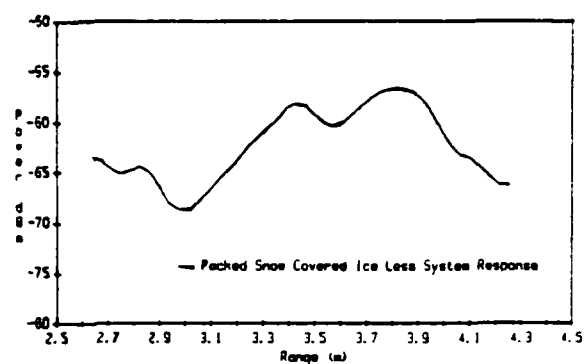
We noticed that a deep layer of snow (15 cm) caused considerable volume scatter at X band; an isolated experiment was done to illustrate this. With no snow, a dominant peak corresponding to the ice surface was observed (Fig. 6.9a). After 15 cm of loose snow was piled on the ice surface a relatively broad spectral return was observed (Fig. 6.9b). This was indicative of volume scatter from the snow particles in the air-snow mixture (the snow was dry and the temperature was about -9°C). Then the snow was packed to a depth of 7.5 cm and more measurements were done. The packing increased the homogeneity of the layer, as evidenced by the decrease in spectral broadening; because of the decrease in volume scatter peaks corresponding to the snow and ice surfaces became noticeable (Fig. 6.9c).

At X band 6.5 cm of dry snow had little effect on

(a)



(b)



(c)

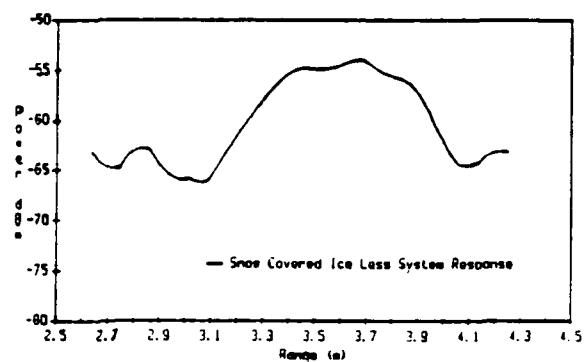


Figure 6.9: Effect of snow cover as seen in range-discriminated output of X-band SOURCESCAT during the CRREL'87 experiment. (a) return from bare smooth saline ice surface - peak at slant range of about 3.6m corresponds to surface, (b) broadening effect caused by volume scatter within 15-cm snow cover, and (c) return after 15 cm of loose snow packed to thickness of 7.5cm - peak at 3.4m corresponds to snow surface and peak at 3.8m corresponds to ice surface.

σ^0 , as was determined during the 1987 campaign. No significant contribution from the snow cover was evident at either polarization (See Figs. 6.10). The properties of the snow covering the surface are not known, except that the snow was dry. Assuming that the snow was of density 0.2 g/cu cm (i.e., $\rho_s = 0.2$), and using the empirically-determined expressions of Ulaby et al [1982], which relate extinction coefficient and volume scattering coefficient to snow density at 9 GHz (i.e., $k_e = 0.77\rho_s$ and $\sigma_v = 0.4\rho_s$), the volume scatter contribution of the snow is estimated from

$$\sigma_{ds}^0 = (\sigma_v \cos\theta / 2k_e) (1 - 1/L^2(\theta)) \quad (6.11)$$

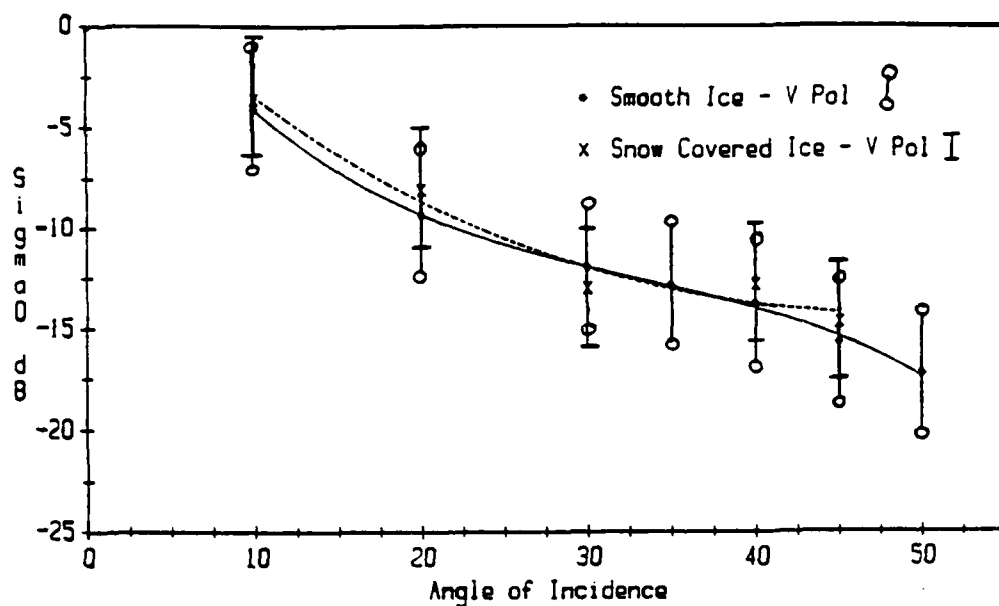
where k_e = extinction coefficient

$L(\theta)$ = loss of the snow layer at incidence angle θ

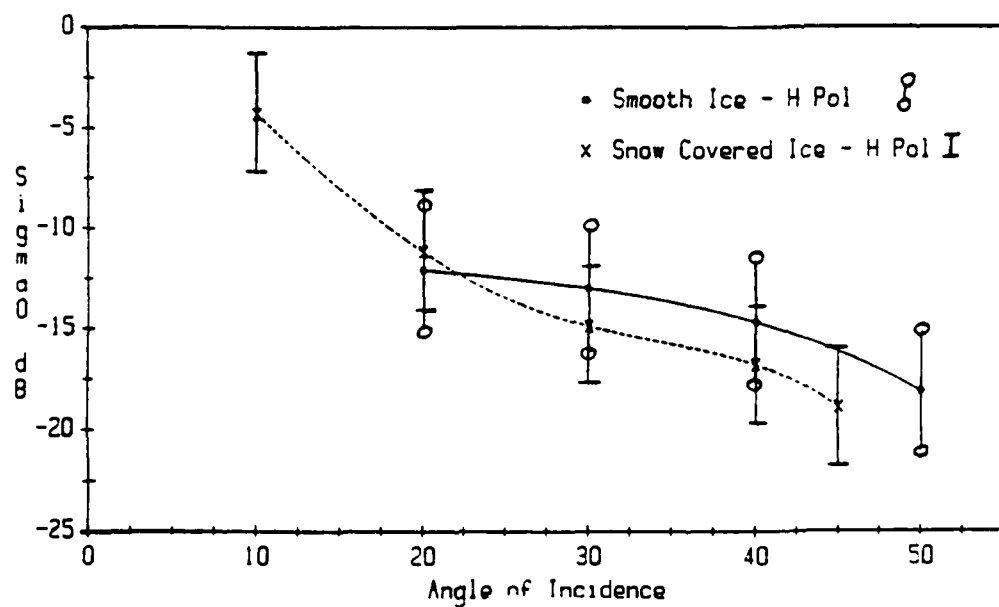
k_e , σ_v are defined above

to be approximately -24 dB. Since this is 6 to 8 dB lower than bare ice $\sigma(\theta)$, it is not surprising that no significant contribution from the snow was evident. That is, the ice surface was sufficiently rough (see parameters in Fig. 6.3) that surface scatter dominated over volume scatter from the snow.

During 1989 we studied an ice sheet (at C band) that was sufficiently smooth that volume scatter from a 6.5 cm snow cover dominated the return at larger incidence angles. At incidence angles greater than 25° an increase of up to 7 dB in σ^0 was observed.



(a)



(b)

Figure 6.10: Effect of 6.5cm cover on backscatter cross-section of smooth saline ice at X band, as determined from data obtained during the CRREL'87 experiment, for (a) VV polarization and (b) HH polarization.

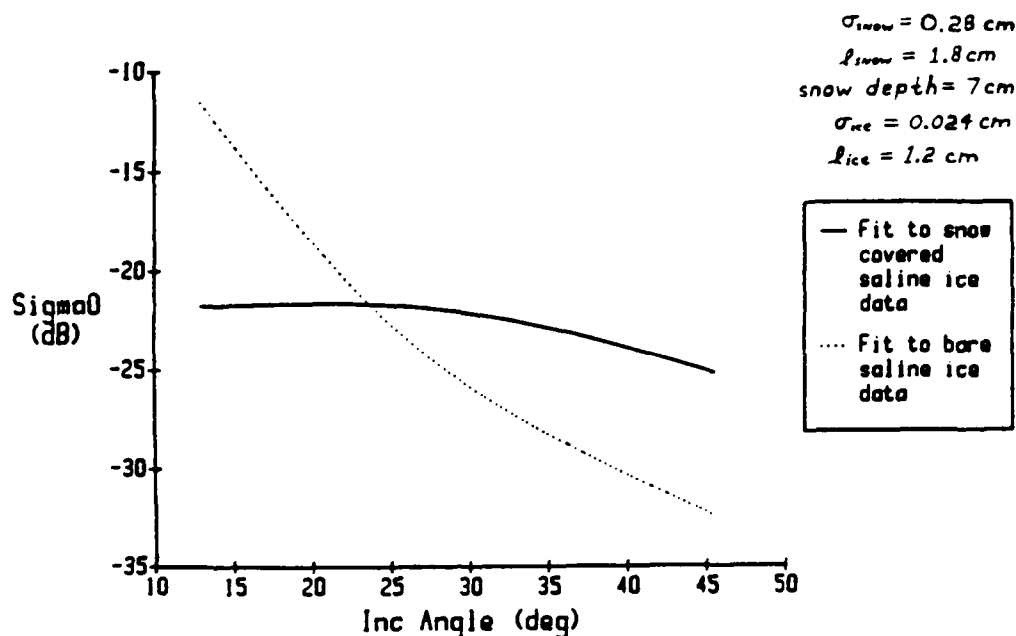


Figure 6.11: Effect of 7cm snow cover on backscatter cross-section of smooth saline ice at C band, as determined from data obtained during the CRREL'89 experiment (see data points on Figs. 6.7 and 6.13).

Surprisingly, a 10 dB reduction at 13° incidence was also noticed (See Fig. 6.11). The layer model of Ulaby et al [1982] is used to illustrate the snow volume scatter effect at larger incidence angles.

This layer model has the form:

$$\sigma^0 = T^2 [\sigma_{ds}^0 + \sigma_{ice}^0 / L^2] + \sigma_{\text{snow surf}}^0 \quad (6.12)$$

where T = transmission coefficient of the air-snow interface

$$L = \exp(k \, d \sec(\theta))$$

$$\sigma_{ds}^0 = \text{see equation (6.11)}$$

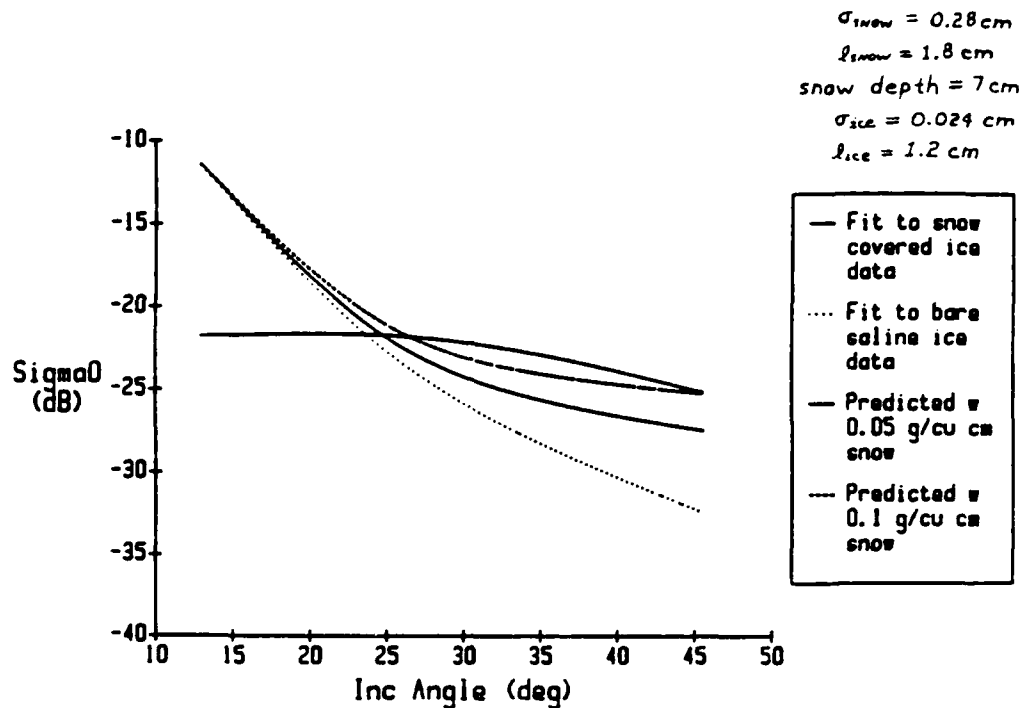


Figure 6.12: Backscatter cross-section of snow covered smooth saline ice surface at C band, as determined from data obtained during the CRREL'89 experiment, compared with predictions of the layer model of Ulaby et al. [1982].

$\sigma_{\text{snow surf}}^0$ = snow surface backscatter cross-section

Figure 6.12 shows predicted σ^0 for the combined surface using $\rho_s = 0.05 \text{ g/cm}^3$ and 0.1 g/cm^3 (measured value of ρ_s was 0.06 g/cm^3). Notice that the return is well predicted for $\rho_s = 0.1 \text{ g/cm}^3$ except at 13° incidence. Figure 6.13 illustrates the relative contributions to σ^0 by the snow surface, snow volume, and ice for $\rho_s = 0.1 \text{ g/cm}^3$. Notice that the measurement at 13° is the same as that predicted for snow

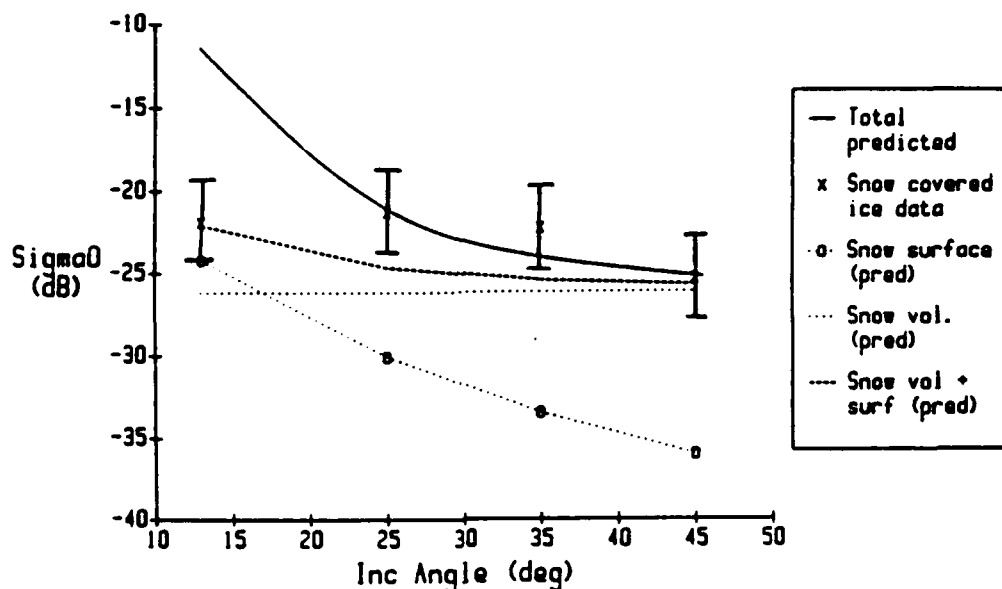


Figure 6.13: Backscatter cross-section of snow covered smooth saline ice surface at C band, as determined from data obtained during the CRREL '89 experiment, and predicted relative contributions of snow surface, snow volume, and ice.

surface+volume scatter only.

The reduction at 13° incidence cannot be explained by snow surface roughness. Scattering was weak due to the low snow dielectric constant ($\epsilon_r' \leq 1.2$). Two possible reasons for this reduction have been considered, neither of which can be verified. It is possible that we altered the properties of the ice surface in the process of removing the snow (we studied the snow covered surface prior to the bare ice surface). However, we found no evidence that the snow

cover modified the ice surface or that we altered the ice surface in the process of shoveling and sweeping snow; the ice surface was dry and naturally smooth after the snow was removed (the conditions at the time of the measurement were ice salinity of 30/00, dry snow, and cold temperatures of $\approx -10^{\circ}\text{C}$). Further, we had little difficulty removing the snow all the way down to the ice surface.

Another possible explanation is that the snow may have been acting as an impedance matching layer. Normally, a thin layer of snow settles to a nearly uniform density within a period of a few hours after it falls [Gow, 1989]. We studied the snow covered ice sheet less than 2 hours after the snow fell. If only partial settling had occurred, it could have been that the density of the snow varied as a function of depth, thus forming a layer with a tapered impedance (with impedances varying from about $Z_{\text{free space}} / \sqrt{1.2}$ to $Z_{\text{free space}} / \sqrt{1.4}$). Such a layer could have caused partial matching over the wide r.f. bandwidth of our radar (Tapered impedances are commonly used to match circuits of different impedance over wide bandwidths; e.g., [Izadian, 1988] and [Ahmed, 1981]). This set of circumstances is not typical, however [Gow, 1989].

6.2.3 Rough saline ice

During the CRREL'88 experiment backscatter from

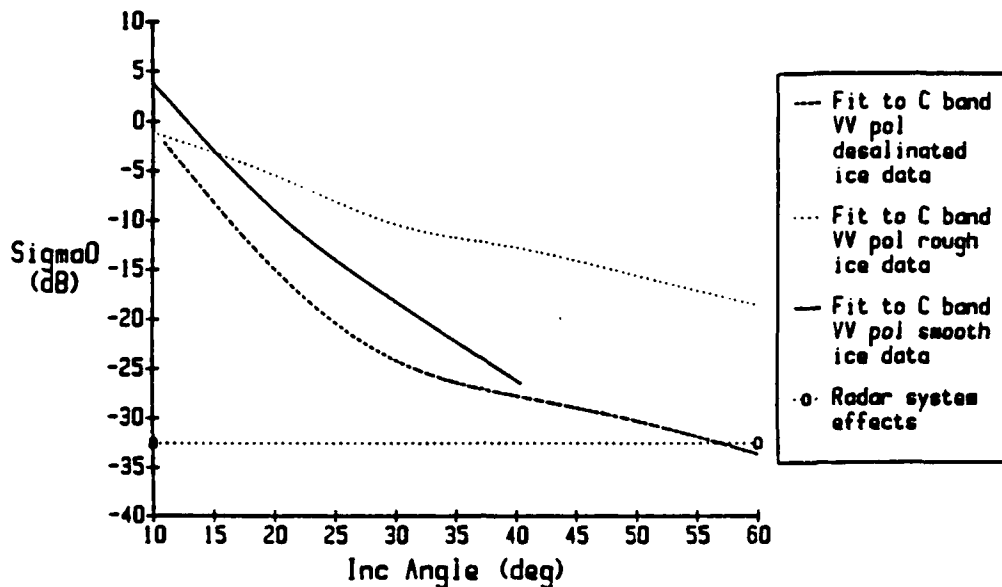


Figure 6.14: Comparison of backscatter cross-sections of smooth, rough, and desalinated ice at C band, as determined from data obtained during the CRREL'88 experiment (see data points on Figs. 6.15 and 6.16).

smooth and rough ice surfaces was compared. After measurements of the smooth ice sheet were performed, 1x2 cm ice prisms were dumped on the ice surface and more measurements were done. The roughness caused an increase in the incoherent return at larger incidence angles, as would be expected (See Fig. 6.14).

The criteria for neither the small perturbation nor the Kirchhoff surface scattering theories is satisfied in this case, i.e., the rms height is too large for the former ($ka \approx 0.6$ and $\sqrt{2}\sigma/l \approx 0.7$), and the

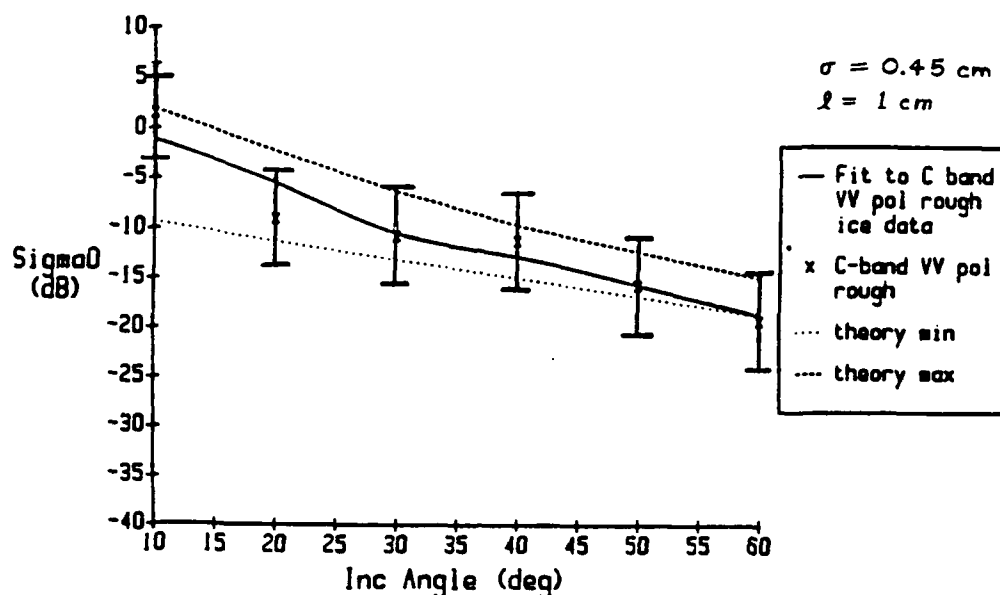


Figure 6.15: Backscatter cross-section of rough saline ice sheet at C band, as determined from data obtained during the CRREL'88 experiment, compared with predictions of the Small Perturbation Method.

radius of curvature is too small for the latter. Nevertheless the Small Perturbation Method predicts the backscatter measured, over the entire angular range (See Fig. 6.15).

6.2.4 Desalinated ice

Backscatter measurements of desalinated ice were made at C band, during the 1988 experiments, and at C and Ku band during 1989. During 1988 the results shown in Fig. 6.14 were obtained. Notice that σ^0 for desalinated ice decreased about as quickly as a

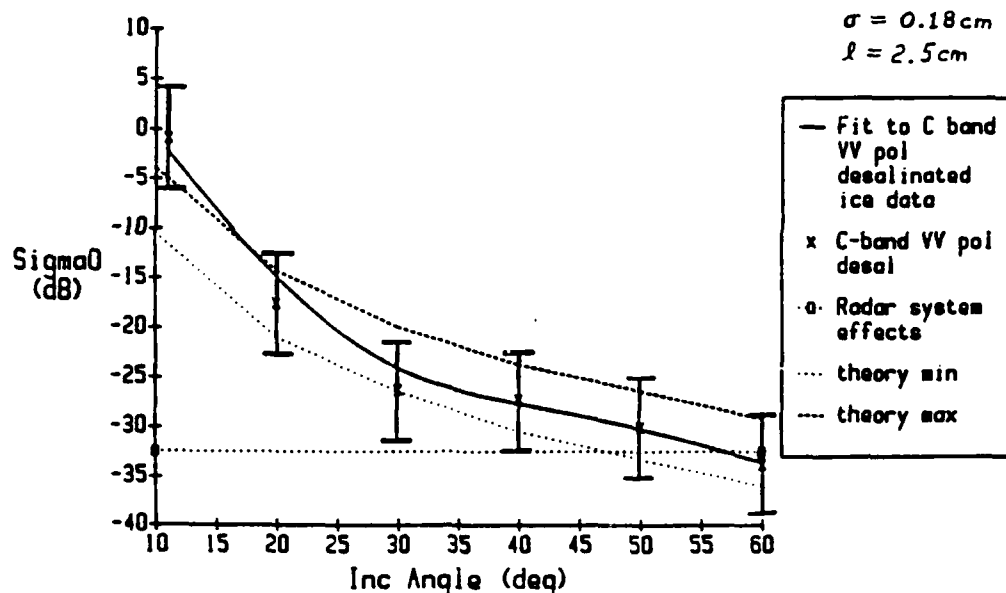


Figure 6.16: Backscatter cross-section of desalinated ice sheet at C band, as determined from data obtained during the CRREL'88 experiment, compared with predictions of the Small Perturbation Method.

function of incidence angle as did σ^0 for smooth saline ice, up to 30° incidence, implying that surface scatter was dominant. The flat portion at incidence angles greater than 30° may have been due to volume scatter; it is difficult to be certain because radar system effects were considerable at this low σ^0 level.

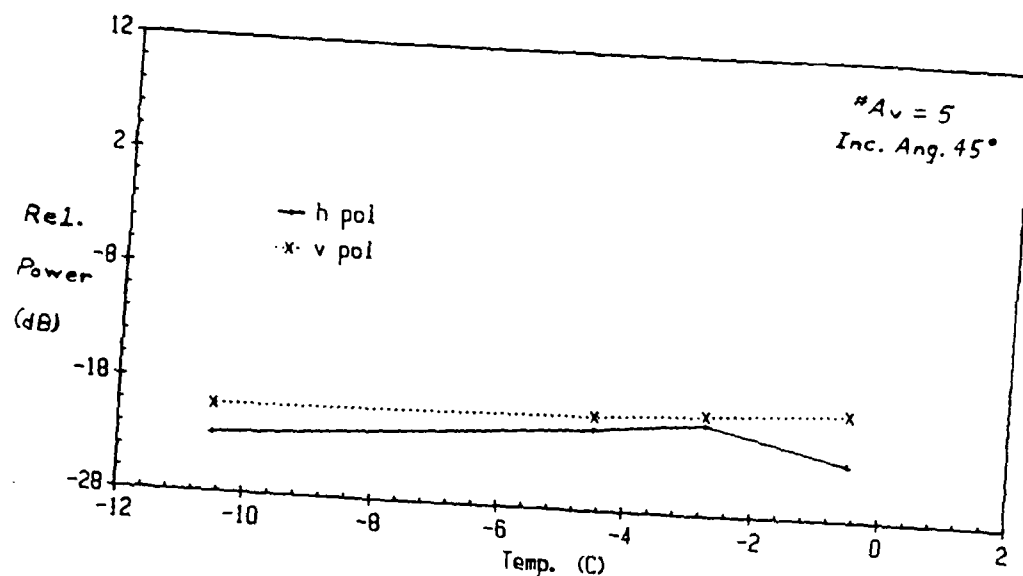
Notice from Fig. 6.16 that the Small Perturbation Method predicts the backscatter measured, over the entire angular range.

A simple experiment was done on this sheet to

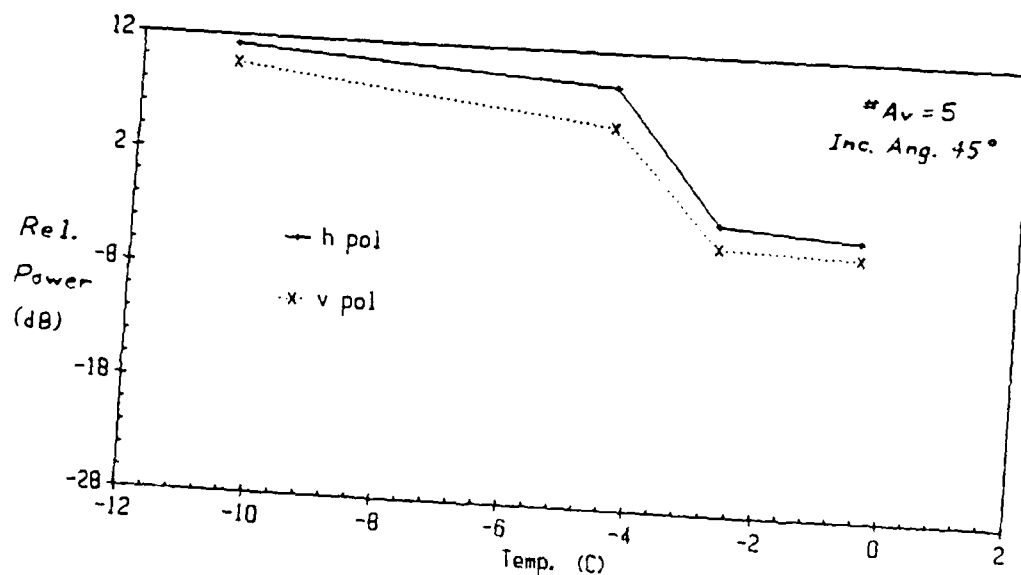
study the volume scattering component. Backscatter was measured as a function of ice surface temperature at a fixed incidence angle. We found that C-band σ^0 varied almost imperceptibly as free water formed at the ice surface (Fig. 6.17a) confirming that the volume scatter contribution was very small. In contrast we observed that σ^0 at X band decreased markedly as the ice surface began to melt (Fig. 6.17b) indicating that volume scatter was significant at X band.

During 1989 we measured backscatter from desalinated ice blocks (See Chpt. 3). The results of the backscatter measurements at C and Ku bands are shown in Fig. 6.18. Notice that $\sigma^0(\theta)$ for Ku band is approximately independent of θ , characteristic of volume scatter [Kim, 1984a]. On the other hand $\sigma^0(\theta)$ at C band falls off more than 10 dB from 15° incidence to 25° incidence, as is characteristic of a return with a large surface scatter component.

During the following analysis we assume, for simplicity, that the ice blocks contained spherical air bubbles of radius 0.45 mm, that the volume fraction of air in the ice was 20%, and the dielectric constant of the ice was uniform at $2.5-j0.01$; these were characteristics of the top layer of the ice. One-way transmission losses of the ice at Ku and C bands were 10 dB at Ku band and 5 dB at C band. Predicted one-way



(a)



(b)

Figure 6.17: Effect of temperature on backscatter from desalinated ice at (a) C band and (b) X band, as determined from data obtained during the CRREL'88 experiment.

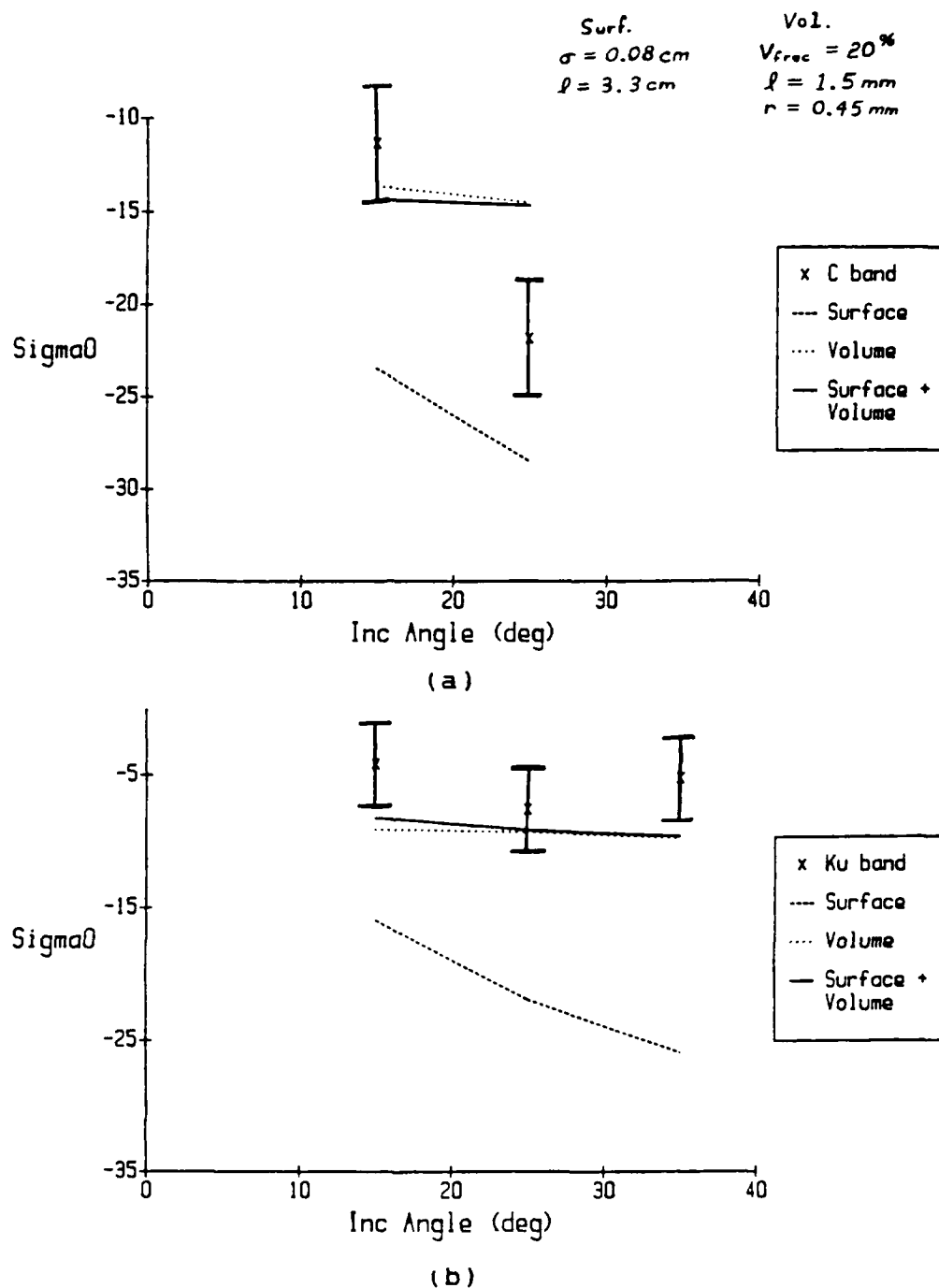


Figure 6.18: Backscatter cross-section of desalinated ice at (a) C band and (b) Ku band, as determined from data obtained during the CRREL'89 experiment, compared with combined predictions of Small Perturbation Method surface and Effective Medium volume scattering theories.

attenuation due to absorption for this ice sheet, based on the estimated dielectric profile is shown in Fig. 3.21 and is 3.5 dB at Ku band and 1.5 dB at C band. Thus, scattering losses are assumed to be 6.5 dB at Ku band and 3.5 dB at C band. Because the air bubble sizes were larger and the number of them more dense in the upper layer, it is assumed that they were responsible for the greatest scattering loss and that we are justified in making the above assumptions.

As a first approximation we assume that the backscatter was due to uncorrelated Rayleigh scattering. The volume scatter coefficient in this case is

$$\sigma_v = 64\pi^5 / \lambda_{ice}^4 |K|^2 N r^6 \quad [\text{Ulaby et al, 198}] \quad (6.13)$$

where λ_{ice} = wavelength in ice

$$K = (\epsilon_c - 1) / (\epsilon_c + 2) = 0.33 \quad (\text{where } \epsilon_c = 1 / \epsilon_{ice})$$

N = number of air bubbles/cu meter

r = radius of air bubbles

At C band $\sigma_v \approx 0.016$ and at Ku band $\sigma_v \approx 0.647$

Assuming that the extinction coefficient is uniform throughout the ice sheet and is of magnitude to account for the losses measured, $k_e = -7.2$ for C band and -14.4 for Ku band.

$$\text{This results in } \sigma_v^o \approx \sigma_v \int_0^{\infty} \exp(-2k_e z) dz \quad (6.14)$$

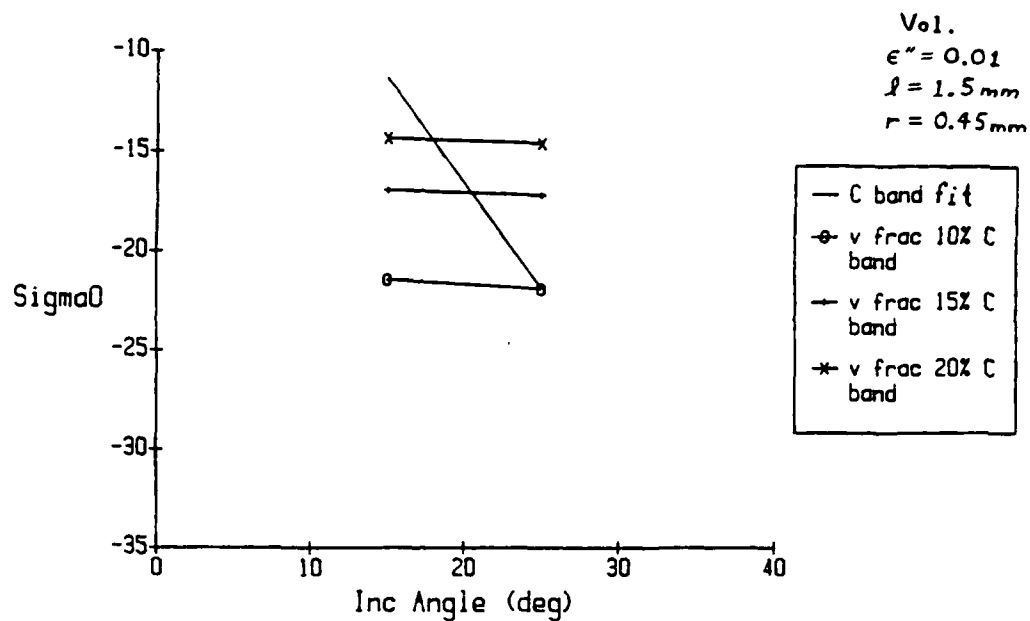
or $\sigma_v^o \approx -16.5$ dB at Ku band and -29.5 dB at C band.

These results are considerably lower than the data (See Fig. 6.18 for data).

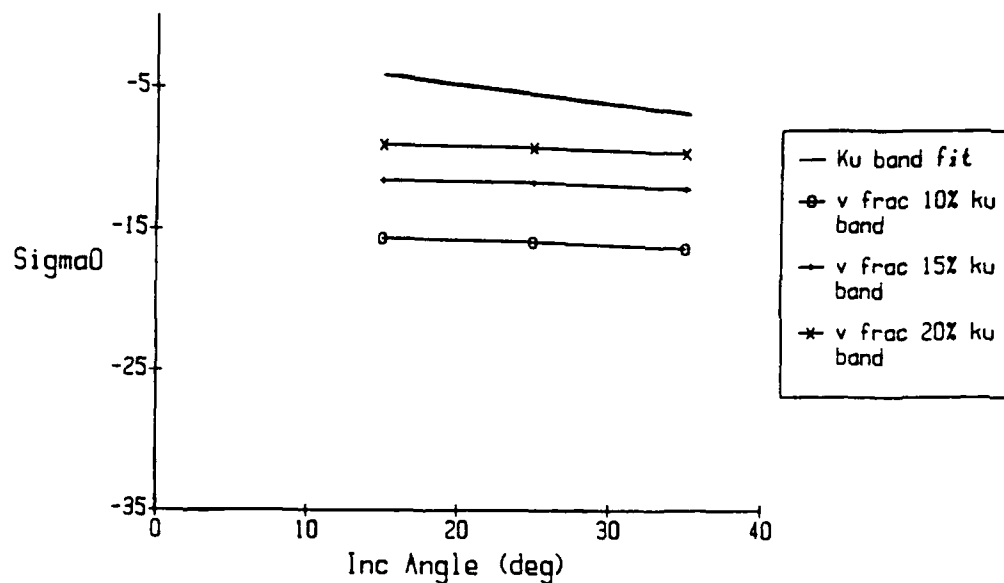
Consider predictions of the Effective Medium volume scattering theory. This theory considers both correlated and uncorrelated scattering. (The theory that was used differs slightly from the one presented in Chapter 2 - we used the one considered here because tested software was already available. This theory differs from the one presented in Chapter 2 in that this theory only considers the loss due to scattering that is accounted for in estimates of the dielectric constant, and correlation between scatterers is considered by means of a correlation function rather than a two-particle distribution function. Details can be found in Fung [1989].) The predictions for the volume scatter component of the desalinated ice blocks, using volume fraction of air = 20%, air bubble radius = 0.45 mm, correlation length = 1.5 mm, and $\epsilon'' = 0.01$, and Small Perturbation predictions for the surface scatter component, are shown in Figs. 6.18. Notice that the prediction for Ku band falls within the measurement error bars. On the other hand the C band prediction is 7 or 8 dB higher than the measured data. We are uncertain of the reason for the large prediction at C band.

To determine a possible explanation for this we varied each input parameter around the measured value to study its effect. Notice from Fig. 6.19 that a decrease in volume fraction causes the prediction at both frequencies to decrease. The same is true of an increase in ϵ'' (Fig. 6.20). Notice in Fig. 6.21, however, that a decrease in the correlation length caused a large decrease in C band predictions but only a small decrease in the Ku band predictions.

The results of these comparisons of measurements of desalinated ice blocks and theoretical predictions are encouraging; but several things prevent us from making stronger statements concerning quantitative comparisons. First, the bubble-structure data were obtained from one sample of the desalinated ice blocks, leaving questions as to the statistical uncertainty of the bubble structure - Figure 6.21 shows that such uncertainty can be of considerable importance. Second, the conditions under which the experiments were performed were less than ideal. For example, the antenna pointing angle was difficult to control (and monitor) for this experiment because the gantry was on a very unlevel surface, leaving questions as to the uncertainty in surface contributions at lower incidence angles; and it was not possible to eliminate or quantify the effects of backscatter from block edges,



(a)



(b)

Figure 6.19: Backscatter cross-section of desalinated ice at (a) C band and (b) Ku band, as determined from data obtained during the CRREL'89 experiment, compared with predictions of the Effective Medium theory at three different values of volume fraction of air.

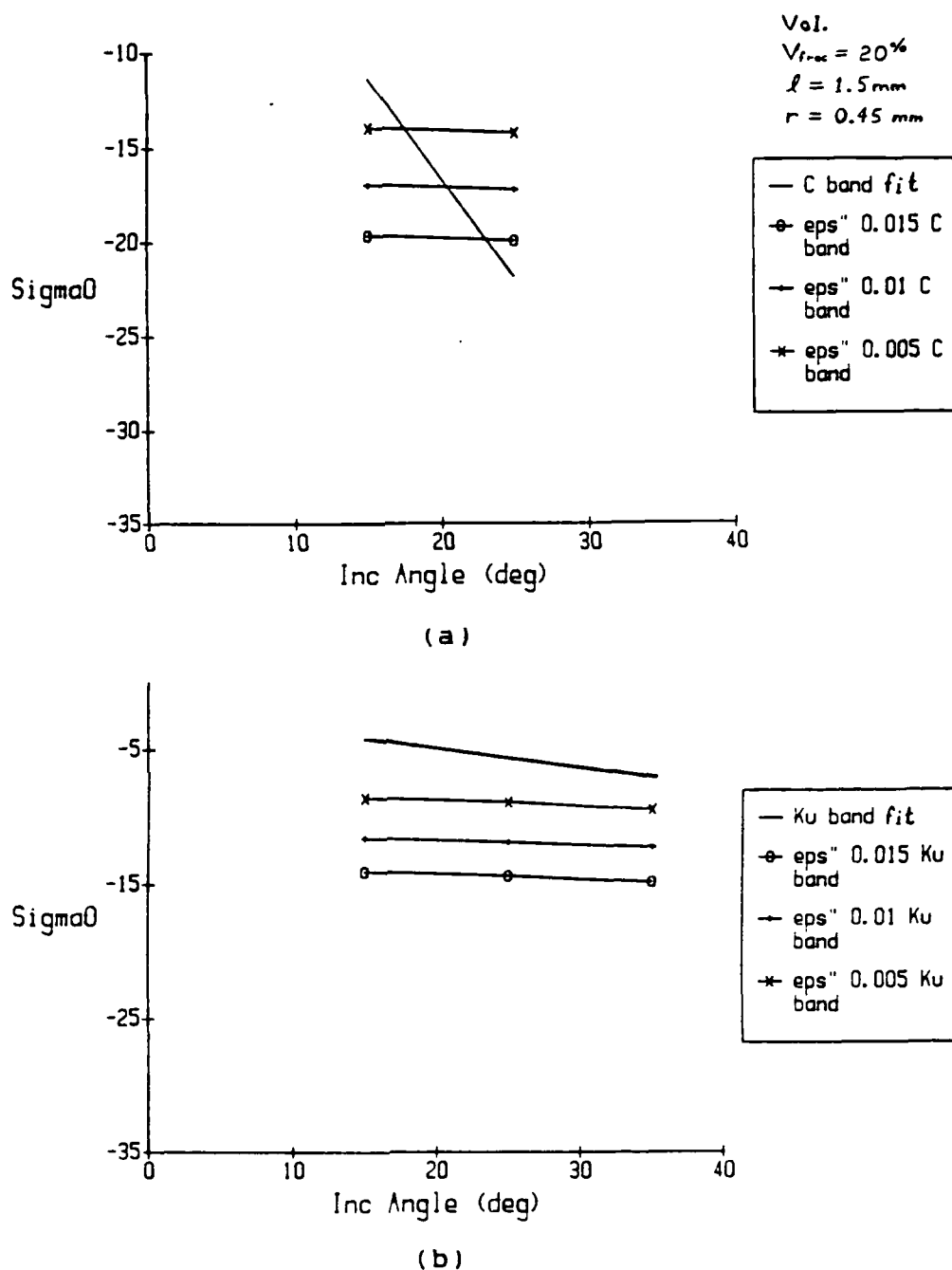
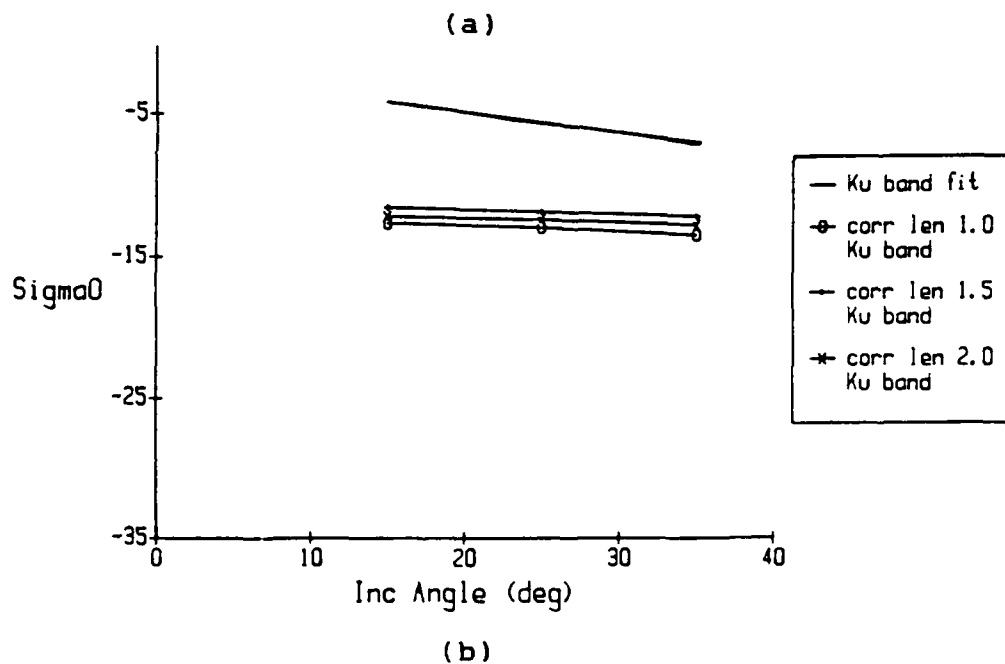
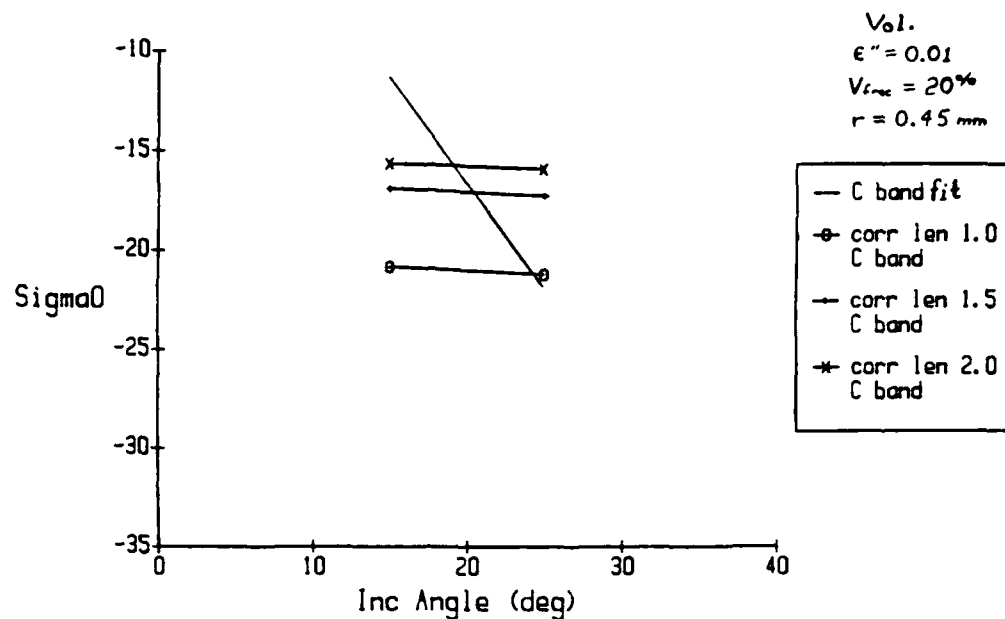


Figure 6.20: Backscatter cross-section of desalinated ice at (a) C band and (b) Ku band, as determined from data obtained during the CRREL'89 experiment, compared with predictions of the Effective Medium theory for three different values of the imaginary component of the dielectric constant.



(b)

Figure 6.21: Backscatter cross-section of desalinated ice at (a) C band and (b) Ku band, as determined from data obtained during the CRREL'89 experiment, compared with predictions of the Effective Medium theory for three different values of correlation length of spacing between air bubbles.

which could have been considerable since wide-beamwidth antennas (horns) were used, resulting in uncertainty as to the relative contributions of both surface and volume.

7.0 Conclusions and Recommendations

7.1 Conclusions

The purpose of this research was to determine the sources of scattering of artificial sea ice, to compare backscatter measurements semi-quantitatively with theoretical predictions, and to develop inexpensive polarimetric radars for sea ice backscatter studies.

In the investigation of scattering from artificial sea ice we came to the following conclusions:

1. The volume scatter contribution to backscatter from smooth (rms height < 0.05 cm) saline ice at C band cannot be neglected. We were unable to quantify the relative surface and volume contributions, but our results indicate that the volume contribution is comparable to the surface contribution.
2. A thin dry snow layer greatly altered the measured backscatter cross-section of smooth (rms height < 0.05 cm) saline ice at C band and incidence angles greater than about 25° . The large reduction in σ° near nadir, presented in Chapter 6, was due to a set of circumstances atypical of conditions in the Arctic or Antarctic. A thin dry snow layer did not noticeably influence measured backscatter from slightly rough (rms height > 0.1 cm) saline ice at X band when the surface was sufficiently rough with respect to a wavelength that surface

scatter dominated over volume scatter from the snow.

One can surmise that snow would dominate X-band scattering if the underlying ice were sufficiently smooth, but no such experiment was performed.

3. Backscatter from rough saline ice at C band is dominated by the contribution from the surface. For this rough surface the Small Perturbation Method correctly predicted the measured data over incidence angles of 0 to 60 degrees.
4. Backscatter from slightly rough (rms height > 0.15 cm) desalinated ice at C band and incidence angles less than about 30 degrees is dominated by surface scatter. Volume scatter is important at X band and is dominant at Ku band.

The CRREL facility is useful, but a number of factors limited the quality of our measurements. These need to be improved; e.g.,

- (1) environmental conditions were often not well controlled because of the poor condition of the roll-back tent;
- (2) a common gantry restricted the experiment plans of individual investigators, and the gantry could not easily be moved by a single person;
- (3) insufficient manpower was available to thoroughly characterize the ice sheets; and
- (4) available technology was not being used to

characterize the ice. For example, surface roughness measurements were made using cumbersome and time-consuming contact methods that limited the number of roughness samples that could reasonably be taken, rather than noncontact laser profilometer or stereo pair photographic techniques; and dielectric constants were estimated from empirical equations rather than measured.

The uncertainty in our backscatter data could have been reduced if we would have been able to carry out our own experiment plans because in many cases we would have taken more measurements than we were otherwise permitted to, and the uncertainty in surface characterization could have been reduced if available technology and more manpower had been utilized to thoroughly characterize the ice sheets.

Finally, we conclude that inexpensive radars, such as those presented in Chapter 4, can provide adequate measurements of backscatter cross-section and scattering matrices of the surfaces reported in this paper.

7.2 Recommendations

Future measurements should emphasize thorough characterization of the ice surfaces so that more precise comparisons of measurement and theory can be done. Sufficient manpower should be provided to

continuously monitor ice structural parameters; and available technology should be utilized to measure these parameters frequently and accurately. Current technology is being used to study the internal characteristics of the ice. It should also be used to monitor surface roughness, dielectric properties, etc.

Measurements of very smooth surfaces should be conducted with low-sidelobe narrow-beam antennas to improve sensitivity and to avoid problems introduced by wide-beam antennas.

The phase calibration technique that was developed is useful in the laboratory. To avoid the need for frequent phase calibration, stable oscillators should be used for up-converting and down-converting in step frequency radars, and VV and HH polarization channel system paths should be phase-matched, to the extent possible, for the FM-CW and step frequency radar systems.

Bibliography

- Addison, J.R. (1969), "Electrical properties of saline ice," Journal of Applied Physics, vol. 40, no. 8, pp. 3105 - 3114.
- Ahmed, M.J., (1981), "Impedance transformation equations for exponential, cosine-squared, and parabolic tapered transmission lines," IEEE Trans. on Microwave Theory and Techniques, vol. MTT-29, no. 1, pp. 67-68.
- Alfultis, M.A., S. Martin, (1987), "Satellite passive microwave studies of the Sea of Okhotsk ice cover and its relation to oceanic processes, 1978-1982," Journal of Geophysical Res., vol. 92, pp. 13013-13028.
- Anderson, D.L., (1960), "The physical constants of sea ice," Research, vol. 13, no. 8, pp. 310-318.
- Anderson, V.H. (1966), "High altitude, side-looking radar images of sea ice in the Arctic," Proc. 4th Symp. on Remote Sensing of the Environment, Institute of Science and Technology, University of Mich., Ann Arbor, pp. 845-857.
- Arcone, S.A., A.J. Gow, S. McGrew (1986a), "Microwave Dielectric, Structural and Salinity Properties of Simulated Sea Ice," IEEE Trans. on Geoscience and Remote Sensing, vol. 24, no. 6, pp. 832-839.
- Arcone, S.A., A.J. Gow, S. McGrew, (1986b), "Structure and dielectric properties at 4.8 and 9.5 GHz of saline ice," Journal of Geophysical Res., vol. 91, no. C12, pp. 14281-14303.
- Askne, J., R. Johansson, (1988), "Ice ridge observations by means of SAR," Digest ICARSS88, vol. 2, pp. 801-803.
- Assur, A., (1958), "Composition of sea ice and its tensile strength," Arctic Sea Ice, U.S. National Academy of Sciences, National Research Council, Publication 598, pp. 106-138.
- Bogorodsky, V.V. (1978), "Electromagnetic characteristics of sea ice and its radio soundings," unpublished.

Bogorodsky, V.V., A.N. Darovskih, (1984),
"Interpretation of aircraft sea ice microwave data,"
Journal of Oceanic Eng., vol. 9, no. 5, pp. 344-346.

Breipohl, W.L., (1970), Probabilistic systems analysis,
John Wiley and Sons, Inc., New York.

Brown, R.G., (1983), Introduction to random signal
analysis and Kalman filterin, John Wiley & Sons, Inc.,
N.Y..

Burns, B.A., D.J. Cavalieri, M.R. Keller, W.J.
Campbell, T.C. Grenfel, G.A. Maykut, P. Gloersen,
(1987), "Multisensor comparison of ice concentration
estimates in the marginal ice zone," Journal of
Geophysical Res., vol. 92, pp. 6843-6856.

Campbell, W.J., J. Wayenberg, J.B. Ramseyer, R.O.
Ramseier, M.R. Vant, R. Weaver, A. Redmond, L.
Arsenault, P. Gloersen, H.J. Zwally, T.T. Wilheit, C.
Chang, D. Hall, L. Gray, D.C. Meeks, M.L. Bryan, F.T.
Barath, C. Elachi, F. Leberl, T. Farr, (1978),
"Microwave remote sensing of sea ice in the AIDJEX Main
Experiment," Boundary Layer Meteorology, vol. 13, no.
1-4, pp. 309-337.

Caputi, W.J., (1973), "Stabilized linear FM generator,"
IEEE Trans. on Aerospace and Electron. Syst., vol. AES-
9, no. 5, pp. 670-678.

Carsey, F.D., (1982), "Arctic sea ice distribution at
end of summer 1973-1976 from satellite microwave data,"
Journal of Geophysical Res., vol. 87, no. 28, pp. 5809-
5835.

Carsey, F.D. (1985), "Summer Arctic Sea Ice Character
From Satellite Microwave Data," Journal of Geophysical
Res., vol. 90, no. C3, pp. 5015-5034.

Cavalieri, D.J., P. Gloersen, T.T. Wilheit, Jr.,
(1986), "Aircraft and satellite microwave observations
of the Bering Sea ice cover during MIZEX west," IEEE
Trans. on Geoscience and Remote Sensing, vol. GE-24,
no. 3, pp. 368-377.

Clark, R.J., Jr., D.B. Swartz, (1971), "YIG-tuned
oscillators --- principles of operation and present
status," Watkins-Johnson Co., 3333 Hillview Ave., Palo
Alto, California.

- Collins, M.J., W.J. Emery, (1988), "A computational method for estimating sea ice motion in sequential Seasat Synthetic-Aperture radar imagery by matched filtering," Journal of Geophysical Res., vol. 93, pp. 9241-9251.
- Comiso, J.C., W. Sullivan, (1986a), "Satellite microwave and in-situ observations of the Weddell Sea ice cover and its marginal ice zone," Journal of Geophysical Res., vol. 91, no. C8, pp. 9663-9681.
- Comiso, J.C., (1986b), "Characteristics of Arctic winter sea ice from satellite multispectral microwave observations," Journal of Geophysical Res., vol. 91, no. C1, pp. 975-994.
- Curlander, J.C., B. Holt, K.J. Hussey (1985), "Determination of Sea Ice Motion Using Digital SAR Imagery," IEEE Journal of Oceanic Eng., vol. OE-10, No. 4, pp. 358-367.
- Eppler, D.T., L.D. Farmer, A.W. Lohanick, (1986), "Classification of sea ice types with single-band (33.6 GHz) airborne passive microwave imagery," Journal of Geophysical Res., vol. 91, no. C9, pp. 10661-10695.
- Fily, M., D.A. Rothrock (1986), "Extracting Sea Ice Data from Satellite SAR Imagery," IEEE Trans. on Geoscience and Remote Sensing, vol. GE-24, no. 6, pp. 849-854.
- Fily, M., D.A. Rothrock, (1987), "Sea ice tracking by nested correlations," IEEE Trans. on Geoscience and Remote Sensing, vol. GE-25, pp. 570-580.
- Finkelstein, M.I., V.A. Kutev, (1972), "Probing of sea ice with a sequence of video pulses," Radioengineering and Electronics, vol. 17, no. 10, pp. 1680-1684.
- Frankenstein, G. and R. Garner (1967), "Equation for determining the brine volume of sea ice from -0.50 to -22.90C," Journal of Glaciology, vol. 6, pp. 943 - 944.
- Fung, A.K., (1989), personal correspondence.
- Gedney, R.T., R.J. Schertler, R.A. Mueller, R.J. Jirberg, H. Mark, (1975), "An operational all-weather Great Lakes ice information system," Proc. 3rd Canadian Symposium on Remote Sensing, Edmonton, Alberta, pp. 73-82.

Gedney, R.T., R.J. Jirberg, R.J. Schertler, R.A. Mueller, T.L. Chase, I. Kramarchuk, L.A. Nagy, R.A. Hanlon, H. Mark, (1977), "All weather ice information system for Alaskan coastal shipping," 9th Annual Offshore Technology Conference, Houston, TX, pp. 299-306.

Gloersen, P., W. Nordberg, T.J. Schmugge, T.T. Wilheit (1973), "Microwave Signatures of First-Year and Multiyear Sea Ice," Journal of Geophysical Res., vol. 78, no. 18, pp. 3564-3572.

Gloersen, P., R.O. Ramseier, W.J. Campbell, T.C. Chang, T.T. Wilheit, (1975), "Variation of ice morphology of selected mesoscale test areas during the Bering Sea Experiment," in Proc. of the Symposium of the Joint U.S./U.S.S.R. Bering Sea Experiment, edited by K. Ya. Kondratyev, pp. 196-218, Gidrometeoizdat, Leningrad.

Gloersen, P., W.J. Campbell, (1988), "Satellite and aircraft passive microwave observations during the marginal ice zone experiment in 1984," Journal of Geophysical Res., vol. 93, pp. 6837-6846.

Glushkov, V.M., V.B. Komarov, (1971), "Side-looking imaging radar system TOROS and its application to the study of ice conditions and geological explorations," Proc. 7th Int'l Symposium on Remote Sensing of Environment, University of Michigan, Ann Arbor.

Gogineni, S.P. (1984), Radar Backscatter from Summer and Ridged Sea Ice, and Design of Short-Range Radars, PhD dissertation, University of Kansas.

Gow, A.J., (1988), personal correspondence.

Gow, A.J., (1989), personal correspondence.

Gray, A.L., R.O. Ramseier, W.J. Campbell, (1977), "Scatterometer and SLAR results obtained over Arctic sea-ice and their relevance to the problems of Arctic ice reconnaissance," 4th Canadian Symposium on Remote Sensing, Quebec City, May, 1977.

Gray, A.L. (1980), "Depression angle study," SURAT Rep. 2, Electromagnetics Inst., Univ. of Denmark, 20 pp.

Gray, A.L., R.K. Hawkins, C.E. Livingstone, L. Drapier Arsenault, W.M. Johnstone (1982), "Simultaneous Scatterometer and Radiometer Measurements of Sea-Ice Microwave Signatures," IEEE Journal of Oceanic Eng., vol. OE-7, No. 1, pp. 20-32.

Hagman, B.B., (1976), "On the use of microwave radiation for Great Lakes ice surveillance," NOAA Technical memorandum ERL GLERL-13, Great Lakes Environmental Research Laboratory, Ann Arbor, Mich.

Hallikainen, M. (1982), "The brightness temperature of sea ice and fresh-water ice in the frequency range 500 MHz to 37 GHz," IEEE IGARSS Digest, vol. II.

Hallikainen, M.T., J.M. Hyypä, M.V.O. Toikka, J.A.E. Haapanen, T.I. Tares, P.J. Ahola, (1988), "Backscatter behaviour of low-salinity sea ice at C- and X-band," Digest IGARSS88, vol. 2, pp. 791-792.

Hawkins, R.K., C.E. Livingstone, A.L. Gray, K. Okamoto, L.D. Arsenault, D.E. Pearson, (1980), "Single and multiple parameter microwave signatures of sea ice," in Proc. 6th Canadian Symp. Remote Sensing, Halifax, Canada, pp. 217-230.

Holmes, Q.A., D.R. Nusesch, R.A. Shuchman (1982), "Textural Analysis and Real-Time Classification of Sea-Ice Types Using Digital SAR Data," IEEE Trans. on Geoscience and Remote Sensing, vol. GE-22, no. 2, pp. 113-120.

Iizuka, K., A.P. Freundorfer, K.H. Wu, H. Mori, H. Ogura, V.K. Nguyen, (1984), "Step-frequency radar," J. Applied Physics, vol. 56, no. 9, pp. 2572-2583.

Izadian, J.S., S.M. Izadian, (1988), Microwave transition design, Artech House, Inc., Norwood, MA.

Johnson, J.D. and L.D. Farmer (1971), "Use of Side-Looking Air-borne Radar for Sea Ice Identification," Journal of Geophysical Res., vol. 76, no. 9, pp. 2138-2155.

Ketchum, J.D., Jr., S.G. Tooma, Jr. (1973), "Analysis and Interpretation of Air-Borne Multifrequency Side-Looking Radar Sea Ice Imagery," Journal of Geophysical Res., vol. 78, no. 3, pp. 520-538.

Kim, Y.S. (1982), "Scattering coefficient estimation: an examination of the narrow-beam approximation," University of Kansas Remote Sensing Laboratory, Technical Report RSL TR 331-23.

Kim, Y.S. (1984a), Theoretical and Experimental Study of Radar Backscatter from Sea Ice, PhD dissertation, University of Kansas.

Kim, Y.S., R.G. Onstott, R.K. Moore (1984b), "The Effect of Snow Cover on Microwave Backscatter from Sea Ice," IEEE Journal of Oceanic Eng., vol. OE-9, no. 5, pp. 383-388.

Kim, Y.S., R.K. Moore, R.G. Onstott, S. Gogineni (1985), "Towards Identification of Optimum Radar Parameters for Sea-Ice Monitoring," Journal of Glaciology, vol. 31, no. 109, pp. 214-219.

Kurskaya, A.A., B.G. Kutuza (1984), "Radiophysical Techniques for Sea Ice Investigations," IEEE Journal of Oceanic Eng., vol. OE-9, no. 5, pp. 329-332.

Larson, R.W., R.A. Shuchman, R.F. Rawson, R.D. Worsfold (1978), "The Use of SAR Systems for Iceberg Detection and Characterization," Proc 12th Intl. Symp. of Remote Sensing of Environment, pp. 1127-1147.

Lee, M., (1988), "Sea-ice analysis software - iceman," Digest IGARSS88, vol. III, pp. 1717-1720.

Livingstone, C.E., et al, (1980), "Classification of Beaufort Sea ice using active and passive microwave sensors," Proc. of the Final SURSAT Ice Workshop, Toronto, Canada, Section 5.5.

Lohanick, A.W., T.C. Grenfel, (1986), "Variations in brightness temperature over cold first-year ice near Tuktoyaktuk, Northwest Territories," Journal of Geophysical Res., vol. 91, no. C4, pp. 5133-5144.

Loshchilov, V.S., V.A. Voyevodin, (1972), "Determination of elements of ice cover drift and ice hummock movement by means of TOROS airborne side-looking radar imagery assembly," Problems of the Arctic and Antarctic, Gidrometeoizdat Press, Leningrad.

Loshchilov, V.S., A.D. Masanov, I.G. Serebrennikov, (ca 1978), "The use of SLAR for the mapping of sea ice and the study of ice dynamics," publishing information unknown.

Luther, C.A., (1988), "Remote sensing in a marginal ice zone: a brief overview," Digest IGARSS88, vol. 2, pp. 1107-1109.

Lyden, J.D., B. Burns, A.L. Maffett (1982), "Characterization of Sea Ice Types Using Synthetic Aperture Radar," IEEE Trans. on Geoscience and Remote Sensing, vol. GE-22, no. 5, pp. 431-439.

Marthaler, J.G., J.E. Heighway, (1978), "Radar image processing of real-aperture SLAR data for the detection and identification of iceberg and ship targets," 5th Canadian Symp. on Remote Sensing, Victoria, B.C., Canada.

Martin, S. (1979), "A field study of brine drainage and oil entrainment in first-year sea ice," Journal of Glaciology, vol. 22, pp. 473 - 502.

Martin, S., B. Holt, D.J. Cavalieri, V. Squire, (1987), "Shuttle Imaging Radar B (SIR-B) Weddel Sea ice observations: a comparison of SIR-B and scanning multichannel radiometer ice concentrations," Journal of Geophysical Res., vol. 92, pp. 7173-7180.

Matzler, C., R.O. Ramseier, E. Svendsen, (1984), "Polarization effects in sea-ice signatures," IEEE Journal of Oceanic Eng., vol. OE-9, no. 5, pp. 333-338.

McNeill, D., P. Hoekstra, (1973), "In-situ measurements on the conductivity and surface impedance of sea ice at VLF," Radio Science, vol. 8, no. 1, pp. 23-30.

McNutt, L., R.K. Raney, (1988), "The LIMEX '87 pilot project, LIMEX '89 and long-term objectives for data collection on the Canadian east coast," Digest IGARSS88, vol. 1, pp. 421-422.

Murthy, H.A., S. Haykin (1987), "Bayesian Classification of Surface-Based Ice-Radar Images," IEEE Trans. on Oceanic Eng., vol. OE-12, No. 3, pp. 493-502.

Nakawo, M. and N.K. Sinha (1981), "Growth rate and salinity profile of first-year sea ice in the high Arctic," Journal of Glaciology, vol. 27, pp. 315 - 329.

Ninnis, R.M., W.J. Emery, M.J. Collins, (1986), "Automated extraction of pack ice motion from advanced very high resolution radiometer imagery," Journal of Geophysical Res., vol. 91, no. C9, pp. 10725-10734.

Onstott, R.G., R.K. Moore, and W.F. Weeks (1979a), "Surface-based scatterometer results of arctic sea ice," IEEE Trans. on Geoscience Electronics, vol. GE-17, pp. 78-85.

Onstott, R.G. and C.V. Delker (1979b), "Radar backscatter study of sea ice in the Beaufort Sea," Remote Sensing Lab., Center for Research, University of Kansas, Rep. 331-10, 30pp.

Onstott, R.G. (1980), Radar backscatter study of sea ice, Ph.D. thesis, University of Kansas.

Onstott, R.G. and S.P. Gogineni (1985), "Active microwave measurements of Arctic Sea Ice under summer conditions," Journal of Geophysical Res., vol. 90, no. C3, pp. 5035-5044.

Onstott, R.G., S.H. Gaboury, J. Bredow, S.P. Gogineni (1988), "Active Microwave Measurements of Artificial Sea Ice," Digest IGARSS88, vol. 2, pp. 805-807.

Parashar, S.K. (1974), Investigation of radar discrimination of sea ice, Ph.D. thesis, University of Kansas.

Pounder, E.R., (1965), The Physics of Ice, Pergamon Press, New York.

Racette, P., R. Forster, (1989), personal correspondence.

Raizer, V.Y., I.G. Zaitseva, V.M. Aniskovich, V.S. Etkin, (1986), "Determining sea ice physical parameters from remotely sensed microwave radiometer data in the 0.3-18 cm band," Soviet Journal of Remote Sensing (English ed.), vol. 5, pp. 29-42.

Ramseier, R.O., P. Gloersen, W.J. Campbell, T.C. Chang, (1975), "Mesoscale description for the principal Bering Sea ice experiment," in Proc. of the Symposium of the Joint U.S./U.S.S.R. Bering Sea Experiment, edited by K. Ya. Kondratyev, pp. 234-270, Gidrometeoizdat, Leningrad.

Rothrock, D.A., D.R. Thomas, A.S. Thorndike, (1988), "Principal component analysis of satellite passive microwave data over sea ice," Journal of Geophysical Res., vol. 93, no. C3, pp. 2321-2332.

Rouse, J.W. (1969), "Arctic Ice Type Identification by Radar," Proceedings of the IEEE, Vol. 57, No. 4, pp. 605-614.

Shaw, V.L., F.G. Bercha, W.H. McRuer, (1988), "Auto and cross correlation analysis of environment, system and target parameters for iceberg detection using airborne radar," Digest IGARSS88, vol. 2, pp. 809-816.

Shuchman, R.A., B.A. Burns, et al., (1986), "Geophysics of the Marginal Ice Zone," 1986 Geoscience and Remote Sensing Symposium Proceedings, vol. 1, pp. 345-351, 86CH2268-1.

Shuchman, R.A., L.L. Sutherland, O.M. Johannessen, E.D. Leavitt, (1988), "Geophysical information on the winter marginal ice zone obtained from SAR," Digest IGARSS88, vol. 2, pp. 1111-1114.

Steffen, K., J.A. Maslanik, (1988), "Comparison of Nimbus 7 scanning multichannel microwave radiometer radiance and derived ice concentrations with Landsat imagery for the north water area of Baffin Bay," Journal of Geophysical Res., vol. 93, no. C9, pp. 10769-10781.

Svendsen, E., K. Kloster, B. Farrelly, O.M. Johannessen, J.A. Johannessen, W.J. Campbell, P. Gloersen, D. Cavalieri, C. Matzler, (1983), "Norwegian remote sensing experiment: evaluation of the Nimbus 7 scanning multichannel microwave radiometer for sea ice research," Journal of Geophysical Res., vol. 88, no. C5, pp. 2781-2791.

Thomas, R.H. (1986), "Satellite Remote Sensing Over Ice," Journal of Geophysical Res., vol. 91, No. C2, pp. 2493-2502.

Timco, G.W. (1979), "An analysis of the in-situ resistivity of sea ice in terms of its microstructure," Journal of Glaciology, vol. 22, pp. 461 - 471.

Troy, B.E. (1981), "Measurement of the microwave properties of sea ice at 90 GHz and lower frequencies," Journal of Geophysical Res., vol. 86, no. C5, pp. 4283 - 4289.

Tsang, L., J.A. Kong, R.T. Shin (1985), Theory of Microwave Remote Sensing, Wiley, NY.

U. Kansas, unpublished findings from experiments at CRREL during 1984-1989.

Ulaby, F.T., R.K. Moore, A.K. Fung (1981), Microwave Remote Sensing - Active and Passive Vol I, Addison-Wesley Publishing Co.

Ulaby, F.T., R.K. Moore, A.K. Fung (1982), Microwave Remote Sensing - Active and Passive Vol II, Addison-Wesley Publishing Co., Chpt. 12.

Ulaby, F.T., R.K. Moore, A.K. Fung (1986), Microwave Remote Sensing - Active and Passive Vol III, Artech House, Inc., Dedham, Mass, Chapt. 13.

Untersteiner, N. (1968), "Natural desalination and equilibrium salinity profiles of perennial sea ice," Journal of Geophysical Res., vol. 73, no. 4, pp. 1251 - 1257.

Vant, M.R. (1976), A combined empirical and theoretical study of the dielectric properties of sea ice over the frequency range 100 MHz to 40 GHz, Ph.D. thesis, Carlton University.

Vant, M.R., R.O. Ramseier, and V. Makios (1978), "The complex dielectric constant of sea ice at frequencies in the range 0.1 - 40 GHz," Journal of Applied Physics, vol. 49, no. 3, pp. 1264 - 1280.

Vesecky, J.F., R. Samadani, M.P. Smith, J.M. Daida, R.N. Bracewell (1986), "Automated Remote Sensing of Sea Ice using Synthetic Aperture Radar," 1986 Geoscience and Remote Sensing Symposium Proceedings, vol. 1, pp. 127-132, 86CH2268-1.

Wackerman, C.C., R.R. Jentz, R.A. Shuchman, (1988), "Sea ice type classification of SAR imagery," Digest IGARSS88, vol. 1, pp. 425-428.

Wadhams, P., M.A. Lange, S.F. Ackley, (1987), "The ice thickness distribution across the Atlantic sector of the Antarctic Ocean in midwinter," Journal of Geophysical Res., vol. 92, no. C13, pp. 14535-14552.

Wadhams, P., (1988), "Winter observations of iceberg frequencies and sizes in the south Atlantic Ocean," Journal of Geophysical Res., vol. 93, no. C4, pp. 3583-3590.

Walsh, J., J. Dane, S.K. Srivastava, (1986), "Remote sensing of icebergs by ground-wave doppler radar," IEEE Trans. on Oceanic Eng., vol. OE-11, no. 2, pp. 276-284.

Wang, Q., (1988), personal correspondence.

Weeks, W.F. and A. Assur, (1969), "Fracture of Lake and Sea Ice," Research Report 269, Cold Regions Research and Engineering Laboratory, Hanover, NH.

Zoughi, R., L.K. Wu, R.K. Moore, (1984), "SOURCECAT: A very-fine-resolution radar scatterometer," University of Kansas Remote Sensing Laboratory, Technical Report RSL TR 5870-1.